

AD-A051 000

UNION CARBIDE CORP PARMA OHIO PARMA TECHNICAL CENTER
RUB TOLERANT MATERIALS DEVELOPMENT. NICKEL-CHROMIUM-ALUMINUM FO--ETC(U)
OCT 77 R J DUFALA

F/G 21/5

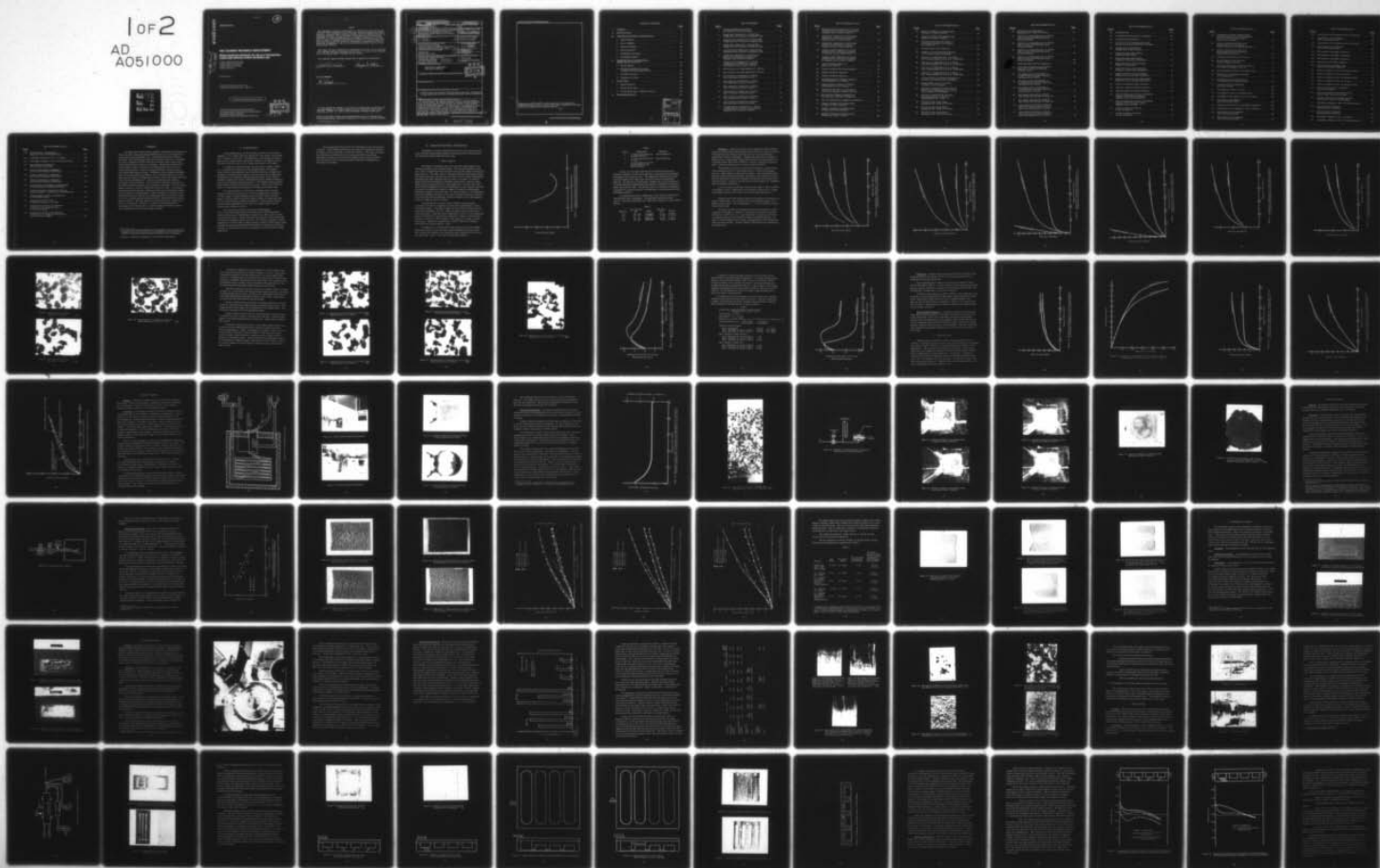
F33615-76-C-2098

UNCLASSIFIED

AFAPL-TR-77-46

NL

1 of 2
AD
A051000



AD A051000

AFAPL-TR-77-46

12
B.S.

RUB TOLERANT MATERIALS DEVELOPMENT

Nickel-chromium-aluminum for use as a transpiration-cooled high pressure turbine abradable seal

*UNION CARBIDE CORPORATION
CARBON PRODUCTS DIVISION
PARMA TECHNICAL CENTER
PARMA, OHIO 44130*

OCTOBER 1977

TECHNICAL REPORT AFAPL-TR-77-46
Final Report for Period June 1976 – April 1977

Approved for public release; distribution unlimited.

AIR FORCE AERO PROPULSION LABORATORY
AIR FORCE WRIGHT AERONAUTICAL LABORATORIES
AIR FORCE SYSTEMS COMMAND
WRIGHT-PATTERSON AIR FORCE BASE, OHIO 45433

DDC
RECEIVED
MAR 8 1978
B

NOTICE

When Government drawings, specifications, or other data are used for any purpose other than in connection with a definitely related Government procurement operation, the United States Government thereby incurs no responsibility nor any obligation whatsoever; and the fact that the government may have formulated, furnished, or in any way supplied the said drawings, specifications, or other data, is not to be regarded by implication or otherwise as in any manner licensing the holder or any other person or corporation, or conveying any rights or permission to manufacture, use, or sell any patented invention that may in any way be related thereto.

This report has been reviewed by the Information Office (OI) and is releasable to the National Technical Information Service (NTIS). At NTIS, it will be available to the general public, including foreign nations.

This technical report has been reviewed and is approved for publication.

John A. Conradi

Kerwyn D. Mack

FOR THE COMMANDER

H. Bush

"If your address has changed, if you wish to be removed from our mailing list, or if the addressee is no longer employed by your organization please notify AFAPL/TBC, W-PAFB, OH 45433 to help us maintain a current mailing list".

Copies of this report should not be returned unless return is required by security considerations, contractual obligations, or notice on a specific document.

SECURITY CLASSIFICATION OF THIS PAGE (When Data Entered)

REPORT DOCUMENTATION PAGE		READ INSTRUCTIONS BEFORE COMPLETING FORM	
1. REPORT NUMBER AFAPL-TR-77-46	2. GOVT ACCESSION NO.	3. RECIPIENT'S CATALOG NUMBER 9	
4. TITLE (and Subtitle) RUB TOLERANT MATERIALS DEVELOPMENT, Nickel-Chromium-Aluminum for Use as a Transpiration-Cooled High Pressure Turbine Abradable Seal.		5. TYPE OF REPORT & PERIOD COVERED Final Rept. June 76 - April 1977	
6. AUTHOR(s) R. J. Dufala		8. CONTRACT OR GRANT NUMBER(s) F33615-76-C-2098	
9. PERFORMING ORGANIZATION NAME AND ADDRESS Union Carbide Corporation Carbon Products Div., Parma Tech. Center 12900 Snow Road, Parma, Ohio 44130		10. PROGRAM ELEMENT, PROJECT, TASK AREA & WORK UNIT NUMBERS Project No. 3066	
11. CONTROLLING OFFICE NAME AND ADDRESS AFAPL/TBC WPAFB, Ohio 45433		12. REPORT DATE October 1977	
14. MONITORING AGENCY NAME & ADDRESS (if different from Controlling Office) Commander, DCASR Cleveland Federal Office Building 1240 East Ninth Street Cleveland, Ohio 44199		13. NUMBER OF PAGES 144	
		15. SECURITY CLASS. (of this report) Unclassified	
16. DISTRIBUTION STATEMENT (of this Report) Approved for Public Release Distribution Unlimited		15a. DECLASSIFICATION/DOWNGRADING SCHEDULE	
17. DISTRIBUTION STATEMENT (of the abstract entered in Block 20, if different from Report)			
18. SUPPLEMENTARY NOTES			
19. KEY WORDS (Continue on reverse side if necessary and identify by block number) Abradable Seal, Rub Tolerant, Nickel-Chromium-Aluminum, Transpiration Cooling, High Pressure Turbine, Oxidation Resistance, Erosion Resistance			
20. ABSTRACT (Continue on reverse side if necessary and identify by block number) A transpiration-cooled, high pressure gas turbine shroud was designed, built, and rig tested. The shroud consisted of a porous rub tolerant material, nickel-chromium-aluminum (NiCrAl) which was brazed to a flow control/ cooling gas distribution chamber. The NiCrAl layer was optimized for abrad- ability and thermal stability. A flow control chamber was designed which controlled the amount and distribution of the cooling gas flow to the rub tolerant layer. The shroud was tested for cyclic oxidation resistance and high velocity, hot gas erosion stability. Optimization of the system for			

DDC
RECEIVED
MAR 8 1978
REGULATED
B

DD FORM 1 JAN 73 1473 EDITION OF 1 NOV 65 IS OBSOLETE

SECURITY CLASSIFICATION OF THIS PAGE (When Data Entered)

i

409 746

AB

SECURITY CLASSIFICATION OF THIS PAGE(When Data Entered)

maintaining a 1900°F (1040°C) surface temperature in a high velocity, 2600°F (1427°C) gas stream was achieved by using a combination of thermal conduction and transpiration cooling mechanisms.

SECURITY CLASSIFICATION OF THIS PAGE(When Data Entered)

TABLE OF CONTENTS

	<u>Page</u>
I. SUMMARY	1
II. INTRODUCTION	2
III. ABRADABLE MATERIAL OPTIMIZATION	4
1. Static Oxidation	4
2. Cyclic Oxidation	23
3. Dynamic Oxidation	29
4. Particle Erosion	41
5. Abradability (In-House)	54
6. Abradability (NASA)	57
IV. TRANSPIRATION-COOLED SHROUD DESIGN AND EVALUATION	67
1. Plenum Design	67
2. Thermal Cycle/Hot Gas Erosion Testing for Structure Optimization	93
3. Variable Flow Test	130
4. Temperature Profile	137
V. CONCLUSION	143
1. Support Structure	143
2. Porous Metal Layer	143
3. Porous Metal Layer - Support Structure	144
VI. RECOMMENDATIONS	144

ACCESSION for		
NTIS	White Section	<input checked="" type="checkbox"/>
DDC	Buff Section	<input type="checkbox"/>
UNANNOUNCED		<input type="checkbox"/>
JUSTIFICATION _____		
BY _____		
DISTRIBUTION/AVAILABILITY CODES		
Dist.	AVAIL.	and/or SPECIAL
A		

LIST OF FIGURES

<u>Figure</u>		<u>Page</u>
1	Oxidation Weight Gain of NiCrAl as a Function of Al Concentration	5
2	Weight Gain of Material A-1 NiCrAl With Temperature as a Function of Oxidation Time	8
3	Volume Growth of Material A-1 NiCrAl With Temperature as a Function of Oxidation Time	9
4	Weight Gain of Material A-2 NiCrAl With Temperature as a Function of Oxidation Time	10
5	Volume Growth of Material A-2 NiCrAl With Temperature as a Function of Oxidation Time	11
6	Weight Gain of Material A-1 NiCrAl and Material A-2 NiCrAl as a Function of Oxidation Time at 1832°F (1000°C)	12
7	Volume Growth of Material A-1 NiCrAl and Material A-2 NiCrAl as a Function of Oxidation Time at 1832°F (1000°C).	13
8	Microstructure of Virgin Material A-1 NiCrAl	14
9	Microstructure of Virgin Material A-2 NiCrAl	14
10	Microstructure of Material A-1 NiCrAl After 1000 Hours at 1600°F (871°C).	15
11	Microstructure of Material A-1 NiCrAl After 1000 Hours at 1832°F (1000°C)	17
12	Microstructure of Material A-2 NiCrAl After 1000 Hours at 1832°F (1000°C)	17
13	Microstructure of Material A-1 NiCrAl After 175 Hours at 1900°F (1040°C)	18
14	Microstructure of Material A-2 NiCrAl After 1200 Hours at 1922°F (1050°C)	18
15	Microstructure of Material A-2 NiCrAl After 290 Hours at 2012°F (1100°C)	19
16	Strength Retention of Material A-1 NiCrAl and Material A-2 NiCrAl as a Function of Oxidation Time at 1832°F (1000°C)	20

LIST OF FIGURES (Cont'd.)

<u>Figure</u>		<u>Page</u>
17	Strength Retention of Material A-1 NiCrAl and Material A-2 NiCrAl as a Function of Oxidation Time at 1900°F (1040°C)	22
18	Weight Gain of Material B-1 NiCrAl and Material B-2 NiCrAl as a Function of Oxidation Time at 1600°F (871°C)	24
19	Weight Gain of Material B-1 NiCrAl and Material B-2 NiCrAl as a Function of Oxidation Time at 1900°F (1040°C)	25
20	Volume Growth of Material B-1 NiCrAl and Material B-2 NiCrAl as a Function of Oxidation Time at 1600°F (871°C)	26
21	Volume Growth of Material B-1 NiCrAl and Material B-2 NiCrAl as a Function of Oxidation Time at 1900°F (1040°C)	27
22	Cyclic Oxidation Behavior of Material A-2 NiCrAl	28
23	Dynamic Oxidation Test Rig (Schematic)	30
24	Dynamic Oxidation Apparatus	31
25	Dynamic Oxidation Apparatus	31
26	Abradable Surface of Dynamic Oxidation Test Segment Prior to Testing	32
27	Support Surface of Dynamic Oxidation Test Segment Prior to Testing	32
28	Cooling Air Flow Rate as a Function of Time on the Dynamic Oxidation Test Rig	34
29	Micrograph of Dynamic Oxidation Test Structure After 500 Hours of Exposure	35
30	Pore Size Measurement Apparatus (Schematic)	36
31	Dynamic Oxidation Test Segment After 75 Hours at 1900°F (1040°C)	37
32	Dynamic Oxidation Test Segment After 185 Hours at 1900°F (1040°C)	37
33	Dynamic Oxidation Test Segment After 286 Hours at 1900°F (1040°C)	38

LIST OF FIGURES (Cont'd.)

<u>Figure</u>		<u>Page</u>
34	Dynamic Oxidation Test Segment After 430 Hours at 1900° F (1040° C)	38
35	Dynamic Oxidation Test Segment After 500 Hours at 1900° F (1040° C)	39
36	NiCrAl Particle From the Surface of the Dynamic Oxidation Test Segment After 500 Hours	40
37	Particle Erosion Test Apparatus	42
38	Weight Loss From Particulate Erosion as a Function of Material Strength	44
39	1650 psi (11.4 MPa) Material A-2 NiCrAl After Being Impinged by 25 g of No. 30 SiC Shot	45
40	1800 psi (12.4 MPa) Material A-1 NiCrAl After Being Impinged by 25 g of No. 30 SiC Shot	45
41	2150 psi (14.8 MPa) Material A-2 NiCrAl After Being Impinged by 25 g of No. 30 SiC Shot	46
42	2600 psi (17.9 MPa) Material A-1 NiCrAl After Being Impinged by 25 g of No. 30 SiC Shot	46
43	Average Decrease in Sample Thickness as a Function of the Quantity of SiC Impinged	47
44	Sample Weight Loss as a Function of Quantity of SiC Impinged	48
45	Decrease in Sample Thickness Along the Major Line of Impingement as a Function of the Quantity of SiC Impinged	49
46	1050 psi (7.2 MPa) UCAR Type AB-2 Material Subjected to 5 Hours of Impingement by No. 30 SiC	51
47	NiCrAl Bi-Layer After Being Impinged by No. 30 SiC for 5 Hours	52
48	NiCrAl Bi-Layer After Being Impinged by No. 30 SiC for 5 Hours	52
49	NiCrAl Bi-Layer After Being Impinged by No. 30 SiC for 5 Hours	53

LIST OF FIGURES (Cont'd.)

<u>Figure</u>		<u>Page</u>
50	NiCrAl Bi-Layer After Being Impinged by No. 30 SiC for 5 Hours	53
51	1650 psi (11.4 MPa) Material A-2 NiCrAl After a 0.030 in (762 μ m) Rub with an Inconel 600 Blade	55
52	2100 psi (14.5 MPa) Material A-2 NiCrAl After a 0.030 in (762 μ m) Rub with an Inconel 600 Blade	55
53	1800 psi (12.4 MPa) Material A-1 NiCrAl After a 0.030 in (762 μ m) Rub with an Inconel 600 Blade	56
54	2400 psi (16.5 MPa) Material A-1 NiCrAl After a 0.030 in (762 μ m) Rub with an Inconel 600 Blade	56
55	NASA Abradable Seal Test Apparatus	58
56	Frictional and Radial Load Results for Material A-2 NiCrAl of Different Strength Levels	61
57	Micrograph of the Leading Edge of an AM 355 Blade Tip After Interaction with Material A-2 NiCrAl	64
58	Micrograph of the Leading Edge of an AM 355 Blade Tip After Interaction with Material A-2 NiCrAl	64
59	Micrograph of the Leading Edge of an AM 355 Blade Tip After Interaction with Material A-2 NiCrAl	64
60	Micrograph of Material A-2 NiCrAl After Interaction with AM 355 Blade Tip	65
61	Micrograph of Material A-2 NiCrAl After Interaction with AM 355 Blade Tip	65
62	Large Particle Size Debris Collected After Rub Interaction Between AM 355 Blade Tips and Material A-2 NiCrAl	66
63	Fine Particle Size Debris Collected After Rub Interaction Between AM 355 Blade Tips and Material A-2 NiCrAl	66

LIST OF FIGURES (Cont'd.)

<u>Figure</u>		<u>Page</u>
64	Jet Exhaust Rig	68
65	Jet Exhaust Rig Nozzle and Test Segment	68
66	Jet Exhaust Rig (Schematic)	70
67	Cut Away View of Transpiration-Cooled Shroud Used in Contract F33615-76-C-2026	71
68	Transpiration-Cooled Shroud Initially Used in This Contract	71
69	Support Structure with Uniform Cooling Air Distribution	73
70	Support Structure with Uniform Cooling Air Distribution (Schematic)	73
71	Support Structure with Preferential Cooling to Lead Position	74
72	Support Structure with Preferential Cooling to Lead Position (Schematic)	74
73	Support Structure with Open Plenum Chamber at the Lead Edge (Schematic)	75
74	Support Structure with Two Open Plenum Chambers at the Lead Edge (Schematic)	76
75	Surface of Optimum Support Structure	77
76	Substrate of Optimum Support Structure	77
77	Optimum Support Structure (Schematic)	78
78	Surface Temperature Profile of the Shroud Segment with Uniform Cooling Air Supplied to Each Plenum Chamber	81
79	Surface Temperature Profile of the Shroud Segment with Preferential Cooling Supplied to the Lead Edge	82
80	Surface Cooling of the Shroud by Heat Conduction	84
81	Surface Cooling of the Shroud by Heat Conduction	85

LIST OF FIGURES (Cont'd.)

<u>Figure</u>		<u>Page</u>
82	Comparison of Surface Cooling Caused by Conduction for Porous Metal Segments Which Are Totally and Partially in Contact with the Support	86
83	Surface Temperature Profile of the Shroud Segment with Preferential Cooling to the Two Lead Plenum Chambers	87
84	Surface Temperature Profile of the Shroud Segment with the Optimized Support Structure Design	89
85	Lead Edge Protection for the Shroud	90
86	Design Change for the Optimized Rig Test Support Structure	91
87	Relocation of Cooling Air Injection Orifices in the Optimized Support Structure	92
88	Shroud Segment with Three Functional Areas	94
89	Schematic of Test Segment Assembly for Jet Exhaust Rig	97
90	Hot Band Across the Surface of the Test Segment on the Jet Exhaust Rig	99
91	Location of Areas of Evaluation on the Test Shroud	101
92	Test Segment 3 Prior to Testing	103
93	Test Segment 3 After 60 Thermal Cycles	103
94	Lead Edge of Test Segment 3 Prior to Testing	104
95	Lead Edge of Test Segment 3 After 60 Thermal Cycles	104
96	Oxidation of Particle at the Lead Edge of Segment 3	105
97	Lead Surface of Test Segment 3 Prior to Testing	106
98	Lead Surface of Test Segment 3 After 60 Thermal Cycles	106
99	Lead Surface of Test Segment 1 After 100 Thermal Cycles	107

LIST OF FIGURES (Cont'd.)

<u>Figure</u>		<u>Page</u>
100	Lead Surface of Test Segment 2 Prior to Testing	108
101	Lead Surface of Test Segment 2 After 100 Thermal Cycles	108
102	Lead Surface of Test Segment 4 Prior to Testing	109
103	Lead Surface of Test Segment 4 After 100 Thermal Cycles	109
104	Micrograph of Lead Edge of Segment 1	110
105	Micrograph of Lead Edge of Segment 2	111
106	Micrograph of Lead Edge of Segment 4	112
107	Particles at Lead Edge of Segment 4	113
108	Particles at the Lead Edge of the Flow Control Layer of Segment 2	114
109	Surface of Segment 1 After 100 Thermal Cycles	116
110	Surface of Segment 2 Prior to Testing	117
111	Surface of Segment 2 After 100 Thermal Cycles	117
112	Surface of Segment 4 Prior to Testing	118
113	Surface of Segment 4 After 100 Thermal Cycles	118
114	Particles at the Surface of Segment 4 Near the Lead Edge	119
115	Interface Between the Abradable and Flow Control Layer Near the Lead Edge	121
116	Interface Between the Abradable and Flow Control Layer Near the Trailing Edge	122
117	Lead Edge of Segment 1 After 100 Thermal Cycles	123
118	Microstructure of Segment 1 Showing the Braze Wicking	124
119	Microstructure of Segment 1 Showing the Braze Wicking	125
120	Lead Edge of Segment 2 Prior to Testing	126
121	Lead Edge of Segment 2 After 100 Thermal Cycles	126

LIST OF FIGURES (Cont'd.)

<u>Figure</u>		<u>Page</u>
122	Microstructure of Lead Edge of Segment 2 After 100 Thermal Cycles	127
123	Lead Edge of Segment 4 Prior to Testing	128
124	Lead Edge of Segment 4 After 100 Thermal Cycles	128
125	Microstructure of Segment 4 After 100 Thermal Cycles	129
126	Surface Temperatures of Segment 1 with Various Cooling Air Flow Rates	132
127	Surface Temperatures of Segment 2 with Various Cooling Air Flow Rates	133
128	Surface Temperatures of Segment 4 with Various Cooling Air Flow Rates	134
129	Test Segment on Jet Exhaust Rig Showing the Cool Area Behind the Chamfered Surface	135
130	Location of Surface Temperature Taken on Segments Subject to Testing on the Jet Exhaust Rig	136
131	Thermocouple Location for Temperature Profile Measurements	138
132	Temperature Profile of Test Structure Oriented at a 30° Angle	139
133	Temperature Profile of Test Structure Oriented at a 45° Angle and with a Protected Lead Edge	141
134	Temperature Profile of Test Structure Oriented at a 45° Angle and No Protective Barrier at the Lead Edge	142

I. SUMMARY

The goal of this contract was to optimize rub tolerant porous structures made from nickel-chromium-aluminum*(NiCrAl) for use as a transpiration-cooled turbine shroud abradable seal. The optimized structure has been developed. The evaluation has shown that this NiCrAl structure is abradable and resists oxidation at 1900°F (1040°C) by forming a stable oxide surface coating during the first 100 hours of exposure. During the formation of the oxide coating, a minor reduction in the cooling gas flow rate occurs at a constant back pressure. After the coating has formed, the flow-pressure drop relationship remains constant. Although the flow through the abradable layer can be stabilized by preoxidation, this is probably unnecessary as the major pressure drop in the optimized structure is across the support structure rather than the abradable layer. However, preoxidation also enhances particulate erosion resistance. After 100 hours of oxidation the erosion is equivalent to UCAR** Type AB-2 (the comparative material). A NiCrAl coated support structure, tested in a 2600°F gas stream at 0.7 Mach, has demonstrated that the most efficient cooling was achieved by preferential cooling of the lead edge of the shroud segment. Under the same test conditions it was demonstrated that the segment was mechanically stable and does not require the use of a stronger porous intermediate layer, between the NiCrAl and the support structure. Thermal stability of the braze and sinter bonded areas has also been attained. Therefore, in addition to meeting the goal of optimizing the rub tolerant layer, a practical support structure to which it can be applied has also been successfully evaluated.

* The nickel-chromium-aluminum (NiCrAl) abradable structure referred to throughout this report was made by a proprietary process developed and reduced to practice by Union Carbide Corporation at its own expense.

** UCAR is a registered trademark of Union Carbide Corporation.

II. INTRODUCTION

Present high pressure turbine shrouds do not have a rub-tolerant capability. If the turbine blade rubs against the outer shroud, severe blade wear or damage could result. The application of rub tolerant materials to high pressure turbine shrouds will permit reduction of the blade to shroud clearances and will result in a more stable performance of the engine.

To produce a rub-tolerant seal, the seal must be readily crushed, cut, or abraded when contacted by the rotating member of the engine. Union Carbide's past experience has shown that a structure designed to be abradable will perform better than any other structure for this application. Abradability occurs when the rotating component makes contact with the abradable material and removes individual particles by cleanly breaking the bonds connecting them to adjacent particles. A distended structure permits the particles to readily escape from the rub area. This process results in little or no heat generation (expenditure of energy) and low blade wear.

The requirements for a satisfactory abradable seal in the high pressure turbine are not easily met, since the temperatures encountered are high enough to rapidly degrade most porous alloy metal structures. Denser structures which incorporate cooling schemes are sometimes used, but these structures have limited rub tolerance. Porous metal structures with acceptable abradability can be cooled in a similar manner but are generally less oxidation resistant.

Previous work by Union Carbide under USAF Contract F33615-76-C-2026 demonstrated the feasibility of the UCAR approach by using a NiCrAl porous abradable layer supported on a denser porous nickel-chromium (NiCr) layer. By passing sufficient cooling air into the shroud and distributing it through the porous structure, the structure could hold a surface temperature of 1900°F (1040°C) while exposed to a 2600°F (1430°C) gas stream. Although that program demonstrated the feasibility of using a porous NiCrAl structure, it did not address itself to optimization of the structure for engine applications.

This program addressed itself to the optimization of the coated shroud assembly. The abradable material was optimized for abrasability, oxidation resistance, erosion resistance, and gas flow stability. The support structure was optimized for efficient use of the cooling gas and the total shroud assembly was optimized for fabrication simplicity and structural stability. The coated shroud was tested under gradient conditions simulating those anticipated in the engine.

III. ABRADABLE MATERIAL OPTIMIZATION

Abradability, erosion, and oxidation tests were the three major tests used to optimize the abradable member of the high pressure turbine shroud. The following sections summarize these tests.

1. Static Oxidation

The addition of aluminum (Al) to the basic NiCr alloys enhances the oxidation resistance of the resultant alloys. The increased oxidation resistance is due to an adherent oxide shell which forms on the surface of the NiCrAl alloy particles. This shell, which is basically aluminum oxide (Al_2O_3) (nickel and chrome oxides are also present), will start to form or repair itself almost instantaneously under oxidizing conditions and is very stable. A family of alloys based on this technology is available in the market. However, these alloys are not all optimized for the same application. The alloy used in the Union Carbide abradable seal has been optimized for use as a porous structure. In general, this application requires a higher Al content to avoid depletion during the formation of the oxide shell. As shown in Figure 1, the relationship between the oxidation resistance of the porous structure and the Al concentration is not linear and the maximum oxidation resistance occurs when approximately 11 weight percent Al is added.

The material which results from the addition of approximately 11 percent Al to NiCr is composed of several solid solution phases. These are listed in Table 1. The phase boundaries for this NiCrAl composition are temperature dependent, and, as a result, the phases listed do not all occur at the same time. At the fabrication temperature, β and γ are the equilibrium phases of the NiCrAl (11 percent Al) composition. However, when the temperature is lowered to 1900°F (1040°C), the β phase is no longer an equilibrium phase. Diffusion to equilibrium at 1900°F (1040°C) for extensive periods of time yields the phases γ and γ' .

Prolonged uses of the material at these temperatures will gradually deplete the structure of Al, the major metal constituent of the oxide shell. As a result of this depletion, the composition will eventually move out of the two phase field, γ plus γ' , and into the single phase field of γ .

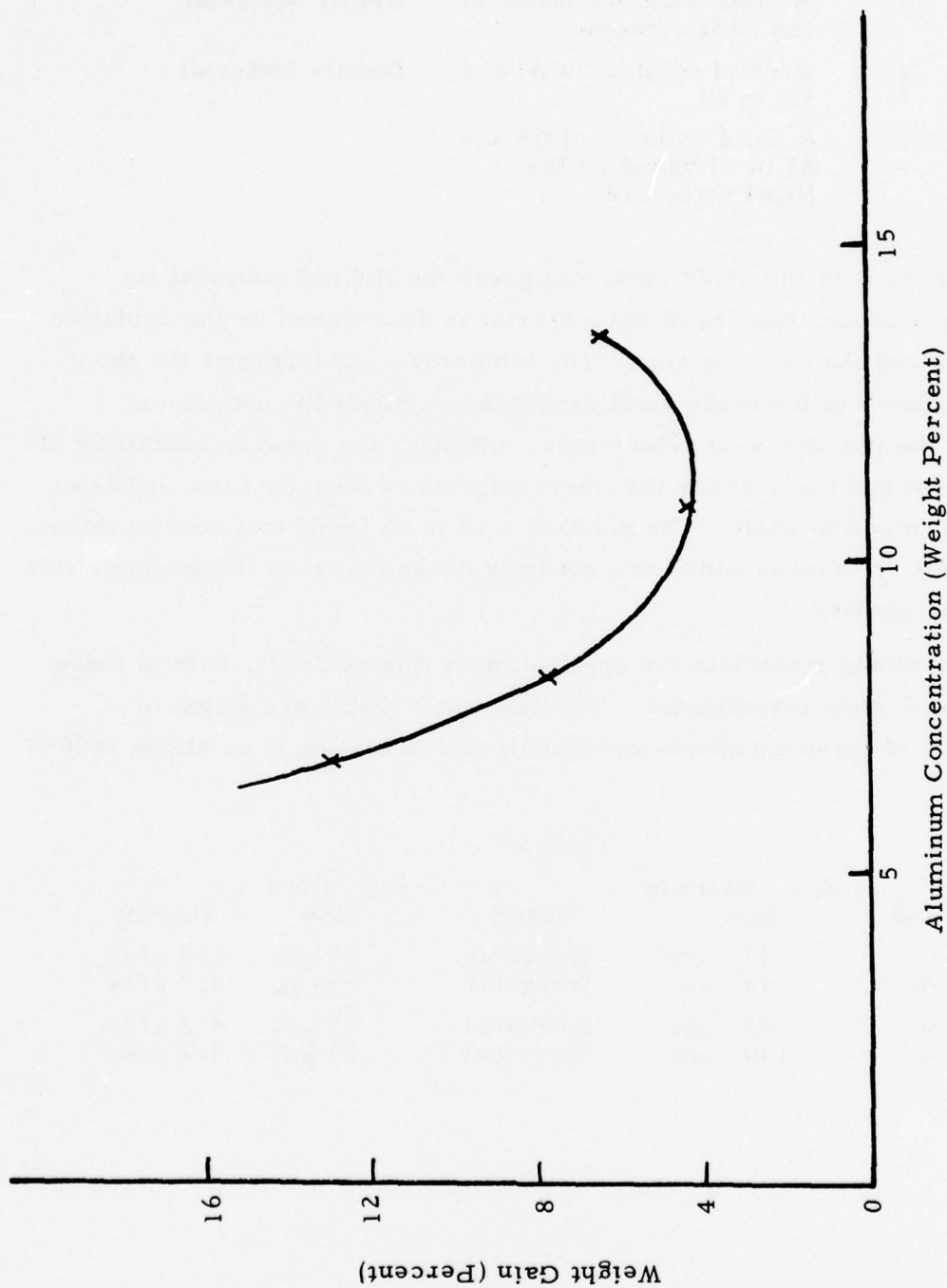


Figure 1: Oxidation Weight Gain After 500 Hours at 1832° F
(1000°C) as a Function of Aluminum Concentration

Table 1

Phase	Composition	Comments
β	A solid solution based on the NiAl structure	Brittle Material
γ	A solid solution of Al and Cr in Ni	Ductile Material
γ'	A solid solution of Cr and Al in Ni based on the Ni ₃ Al structure	

Because it is the oxide shell that gives the NiCrAl material its oxidation resistance, the life of the material is determined by the oxidation temperature and the particle size. The temperature determines the thickness and stability of the oxide shell required to protect the underlying material. The particle size determines, initially, the reserve quantities of the Al present and the quantity that must migrate to initially form and later repair the protective shell. The particle size is an important consideration, especially for structures which are not fully dense, such as those which have abradable properties.

To evaluate materials for application in this contract, both of these considerations were investigated. The materials tested are listed in Table 2. All of these materials were subjected to testing at or above 1600°F (871°C).

Table 2

Material	Avg. Particle Size	Shape	Avg. Pore Size	Density
A-1	85 μm	Irregular	65 μm	2.8 g/cc
A-2	145 μm	Irregular	95 μm	2.7 g/cc
B-1	85 μm	Spherical	27 μm	4.3 g/cc
B-2	130 μm	Spherical	35 μm	4.2 g/cc

Material A - Materials A-1 and A-2 were subjected to static oxidation testing at various temperatures between 1600°F (871°C) and 2012°F (1100°C). The weight gain and volume growth data for these tests are presented graphically in Figures 2 through 5. Although the initial rate of oxidation is high, the rate is significantly reduced after 150 hours for temperatures up to slightly greater than 1900°F (1040°C). However, as shown in Figures 4 and 5, excessive oxidation rates occurred at 2012°F (1100°C).

The parabolic type of curve shown in these figures is characteristic of the oxidation process for this NiCrAl system. As the process begins, there is a rapid oxidation of the particle surfaces. After an adherent oxide film has formed around the particles, the oxidation rates begin to decrease. Once an oxide shell of sufficient thickness has developed, the oxidation rates either level off or continue to increase but at a more gradual rate, dependent upon the oxidation temperature.

A direct comparison between A-1 and A-2 was made at 1832°F (1000°C) (see Figures 6 and 7). Material A-1 with the larger surface area-to-volume ratio (smaller particle size) shows more oxidation than Material A-2.

Figures 8 and 9 show typical virgin microstructures of structures A-1 and A-2 respectively. As is characteristic of this NiCrAl system, a two-phase structure exists. The rimming phase, β , is very evident in the inter-particle bond areas.

The effect of long-term oxidation upon the microstructure is shown in Figures 10 through 15. Figure 10 shows the microstructure of A-1 after 1000 hours at 1600°F (871°C). A thin oxide shell, which gives the NiCrAl its oxidation resistance, has formed around the individual particles. No signs of internal oxidation were evident, and degradation of the interparticle bond areas was minimal. No other oxidation experiments were conducted at this temperature.

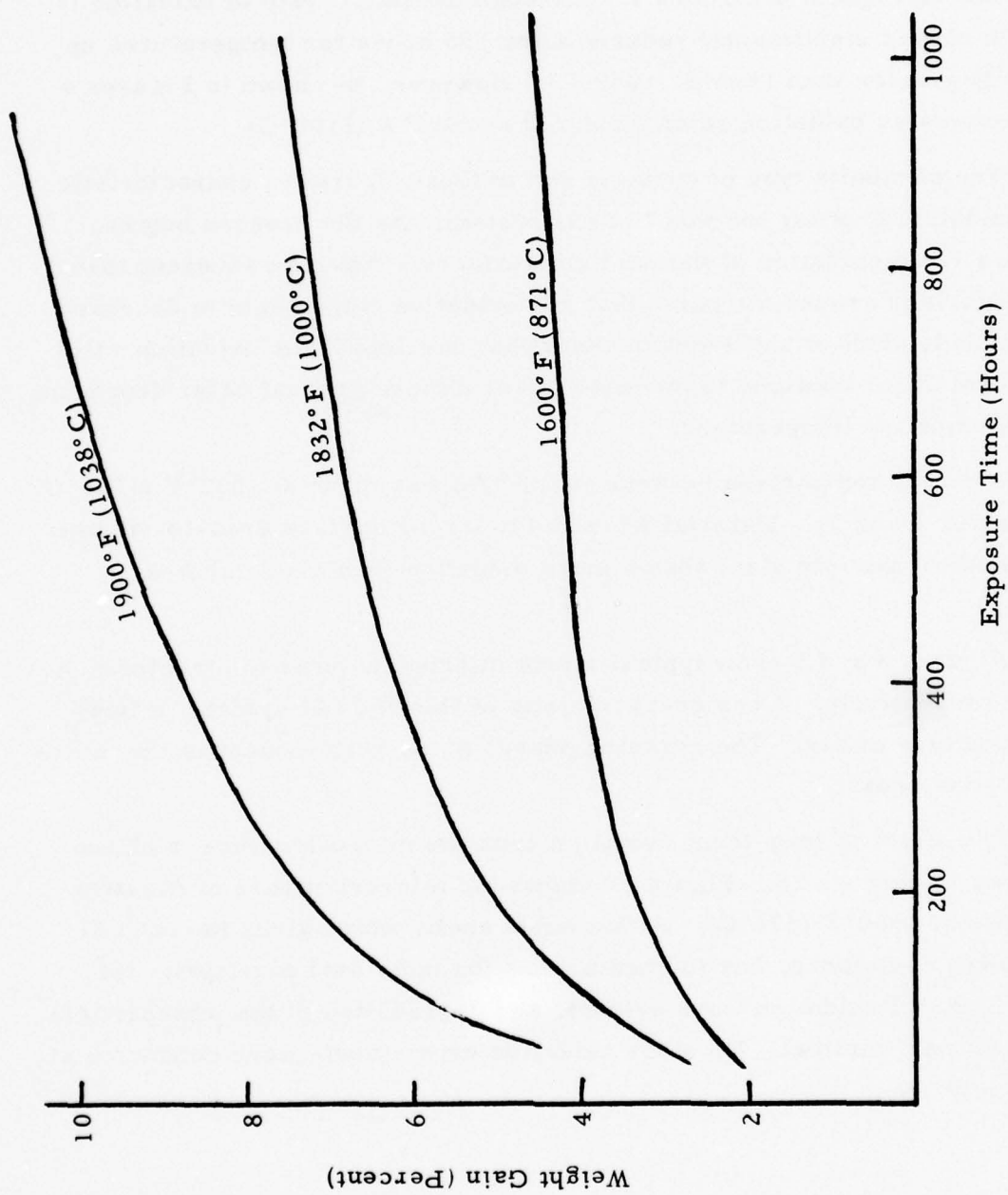


Figure 2: Weight Gain of Material A-1 NiCrAl with Temperature as a Function of Oxidation Time

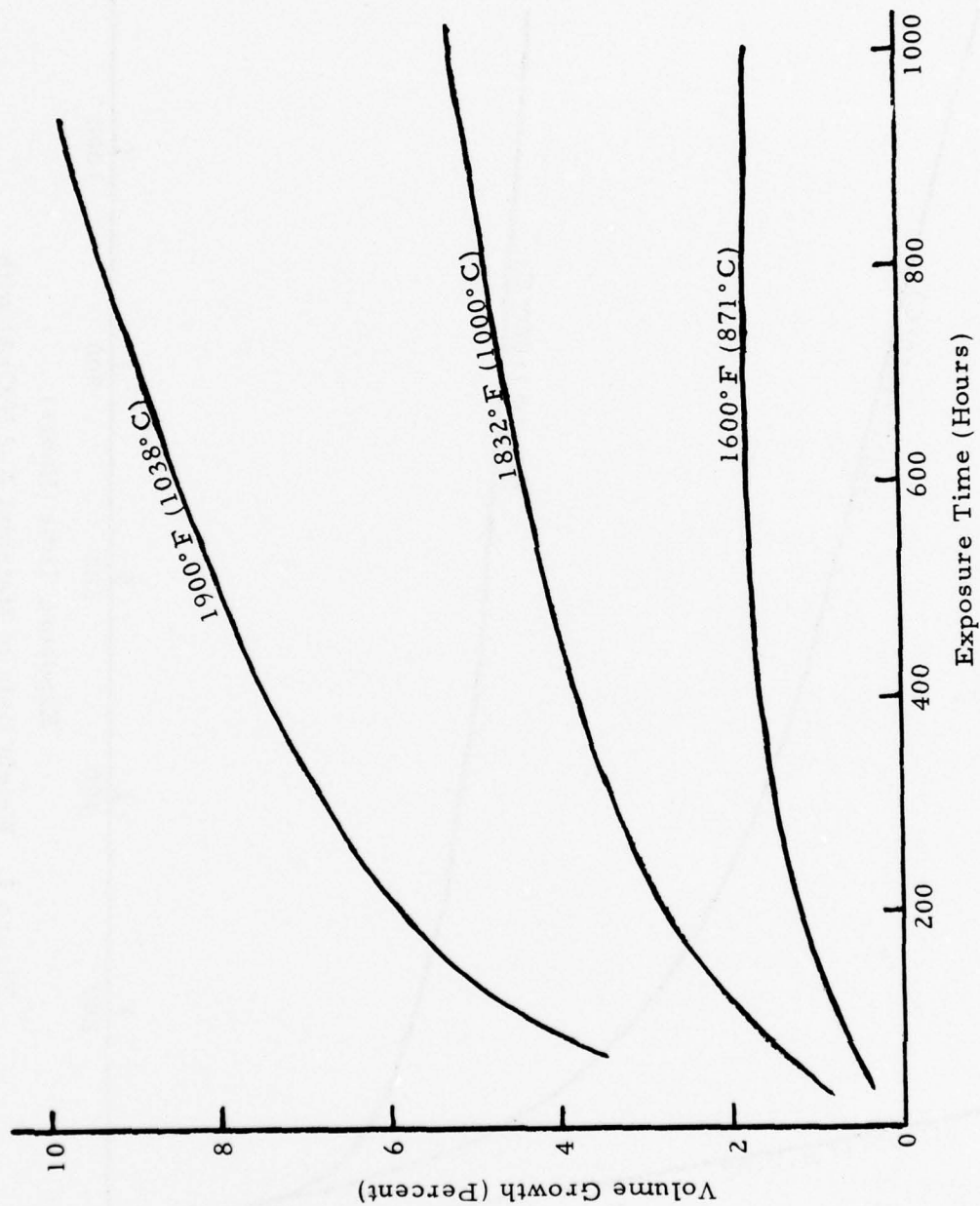


Figure 3: Volume Growth of Material A-1 NiCrAl with Temperature as a Function of Oxidation Time

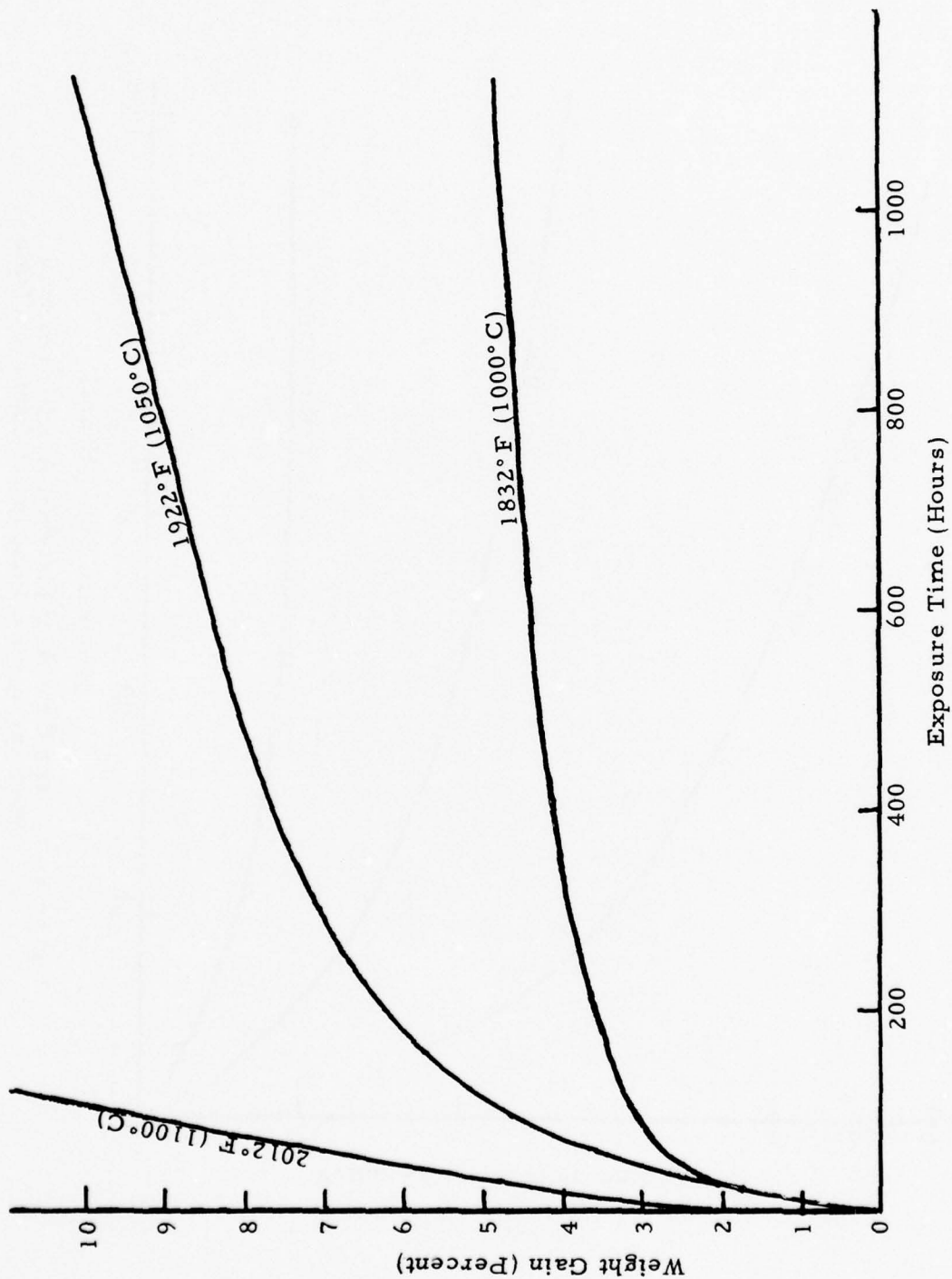


Figure 4. Weight Gain of Material A-2 NiCrAl with Temperature as a Function of Oxidation Time

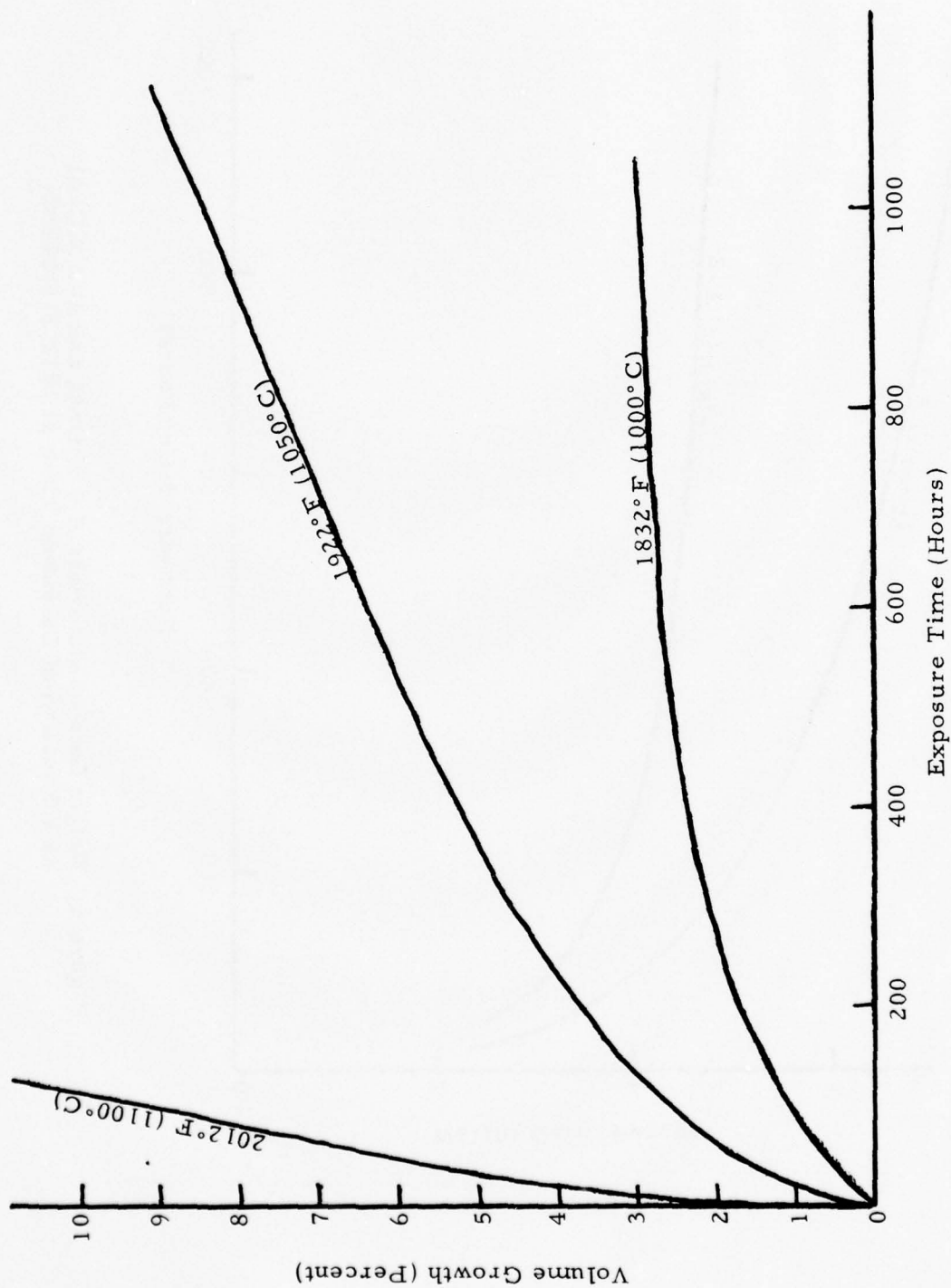


Figure 5: Volume Growth of Material A-2 NiCrAl with Temperature as a Function of Oxidation Time

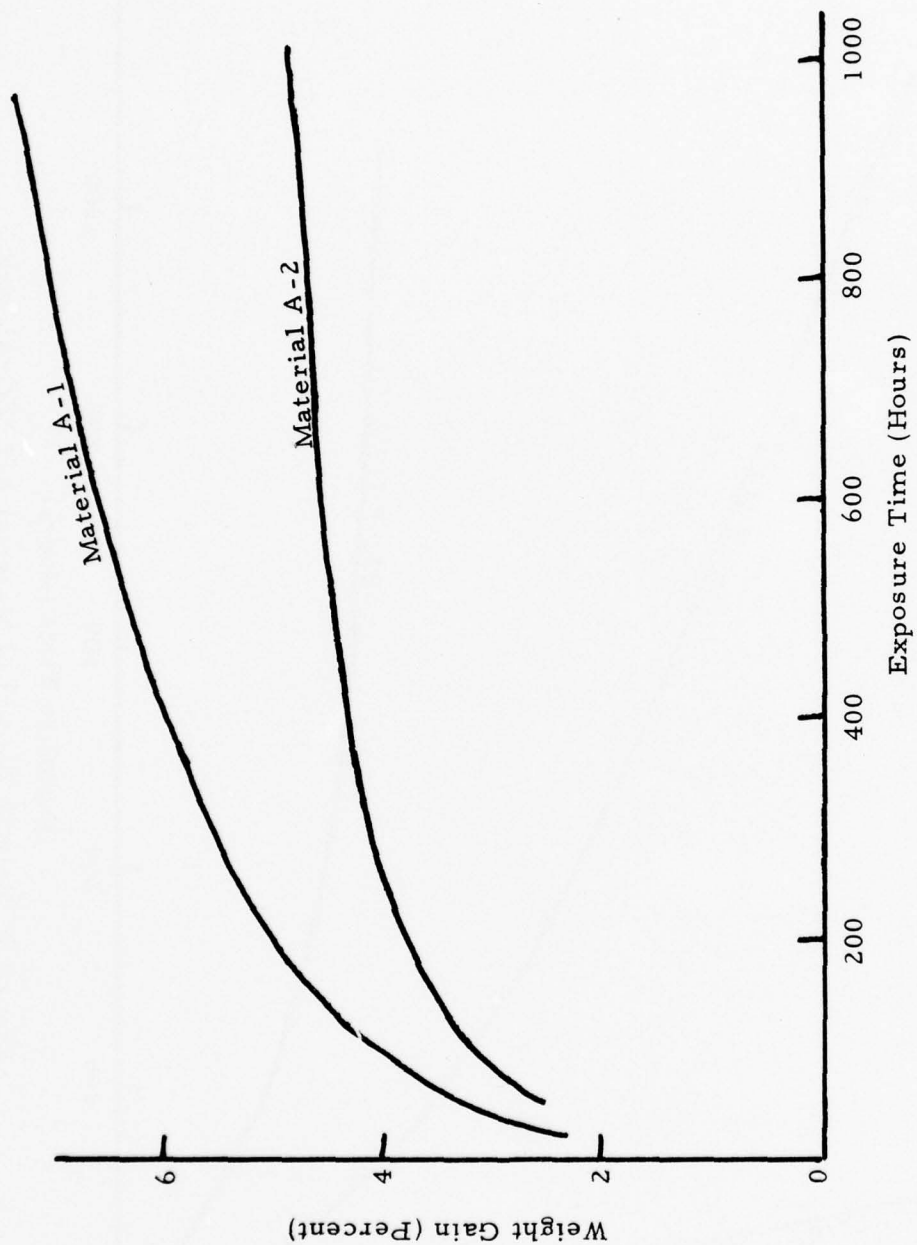


Figure 6: Weight Gain of Materials A-1 NiCrAl and A-2 NiCrAl as a Function of Oxidation Time at 1832°F (1000°C)

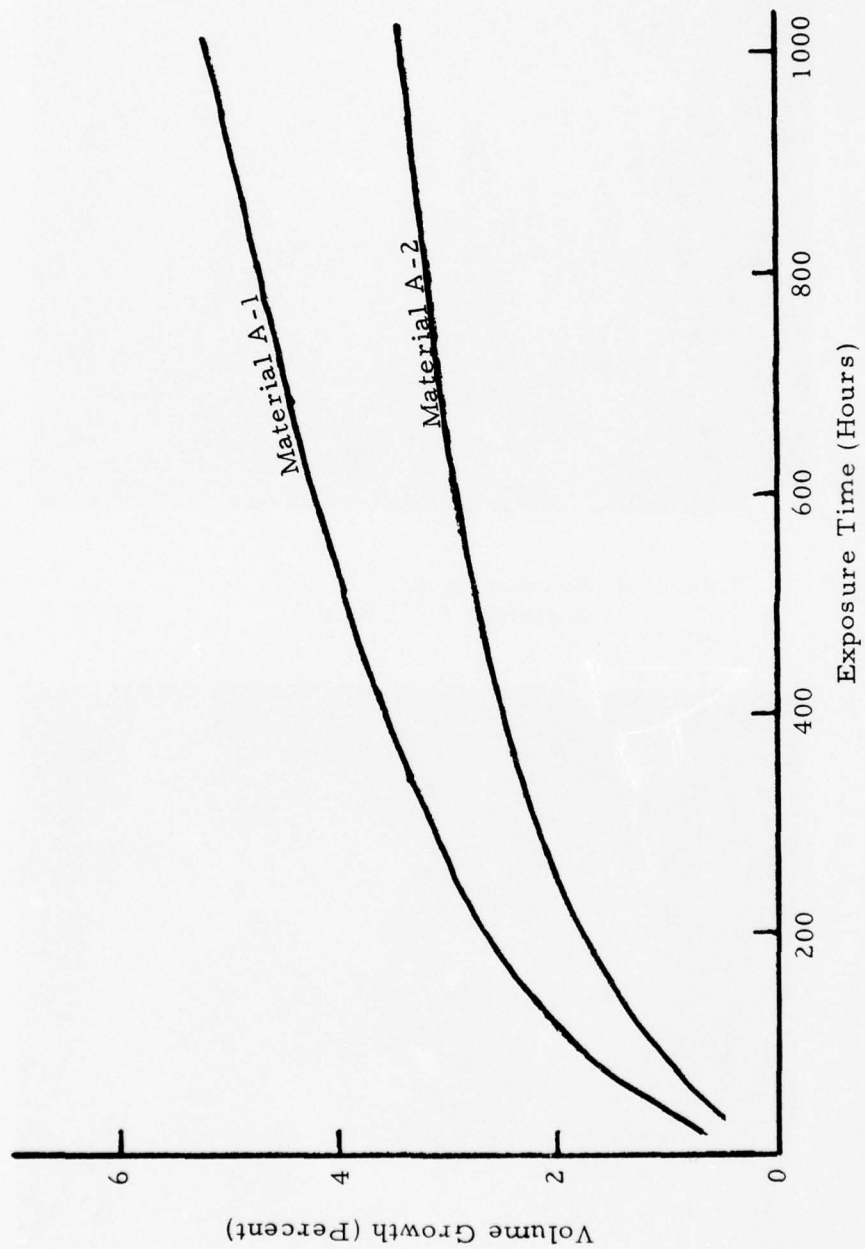


Figure 7: Growth of Materials A-1 NiCrAl and A-2 NiCrAl as a Function of Oxidation Time at 1832°F (1000°C)

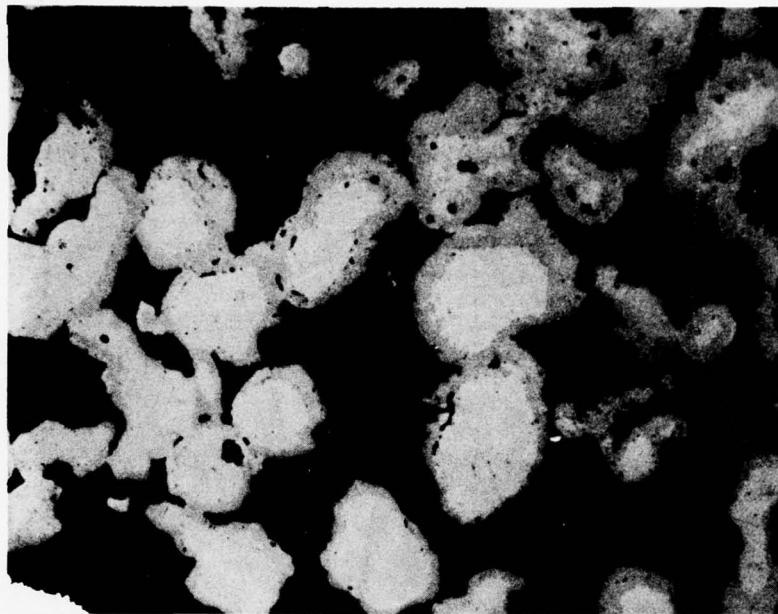


Figure 8: Microstructure of Virgin
Material A-1 NiCrAl 200X

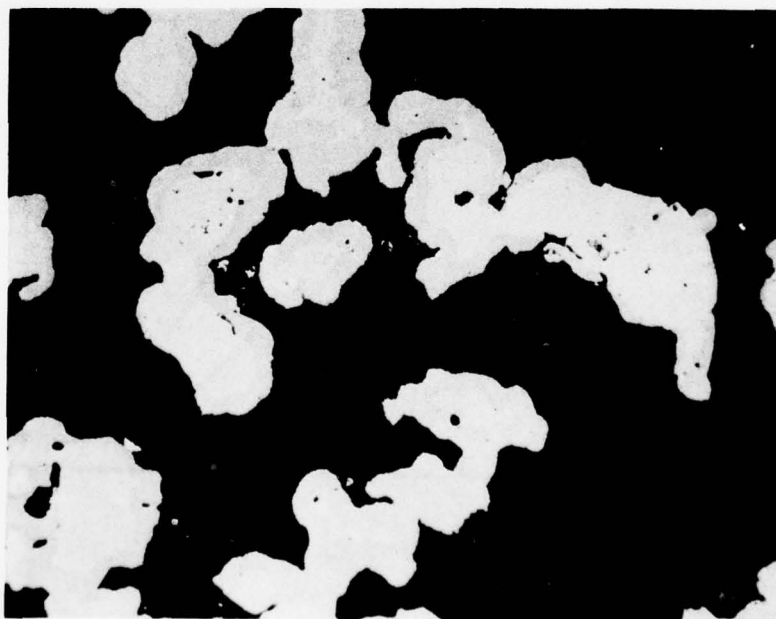


Figure 9: Microstructure of Virgin
Material A-2 NiCrAl 200X

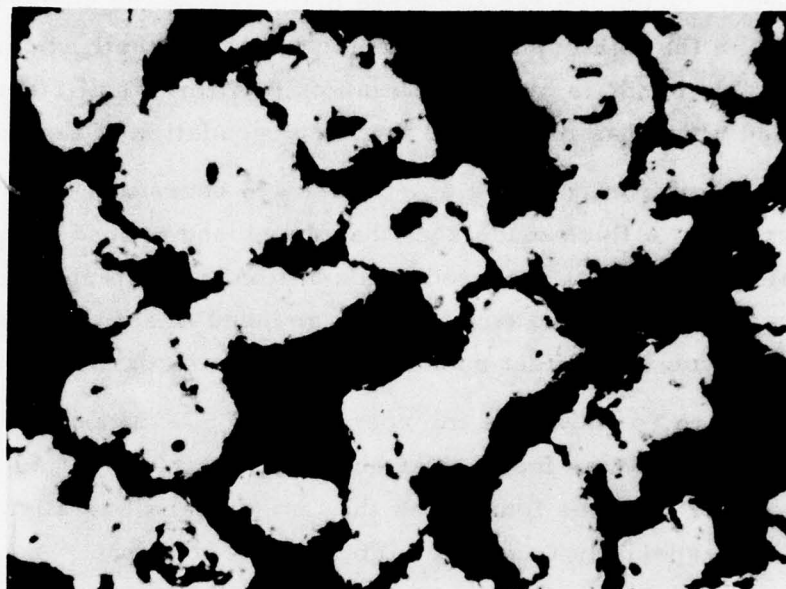


Figure 10: Microstructure of Material A-1 NiCrAl
After 1000 Hours at 1600°F (871°C) 200X

The effect of 1000 hours of static oxidation at 1832°F (1000°C) upon the A1 and A2 microstructures is shown in Figures 11 and 12, respectively. Insignificant amounts of internal oxidation have occurred throughout both structures. Oxidation has occurred primarily at the surface of the particles, resulting in the tightly adherent protective oxide shell. Some oxidation of the interparticle bonds is evident, but an oxide film of sufficient thickness has developed which has minimized further degradation of the bonds.

The microstructures of A1 after 475 hours at 1900°F (1040°C) is shown in Figure 13. A thick oxide shell has developed around the particles, and some internal oxidation has occurred. In addition, the interparticle bonds have become badly oxidized and considerably reduced in size. This condition has a pronounced adverse effect upon the tensile strength.

Figure 14 shows the microstructure of A2 after 1200 hours at 1922°F (1050°C). There was less oxidation damage to Material A2 than to A1, even though the A2 test was longer and the temperature was slightly higher. This result was especially true of the interparticle bonds.

Figure 15 shows a microstructure of A2 which has received 290 hours of oxidation at 2012°F (1100°C). The observed oxide layer is extensive and appears to be only loosely attached to the particles. Some internal oxidation has occurred.

The ability of NiCrAl structures to successfully withstand long-term oxidation has been demonstrated by their excellent strength retention at elevated temperatures. Figure 16 compares the strength retention curves of A1 and A2 after 1000 hours at 1832°F (1000°C). Both structures exhibit similar strength retention abilities; a gradual tensile strength increase is followed by a gradual decrease. The A2 structure has stabilized at close to its virgin tensile strength level after 1000 hours at 1832°F (1000°C), and the A1 structure appears to be decreasing in strength at a slow rate after this time interval.

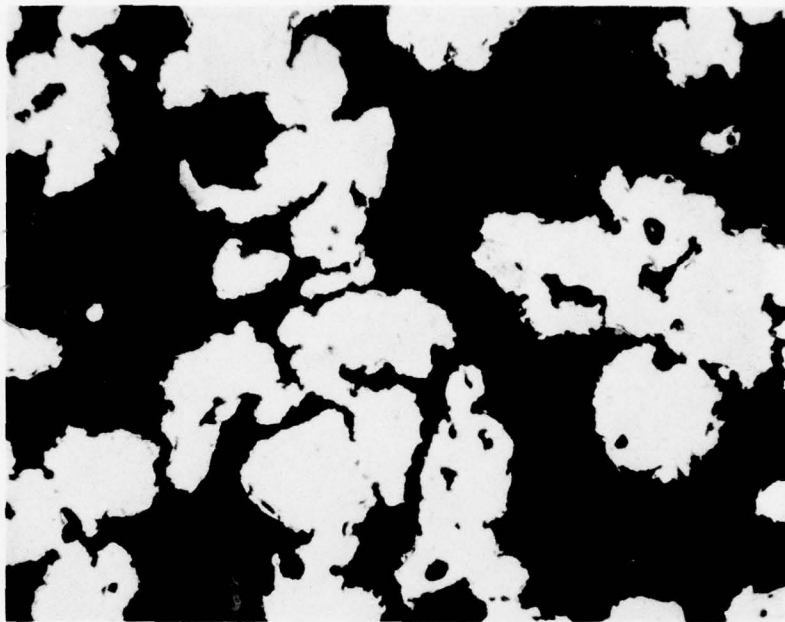


Figure 11: Microstructure of Material A-1 NiCrAl After
1000 Hours at 1832°F (1000°C) 200X

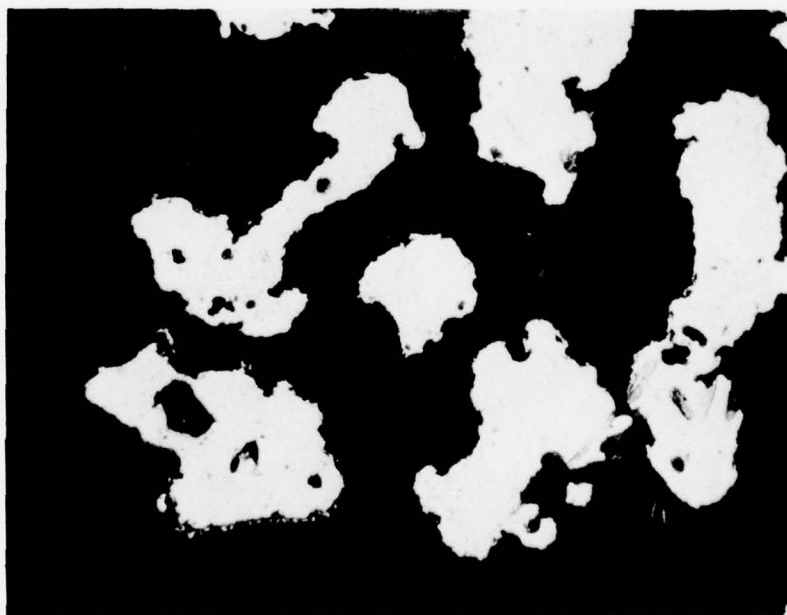


Figure 12: Microstructure of Material A-2 NiCrAl After
1000 Hours at 1832°F (1000°C) 200X

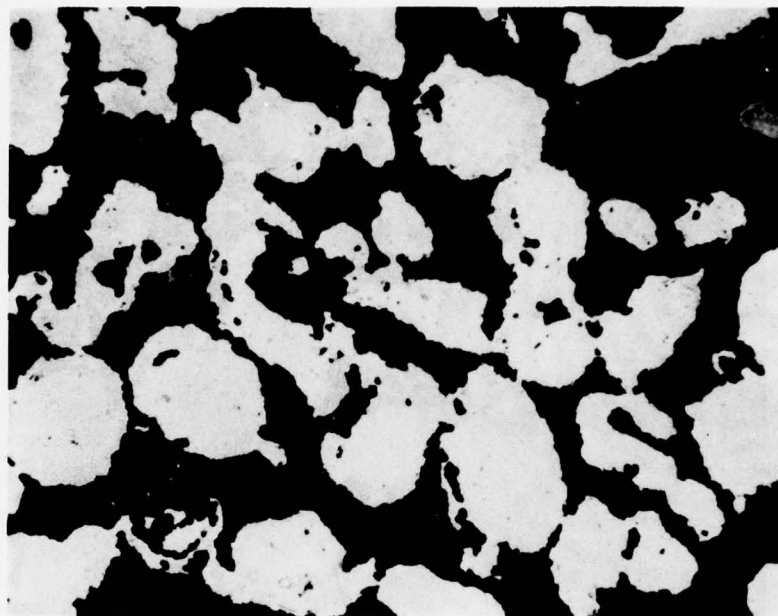


Figure 13: Microstructure of Material A-1 After
175 Hours at 1900°F (1040°C) 200X

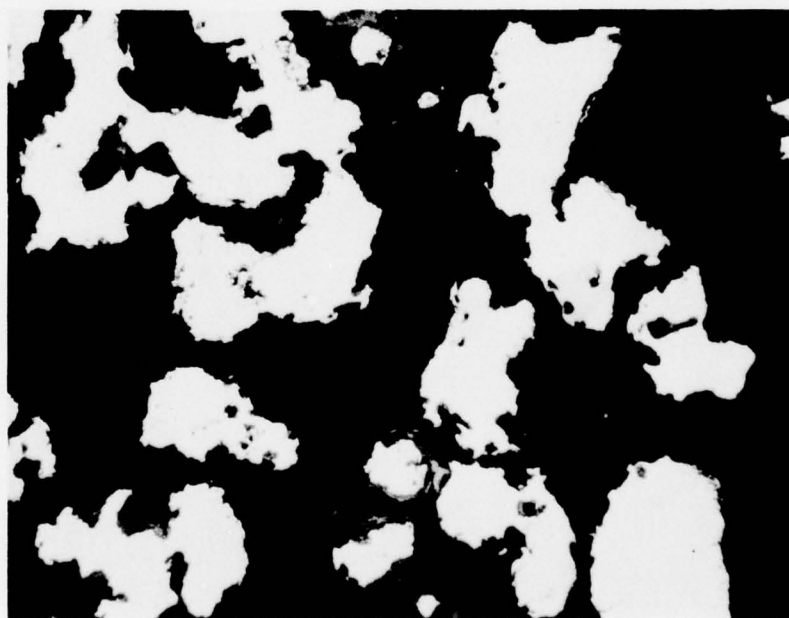


Figure 14: Microstructure of Material A-2 NiCrAl After
1200 Hours at 1922°F (1050°C) 200X

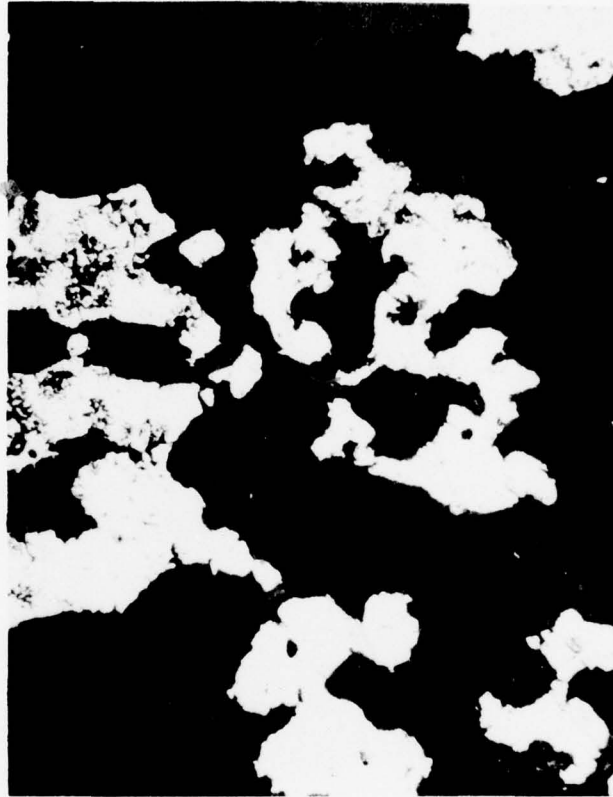


Figure 15: Microstructure of Material A-2 NiCrAl After
290 Hours at 2012° F (1100° C) 200X

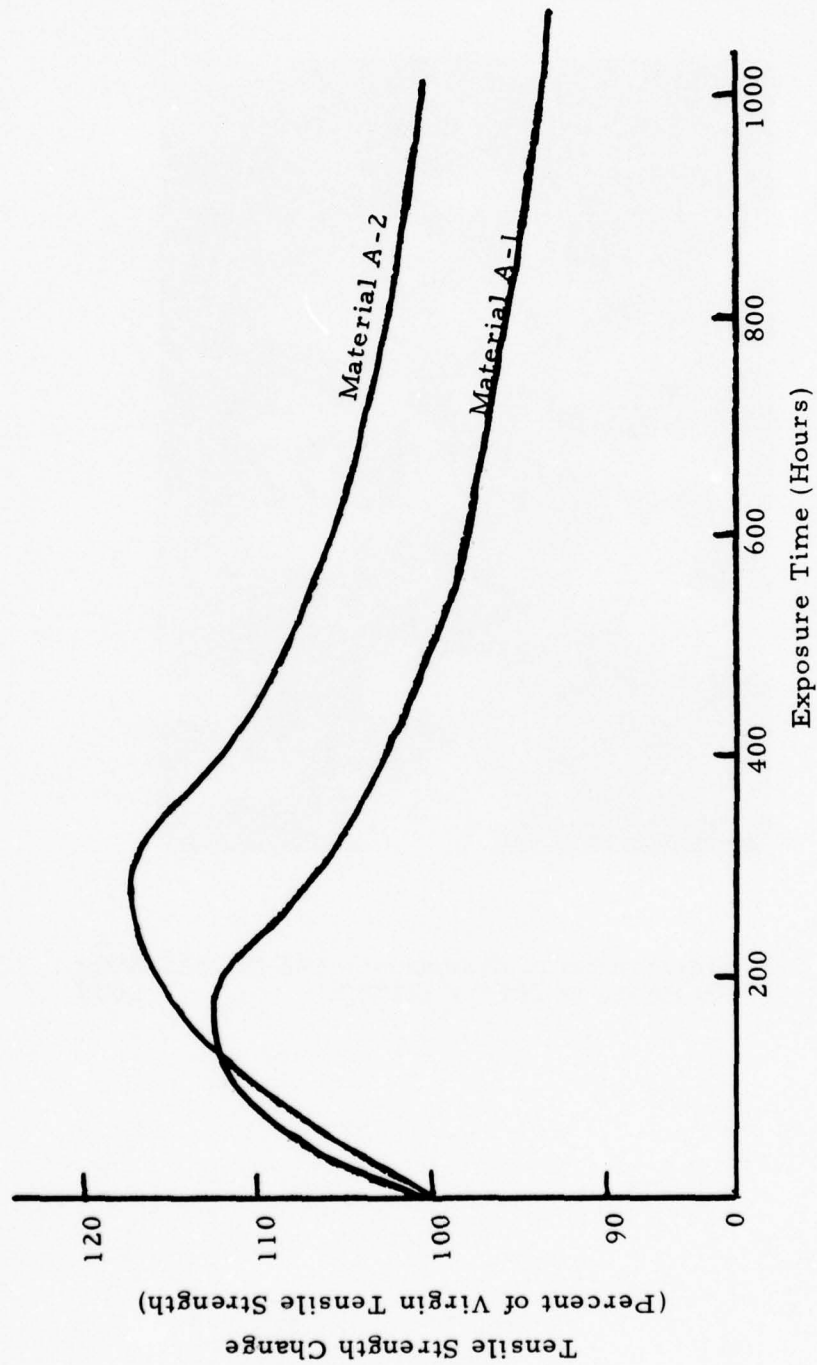


Figure 16: Effect of Oxidation Time at 1832°F (1000°C) on the Strength Retention of Materials A-1 NiCrAl and A-2 NiCrAl

A decrease in tensile strength retention occurs for both A-1 and A-2 materials with increasing oxidation temperatures. A similar tensile strength behavior to that observed at 1832°F (1000°C) occurred at 1900°F (1040°C), as shown in Figure 17 for structures A-1 and A-2. For the A-2 material, the strength leveled off at approximately 85% of its virgin strength. This strength retention was equally as good as that exhibited by the A-1 structure at 1832°F (1000°C). The A-1 material decreased in strength to approximately 65% of that which it had as virgin material.

A comparison of the two materials, A-1 and A-2, under static oxidation conditions showed that A-2 was the superior material. It had less weight gain, a smaller volume growth, and better strength retention than the A-1 material. Physical properties for Material A-2 are listed in Table 3.

Table 3

Composition: Nickel-Chromium-Aluminum alloy;
nominally 70 Ni - 20 Cr - 10 Al

True Density: 6.97 g/cc

Bulk Density: 2.5 - 2.8 g/cc

CTE (R. T. to 1832°F (1000°C); 10.2×10^{-6} in/in/°F (5.7×10^{-6} cm/cm/°C)

Thermal Diffusivity (α):	Room Temp.	1.10 mm ² /sec
	1470°F (800°C)	2.70 mm ² /sec

Ultimate Tensile Strength

Prior to Oxidation:	1700 psi	(11.7 MPa)
After 250 Hours at 1832°F (1000°C)	1985 psi	(13.7 MPa)
After 1000 Hours at 1832°F (1000°C)	1700 psi	(11.7 MPa)

Static Oxidation Volume Increase

After 1000 Hours at 1832°F (1000°C)	3.2%
After 1100 Hours at 1922°F (1050°C)	9.0%
After 300 Hours at 2012°F (1100°C)	23.7%

Static Oxidation Weight Gain

After 1000 Hours at 1832°F (1000°C)	4.6%
After 1100 Hours at 1922°F (1050°C)	10.0%
After 300 Hours at 2012°F (1100°C)	16.0%

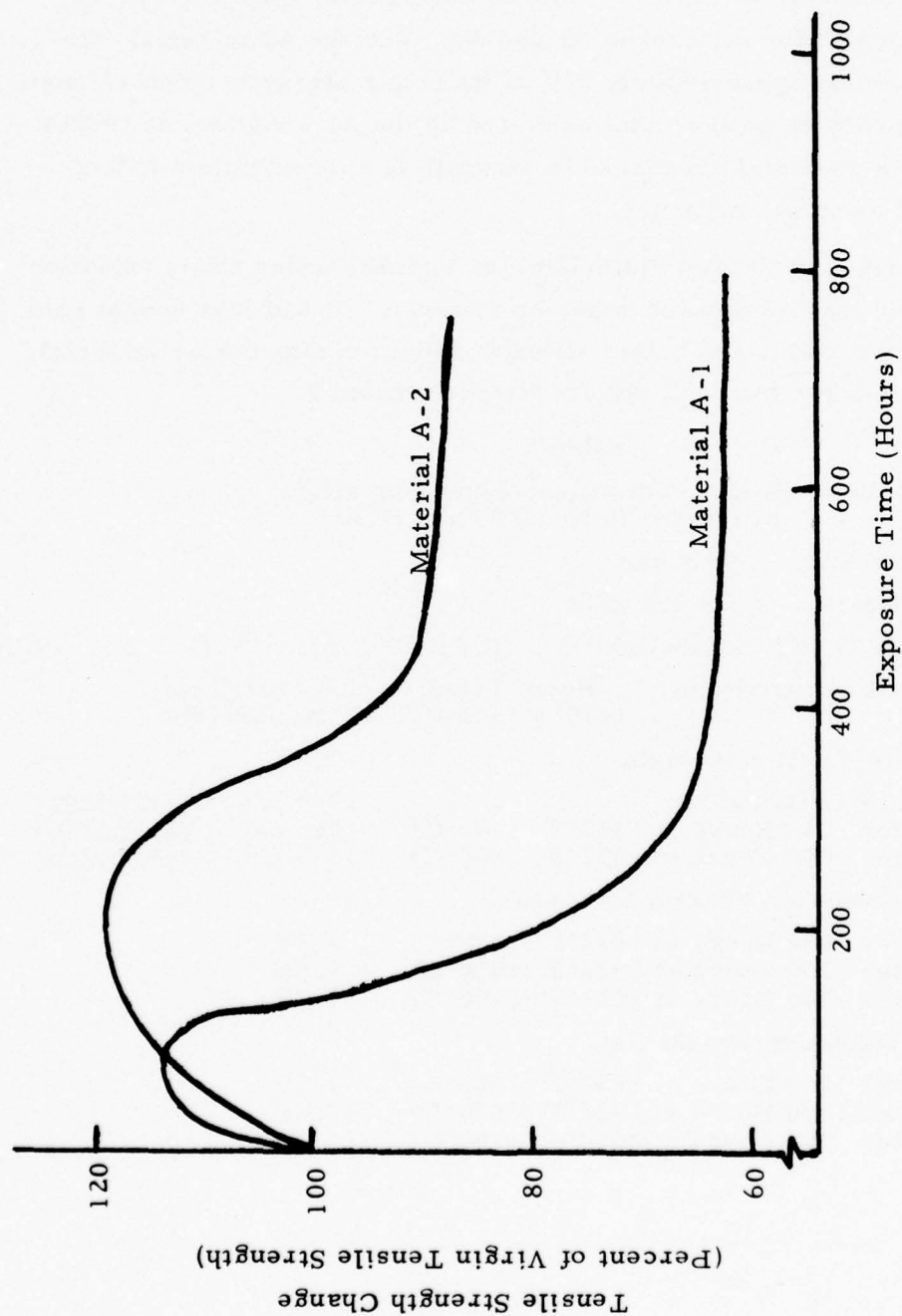


Figure 17: Effect of Oxidation Time at 1900°F (1040°C) on the Strength Retention of Materials A-1 NiCrAl and A-2 NiCrAl

Material B - Testing of Materials B1 and B2 was less extensive than testing of Materials A1 and A2. Most of the information generated was weight gain and volume growth data.

Static oxidation data for these two structures was taken at 1600°F (871°C) and 1900°F (1040°C). At 1600°F (871°C), there was an initial weight gain of 2.5% after 100 hours of exposure for both B1 and B2 (see Figure 18). An additional 1% weight gain occurred up to 550 hours.

A different trend emerged at 1900°F (1040°C). The weight gain curve, in Figure 19, shows that both B1 and B2 oxidize rapidly during the first 200 hours, followed by a slight decrease in their continued oxidation rate. However, B1 and B2 increased in weight by 12.7% and 11.5%, respectively, after 550 hours. These same basic trends are shown in the volume growth curves, Figures 20 and 21.

Static Oxidation Summary - A comparison of the two material types shows that the group A materials have superior oxidation resistance to the group B materials. Since this is especially important at the abradable surface where the temperatures are the highest, Material A2 (the better of the two A materials) was selected for further testing. These tests included dynamic oxidation, particle erosion, and abrasability. The other materials were maintained as possible candidates for use as the flow control layer of the shroud.

2. Cyclic Oxidation

Material A2 was subjected to cyclic oxidation testing at 1832°F (1000°C). Two types of cyclic test were used. In the first type, the segments were held at 1832°F (1000°C) for 5 minutes followed by 5 minutes at room temperature. This process was repeated for 1275 cycles. In the second type of test, the samples were held for at least 2 hours at 1832°F (1000°C) before bringing them to room temperature. In both cases, cooling was achieved by removing the segments from the hot furnace and allowing them to air cool. The segments were not quenched. The results of both of these tests are shown in Figure 22. Within the limits of experimental error, the curves approximate the static oxidation curve.

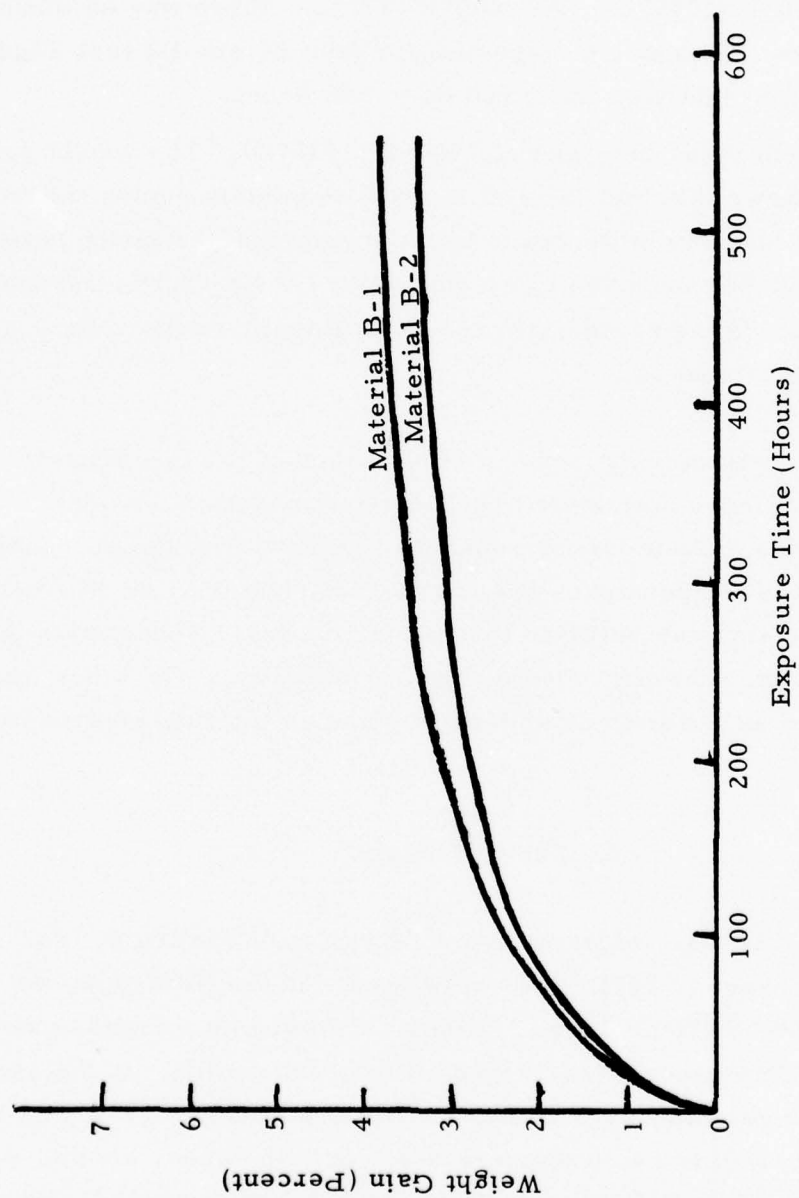


Figure 18: Weight Gain of Materials B-1 NiCrAl and B-2 NiCrAl as a Function of Oxidation Time at 1600° F (871°C)

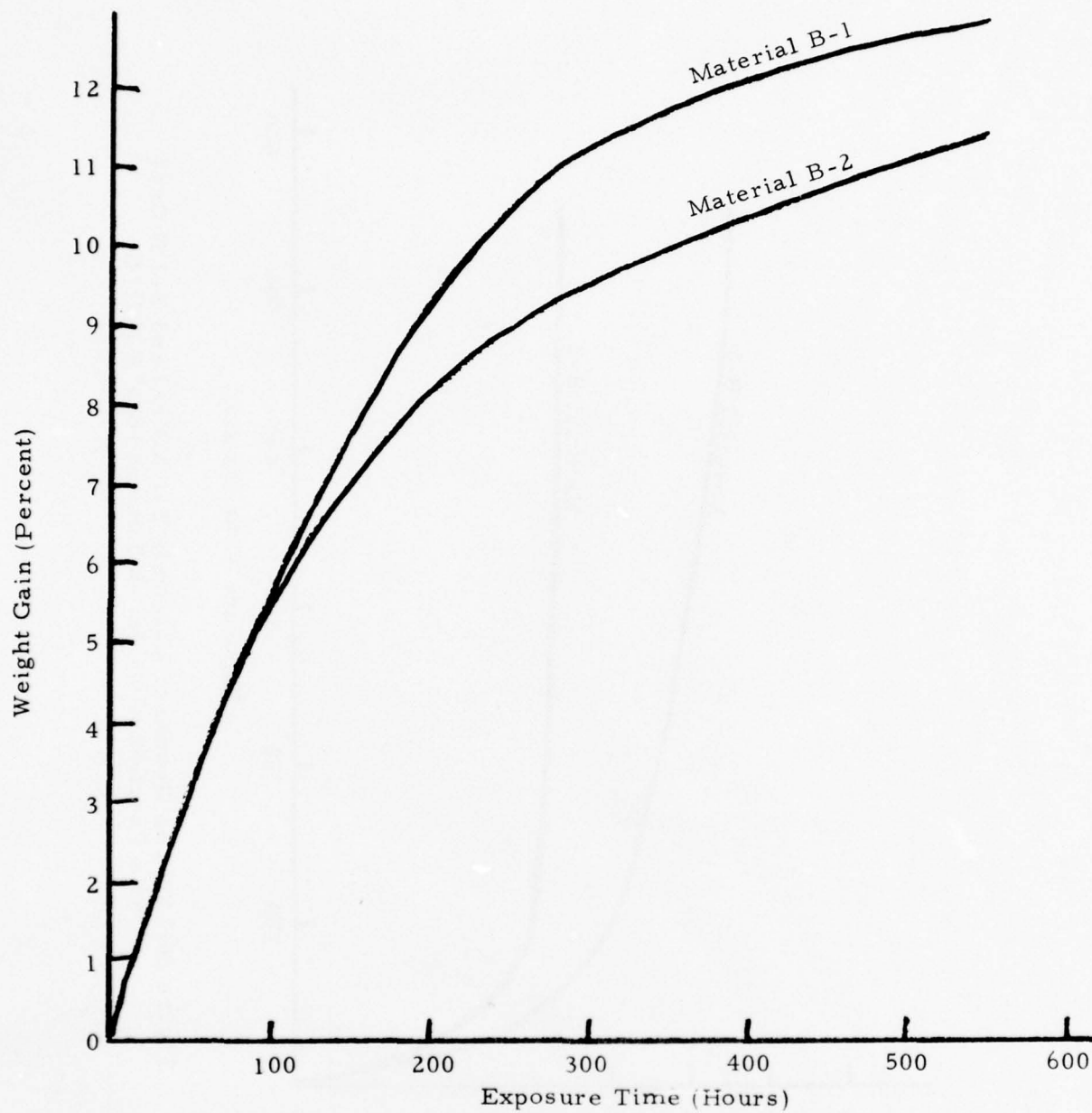


Figure 19: Weight Gain of Materials B-1 NiCrAl and B-2 NiCrAl as a Function of Oxidation Time at 1900° F (1040° C)

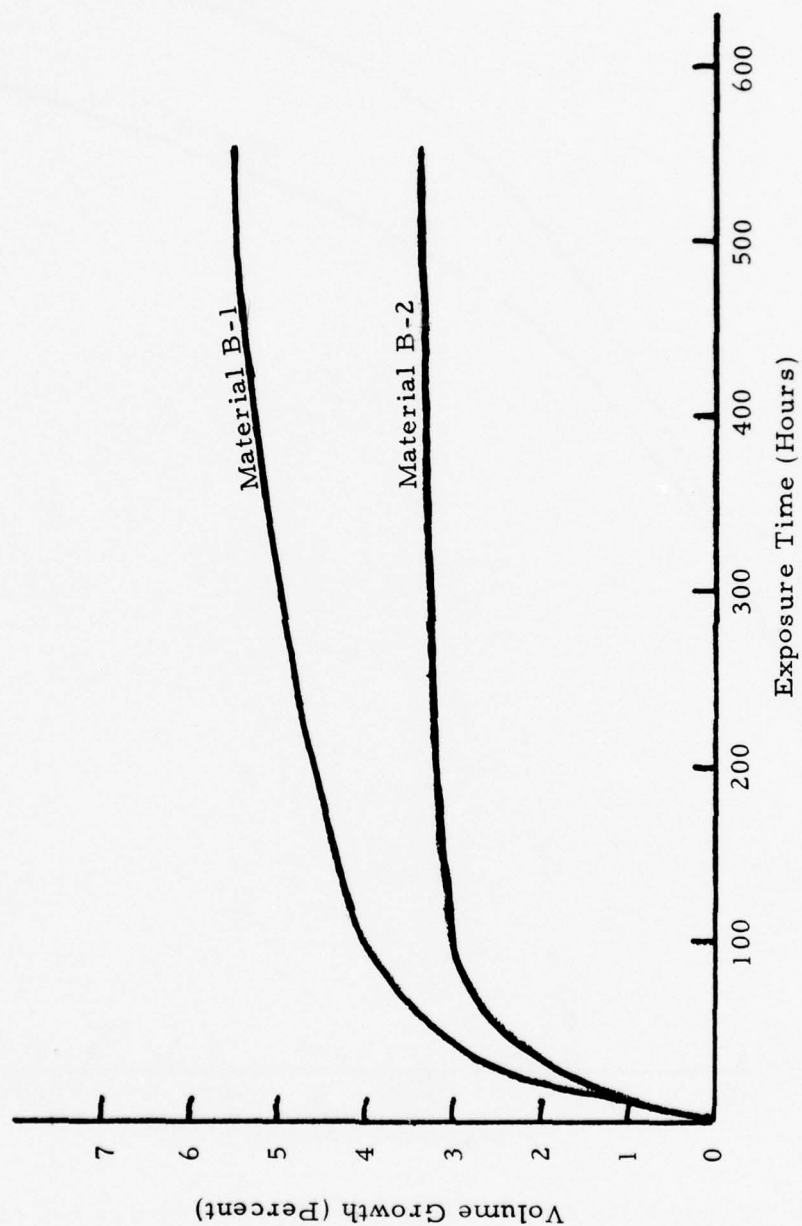


Figure 20: Volume Growth of Materials B-1 NiCrAl and B-2 NiCrAl as a Function of Oxidation Time at 1600°F (871°C)

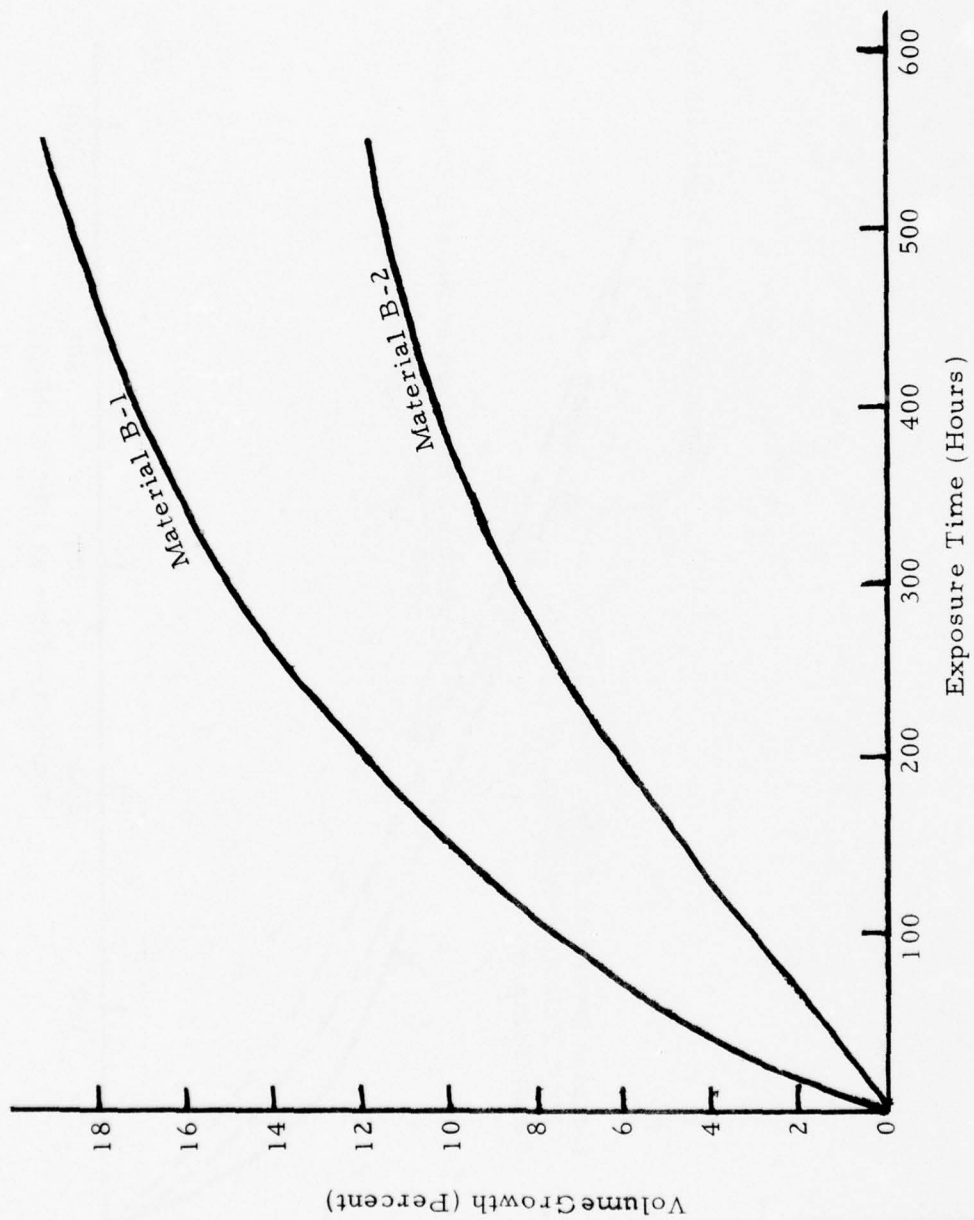


Figure 21: Volume Growth of Materials B-1 NiCrAl and B-2 NiCrAl as a Function of Oxidation Time at 1900°F (1040°C)

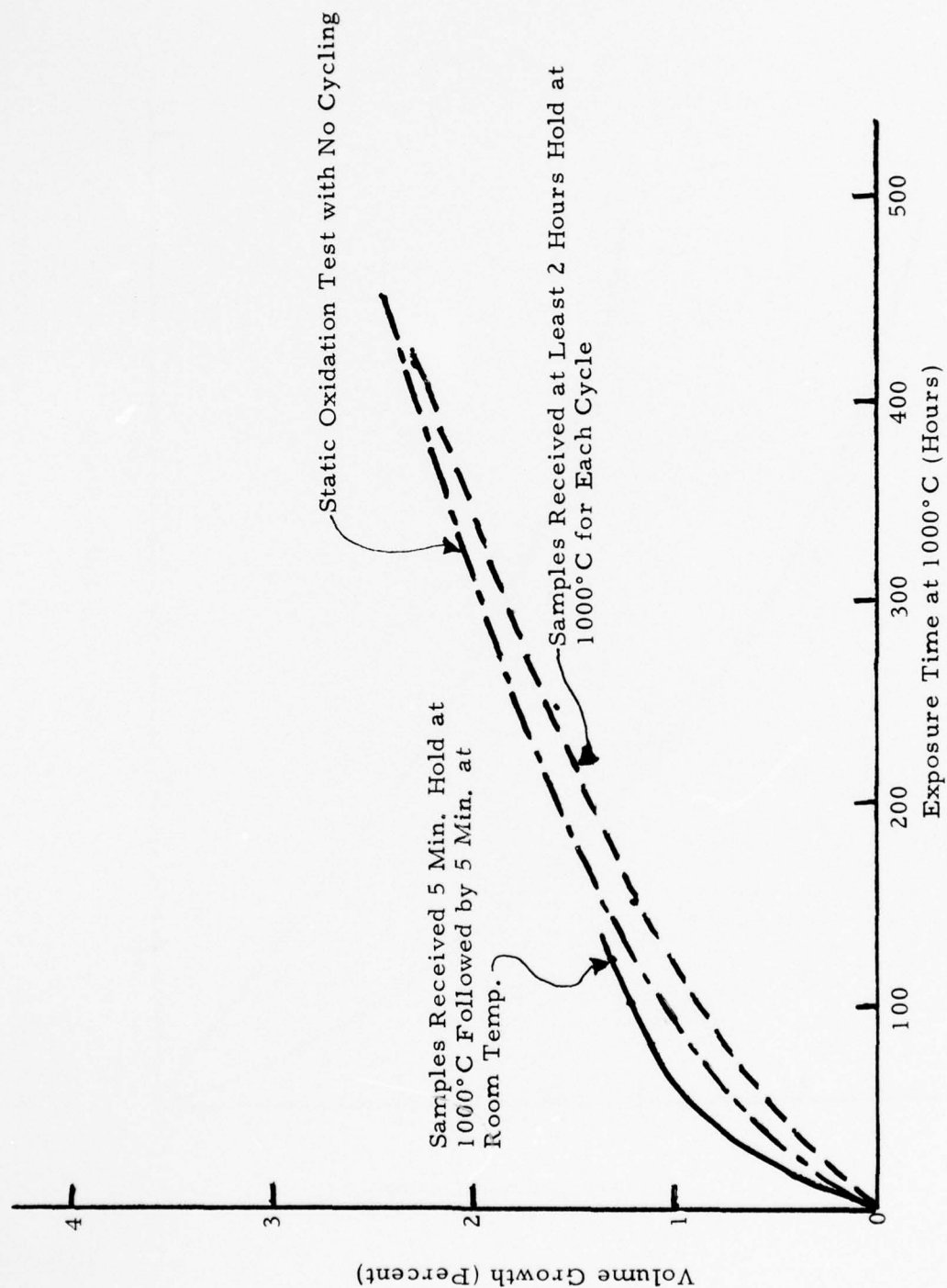


Figure 22: Cyclic Oxidation Behavior of Material A-2 NiCrAl

3. Dynamic Oxidation

Purpose - The dynamic oxidation test, one of the tests required by this contract, was used to determine if oxidation of the NiCrAl abrasable or flow control layers resulted in modification of the air flow through the structure during the useful life of the abrasable structure.

Procedure - The dynamic oxidation test rig was designed to meet the requirements specified by WPAFB. A schematic of the apparatus is shown in Figure 23, and the test rig itself is shown in Figures 24 and 25. The entire apparatus, excluding gauges and meters, with the sample attached was placed into a furnace. The furnace was used to heat the cooling air to the specified temperature by means of coiled tubing, which acted as a heat exchanger. A measured flow of the heated cooling air, at a constant pressure, was forced through the 1 in (2.54 cm) diameter test sample. This step resulted in some heating of the sample. Additional heat was supplied to the sample by means of the natural gas-oxygen torch to maintain the specified surface temperature.

The test rig was designed to simulate the nonequilibrium temperature conditions that a transpiration-cooled seal would encounter in an engine. The surface temperature was held at 1900°F (1040°C), and the cooling air temperature was 1200°F (650°C). The cooling air flow to achieve this gradient was substantially less than that required on the jet exhaust rig test due to the lower heat input of the natural gas-oxygen torch. The test was conducted for 500 hours.

The NiCrAl structure tested was a bilayer structure. A 2400 psi (16.5 MPa) abrasable layer (A2 material) was sintered to a 5000 psi (34.5 MPa) flow control layer (A1 material). This bilayer structure was brazed to a simulated support structure, shown in Figures 26 and 27, which was mounted on the test rig.

Operating temperatures were monitored from a test stand. Surface temperatures were measured by means of an optical and a radiation pyrometer. Temperatures at the flow control layer/support structure interface and at the back of the support structure were determined by means of Chromel-Alumel thermocouples. The cooling air temperature was also measured by a Chromel-Alumel thermocouple.

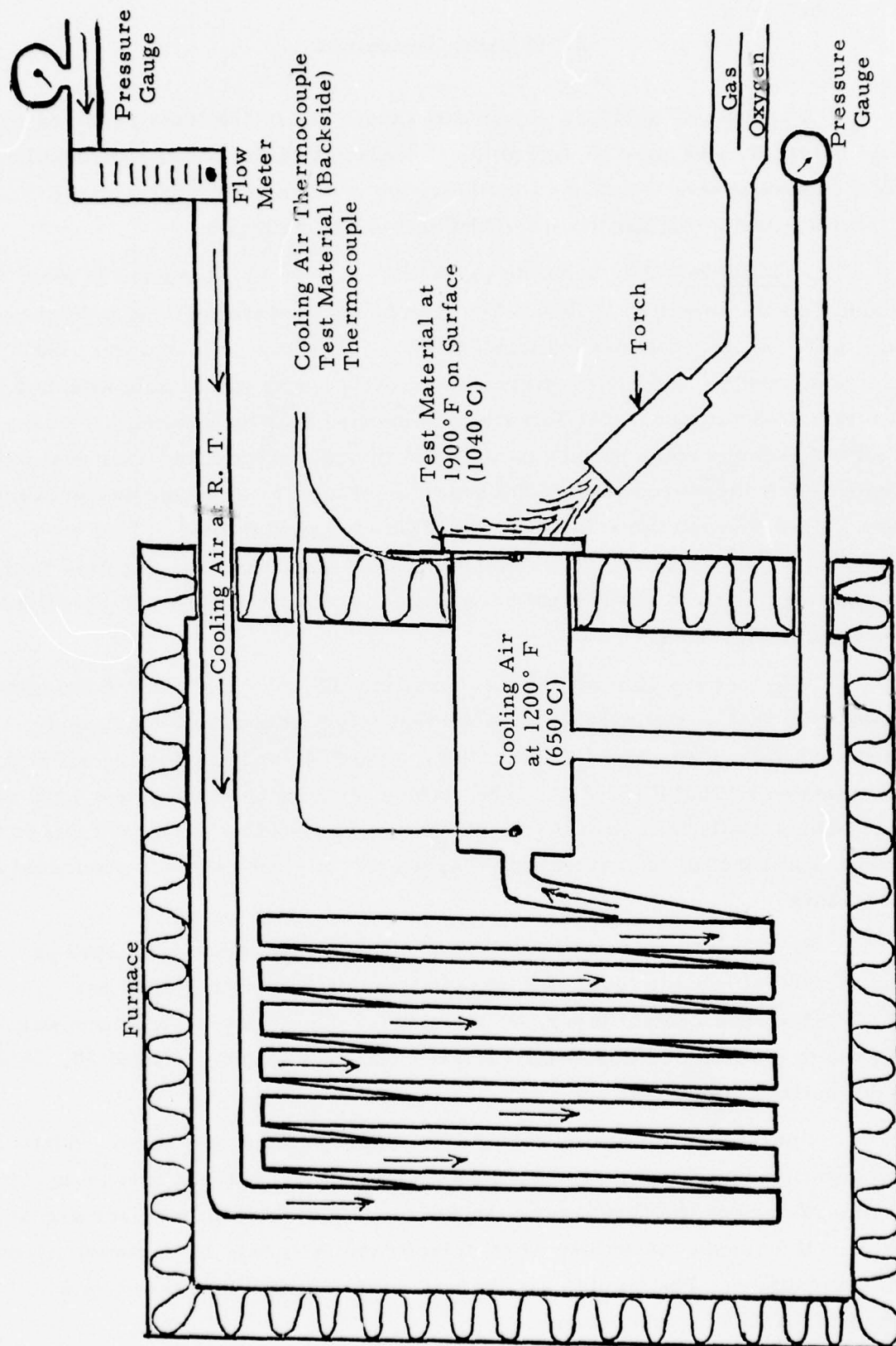


Figure 23: Dynamic Oxidation Test Rig



Figure 24: Entire Dynamic Oxidation Apparatus

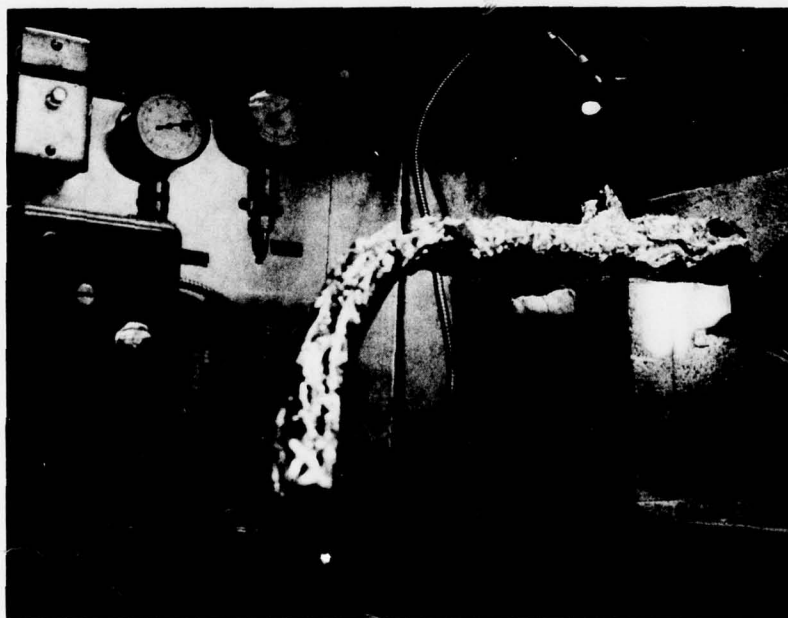


Figure 25: Dynamic Oxidation Apparatus

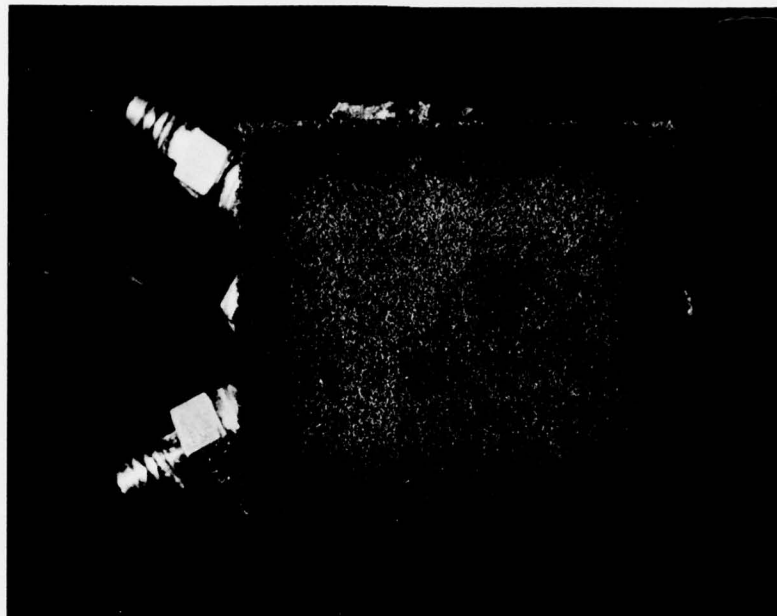


Figure 26: Dynamic Oxidation Test Segment Prior to Testing (Abradable Surface)

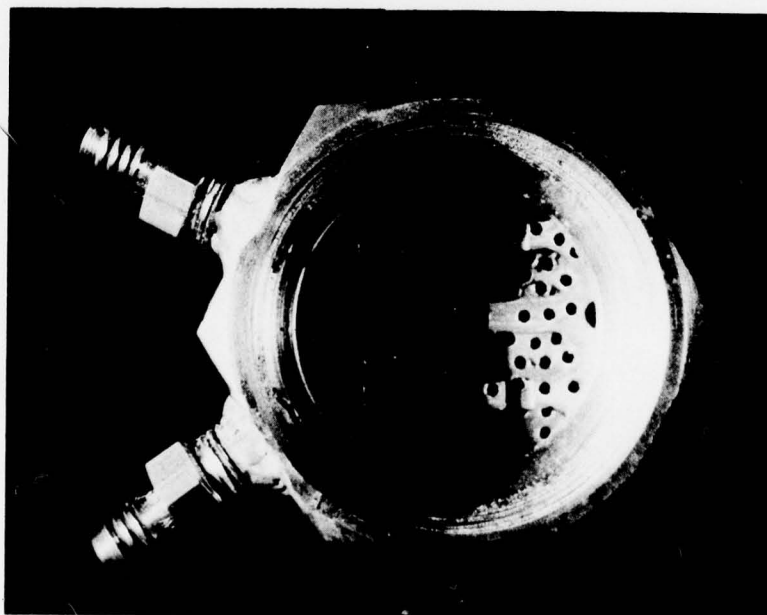


Figure 27: Dynamic Oxidation Test Segment Prior to Testing (Support Surface)

The cooling air flow rate was monitored at 1 psi (6.9 KPa) back pressure. The change in flow rate as a function of time and the change in pore size were measured. Microscopic examination of the structure was also done to determine the extent of the oxidation.

Discussion and Results - The dynamic oxidation test successfully showed that, after the establishment of a protective oxide coating, no further reduction in the pore size of the NiCrAl structure occurred during 500 hours of testing.

Figure 28 shows the change in the flow rate as a function of time when a 1 psi (6.9 KPa) back pressure is maintained. As can be seen, the curve levels off with no further reduction in the flow after the initial 150 hours at a minimum surface temperature of 1900°F (1040°C).

The initial pore size was 18 μm for the largest pore and 11 μm for the average pore as measured by the ASTM Bubble Test* method. These measurements were smaller than expected and were attributed to the braze wicking shown in Figure 29. The braze used was the AMS 4777 braze. No measurable change in pore size was observed after 500 hours of dynamic oxidation testing.

The conditions used in this test, although monitored and controlled, did vary; the surface temperature, especially, was nonuniform. The temperature was maintained at a minimum of 1900°F (1040°C) because of lack of flame uniformity. Four hot spots were observed on the sample (the locations are pointed out in Figures 31 through 35). These hot spots were continuously at a temperature of 1960°F (1070°C). Figure 36 shows a typical surface particle from one of these four locations. As can be seen, the particle is free of internal oxidation. (The phases present are γ and γ' . The γ' phase is represented by the light spots at the center of the particle.) The backside of the segment has a temperature of approximately 1550°F (843°C). This temperature varies with the surface temperature but a gradient of 350°F (195°C) always exists through the porous NiCrAl.

* The pore size was determined by ASTM method designated E128-61 (reapproved 1969). Figure 30 is a schematic of the apparatus used.

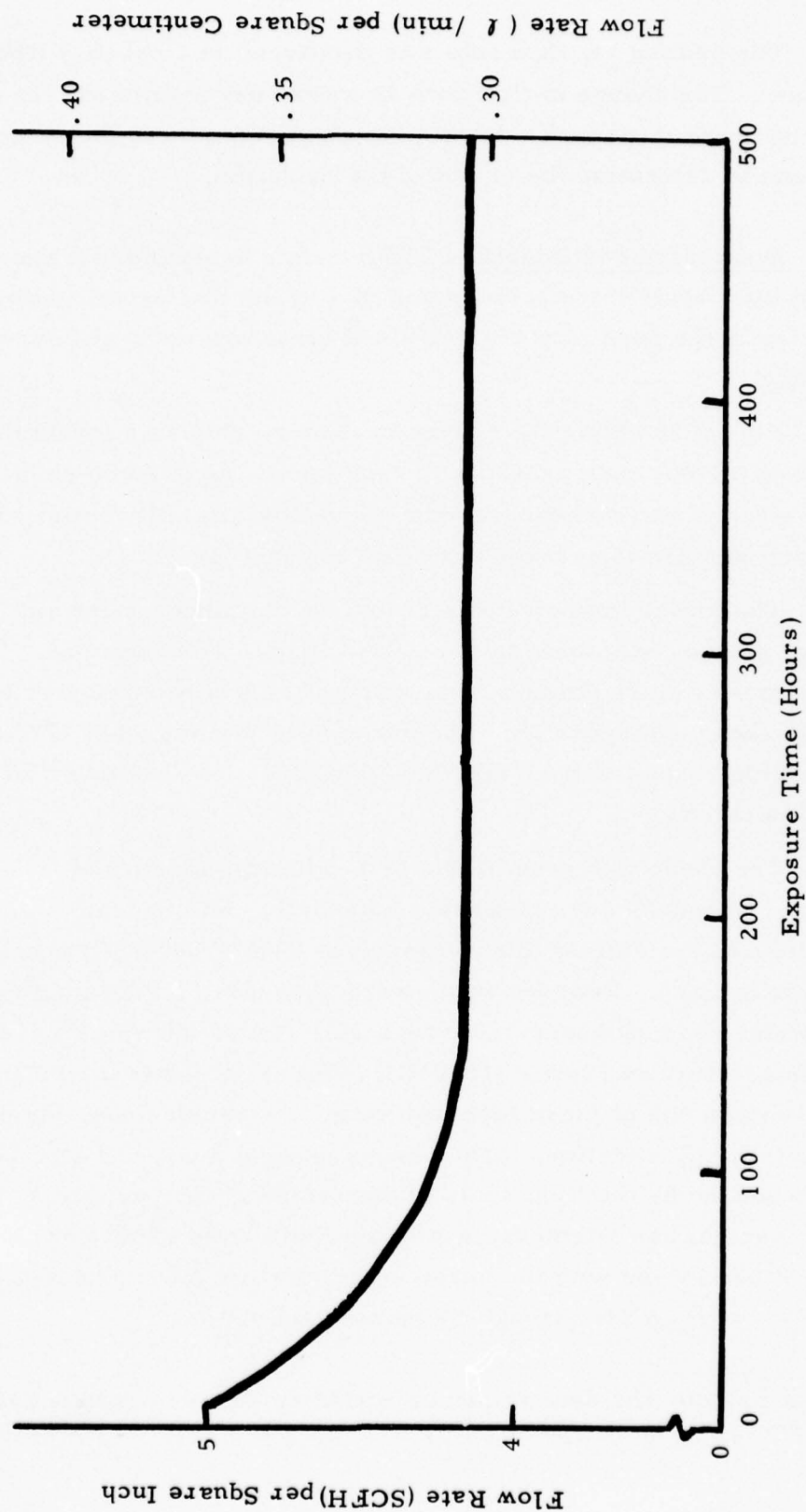


Figure 28: Flow Rate of 1200°F (871°C) Cooling Air Through Material A-2 NiCrAl as a Function of Oxidation Time at a Constant Pressure Drop of 1 psi (6.9 KPa)

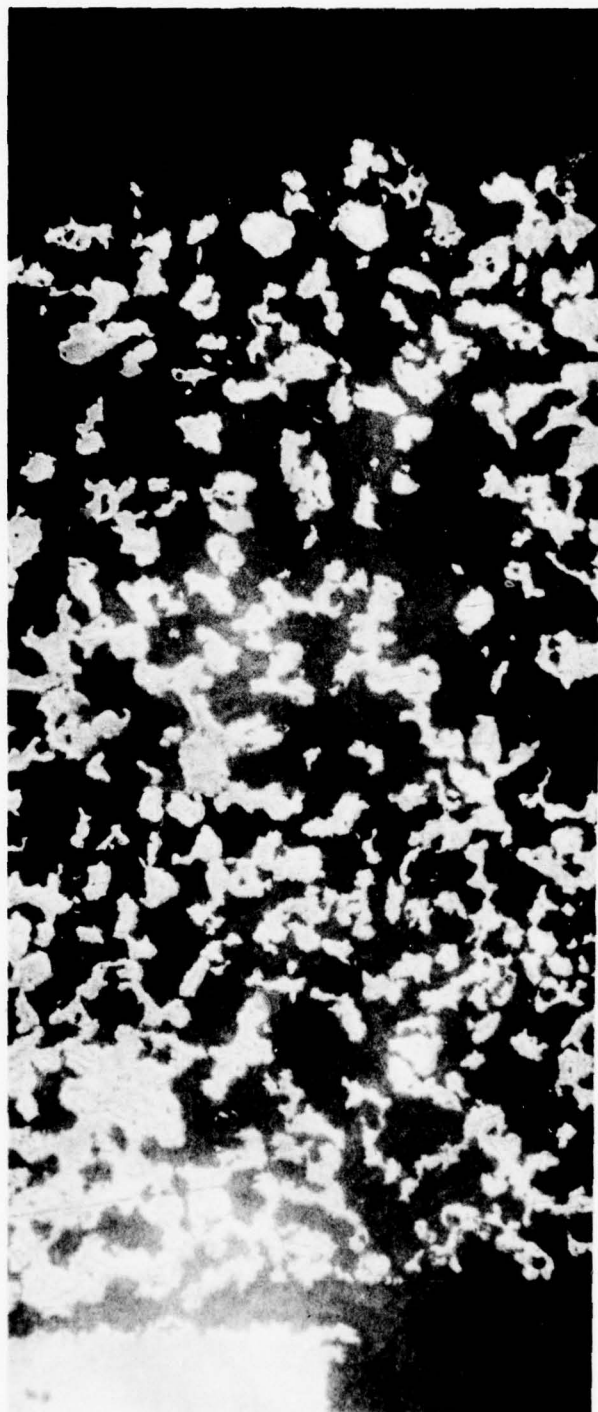


Figure 29: Micrograph of Dynamic Oxidation Test
Structure After 500 Hours of Exposure 100X

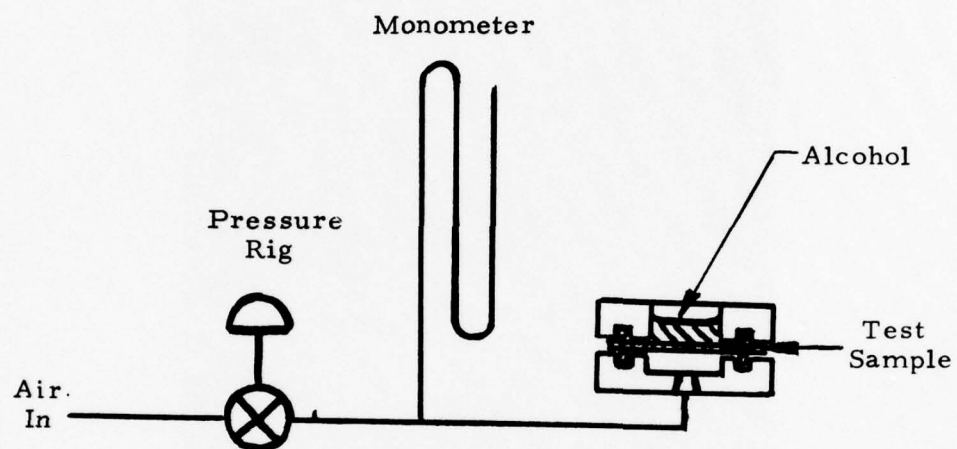


Figure 30: Schematic of Equipment Used to Measure the Pore Size of Porous Materials

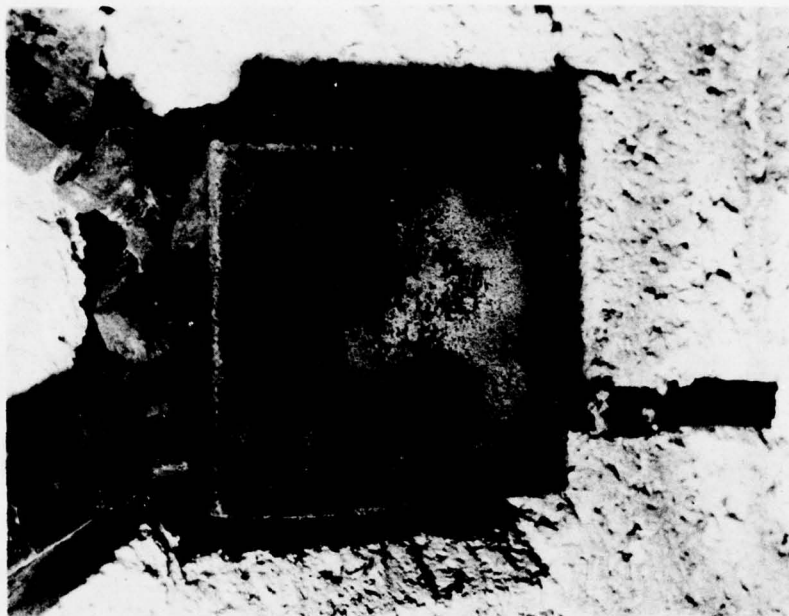


Figure 31: Dynamic Oxidation Test Segment After
75 Hours at 1900°F (1040°C)



Figure 32: Dynamic Oxidation Test Segment After
185 Hours at 1900°F (1040°C)

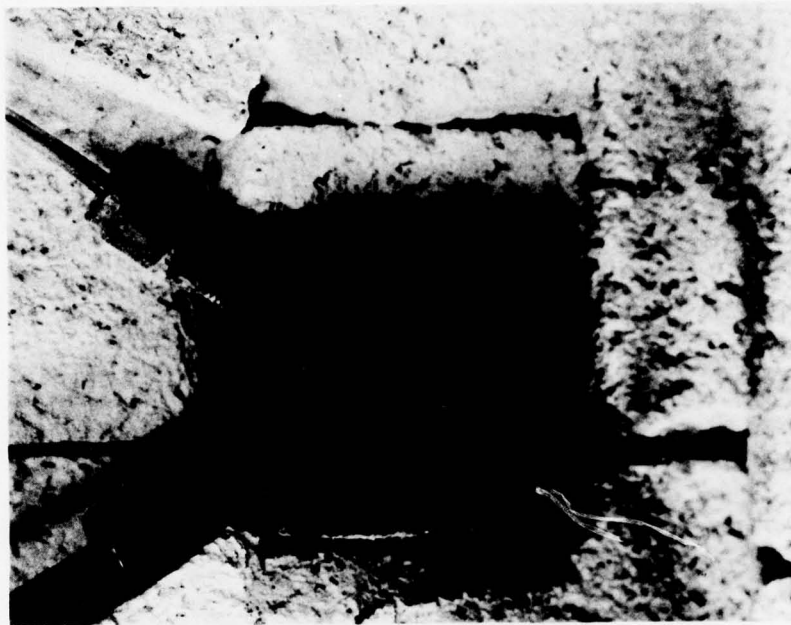


Figure 33: Dynamic Oxidation Test Segment After
286 Hours at 1900°F (1040°C)

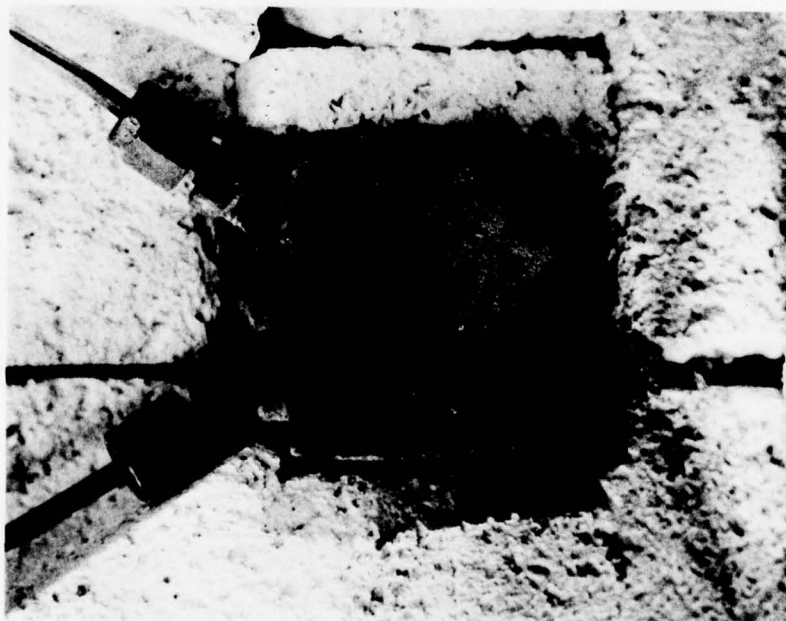


Figure 34: Dynamic Oxidation Test Segment After
430 Hours at 1900°F (1040°C)

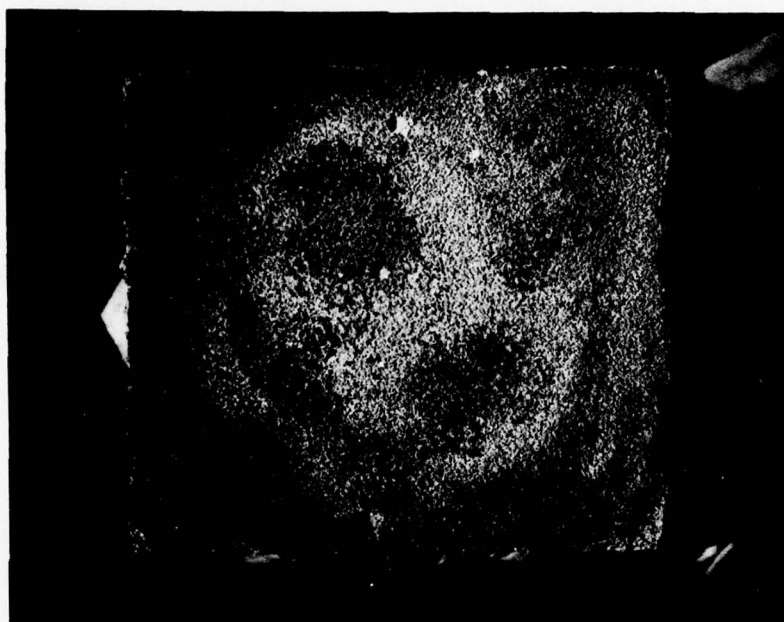


Figure 35: Dynamic Oxidation Test Segment After
500 Hours at 1900°F (1040°C)

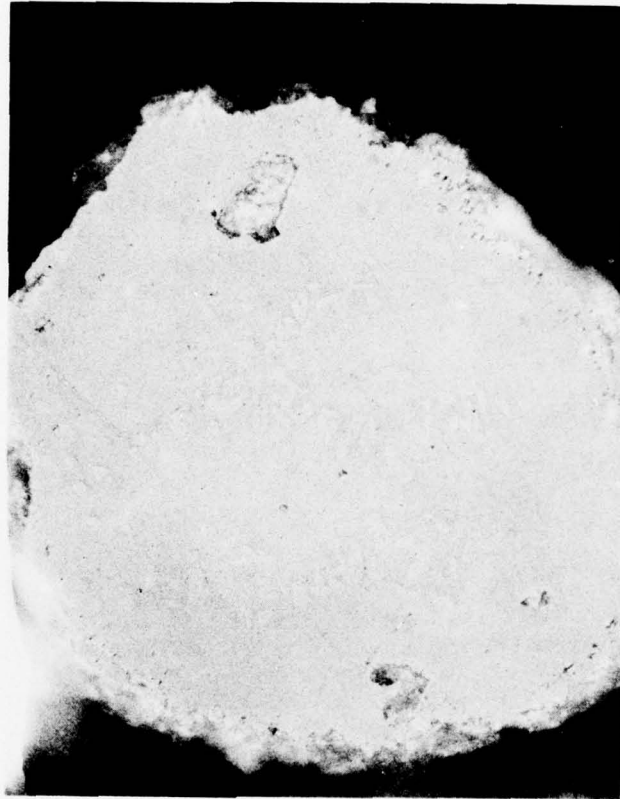


Figure 36: NiCrAl Particle Typical of One Located
on the Surface after 500 Hours of Dynamic
Oxidation Testing at 1900°F (1038°C) 500X

4. Particle Erosion

Purpose - The particle erosion test was done to determine the degree to which the rub-tolerant layer would erode when exposed to a stream of particles which are propelled by the high pressure gas stream.

Procedure - The particulate erosion test rig is shown schematically in Figure 37. Air at pressures up to 100 psi (690 KPa) was supplied by an 80 CFM (38 l/sec) reciprocating air compressor. The high pressure air was forced through an air line, and aspirated particles were injected into the air stream 8 in (20.3 cm) ahead of the 3/8 in (9.5 mm) ID nozzle. The test segments were placed 4 in (10.2 cm) from the nozzle and could be positioned at various angles with respect to the particle stream.

The room temperature test consisted of impinging No. 30 silicon carbide (SiC) shot onto the surface of several 2 in (5.1 cm) by 2 in (5.1 cm) segments of rub-tolerant material. The segments were placed at a 30° angle with respect to the 100 psi (690 KPa) air stream which accelerated the particles. The length of the test was approximately 5 hours at a particulate feed rate of 0.05 g/sec or until the material became completely eroded through.

Abradable material A2 at strength levels of 2100 psi (14.5 MPa) and 2400 psi (16.5 MPa) sintered to a 5000 psi (34.5 MPa) support layer (A1 material) were evaluated in this test. Bilayer materials were tested in both virgin and oxidized states. The oxidized segments were statically oxidized for 100 hours at 1900°F (1040°C). This oxidation caused a strength increase, as described in the "Static Oxidation" section. The UCAR Type AB-2 at 1050 psi (7.2 MPa) was used as a comparative material in the virgin state only*. Although the strength levels of Material A2 and UCAR Type AB-2 were quite different, they were the highest strength levels for each material at which the abrasible properties are still maintained.**

* Oxidation of UCAR Type AB-2 at 1900°F (1040°C) for 100 hours would have been destructive.

** The A2 material can maintain its abrasibility at a higher strength level than the UCAR Type AB-2 because the A1 addition to the NiCr in the former embrittles it at room temperature. The material, therefore, does not show plastic deformation, a condition which leads to smearing at strength levels between 1050 psi (7.2 MPa) and 2400 psi (16.5 MPa) for UCAR Type AB-2.

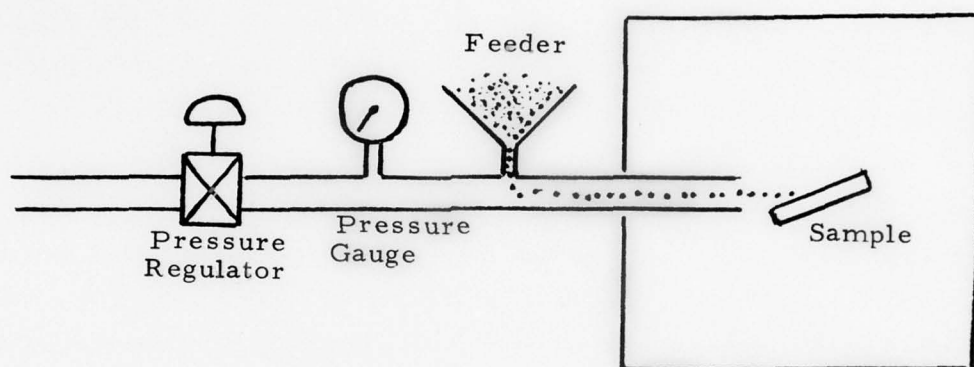


Figure 37: Particle Erosion Test Rig

Data were reported in graphic form as weight loss versus weight-of-particle-impinged and as thickness decrease versus weight-of-particles-impinged.

Discussion and Results - The results of preliminary short-term particle erosion testing indicated that erosion resistance increased with material strength. These tests indicate that an approximately linear relationship exists between the amount of erosion and the material strength over the strengths tested, as shown in Figure 38. The NiCrAl material tested was: 1650 psi (11.4 MPa) and 2150 psi (14.8 MPa) Material A-2 and 1800 psi (12.4 MPa) and 2600 psi (17.9 MPa) Material A-1. Test data from the final (5 hour) testing is also included in Figure 38. The preliminary test segments are shown in Figures 39, 40, 41, and 42.

The approximate linear relationship (erosion rate versus strength) is valid only when NiCrAl materials are used. For example, the comparative material, 1050 psi (7.2 MPa) UCAR Type AB-2, had better erosion resistance than the 2400 psi (16.5 MPa) A-2 material. The difference is believed to be largely due to the decrease in ductility caused by the Al addition to the NiCr.

The long-term particle erosion data, generated for 5 hours with a feed rate of approximately 50 mg/sec, are presented in graph form in Figures 43, 44, and 45. Figure 43, a graph of average decrease in thickness over the entire segment as a function of the amount of SiC used, and Figure 44, a graph of weight loss over the entire segment as a function of the amount of SiC used, indicated that higher strength levels would reduce the average rate of erosion. Although this effect can be seen when the two strength levels of the virgin materials are compared, it was demonstrated more dramatically when the virgin materials were compared with the higher-strength oxidized material.*

Along the major line of impingement, no difference can be detected in the erosion rates of the two strength levels of virgin A-2 material; however, a dramatic difference existed between the virgin segment and its higher-strength oxidized counterpart. This relationship is shown in Figure 45.

* The strength of material, when oxidized, increases as is shown in Figure 16.

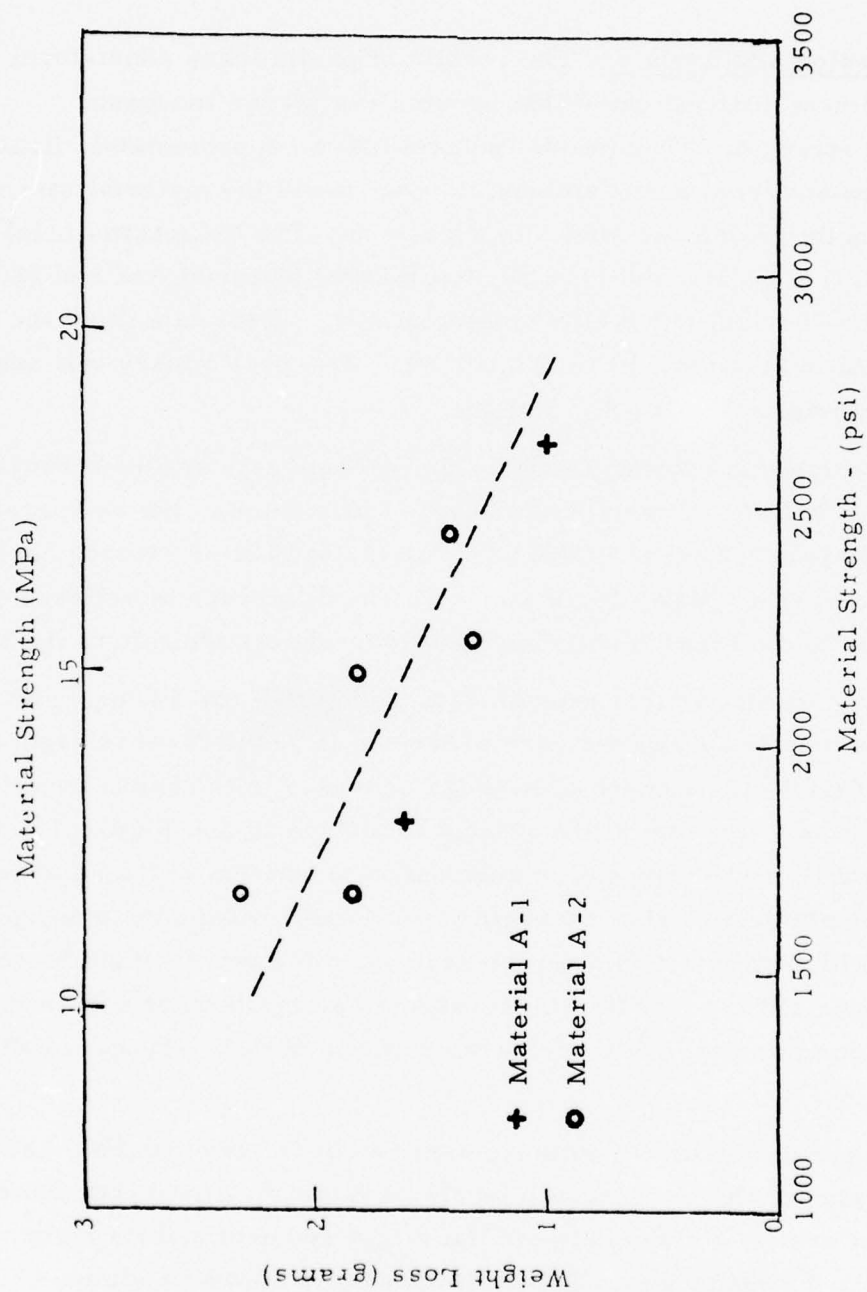


Figure 38: Room Temperature Erosion* Using No. 30 SiC With a 100 psi (690 KPa) Air Stream.

* 25 grams of SiC were shot at the structure at a rate of 0.05 g/sec.

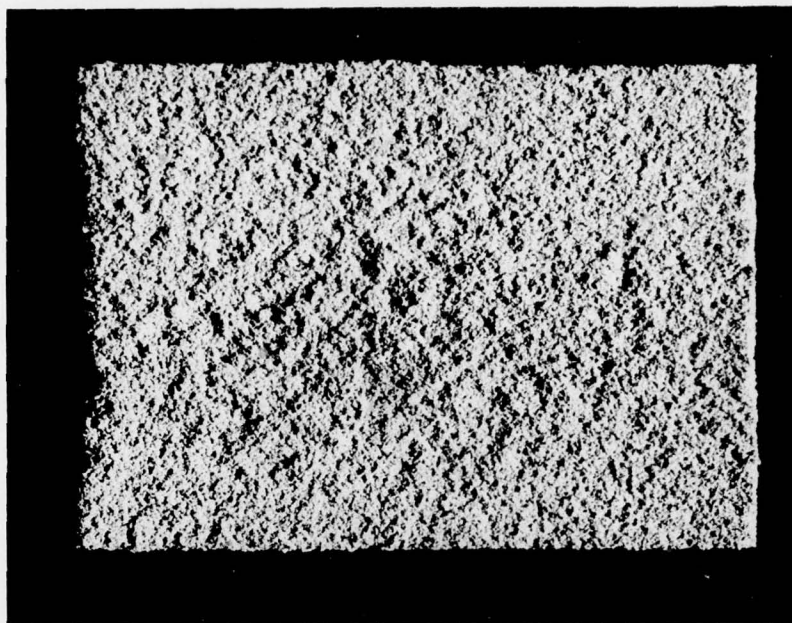


Figure 39: 1650 psi (11.4 MPa) Material A-2 NiCrAl After Being Impinged by 25 g of No. 30 SiC Shot

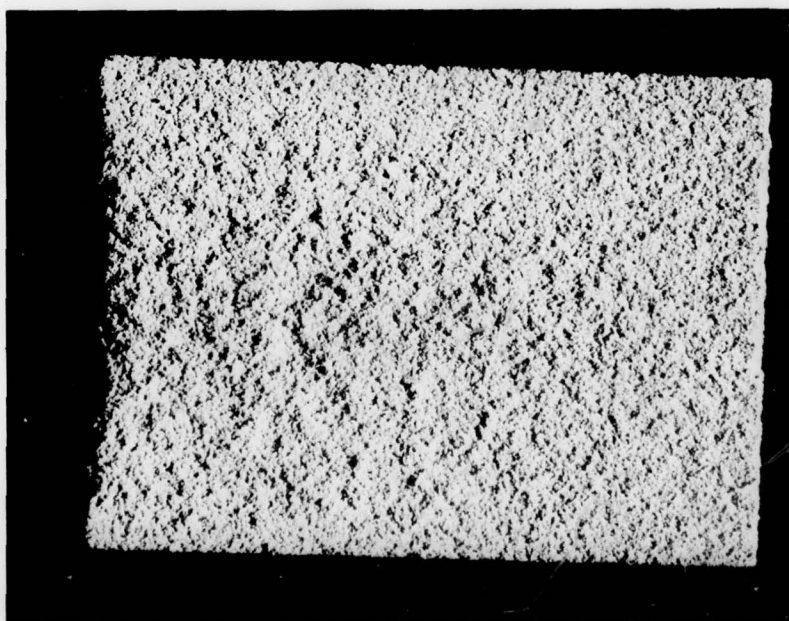


Figure 40: 1800 psi (12.4 MPa) Material A-1 NiCrAl After Being Impinged by 25 g of No. 30 SiC Shot

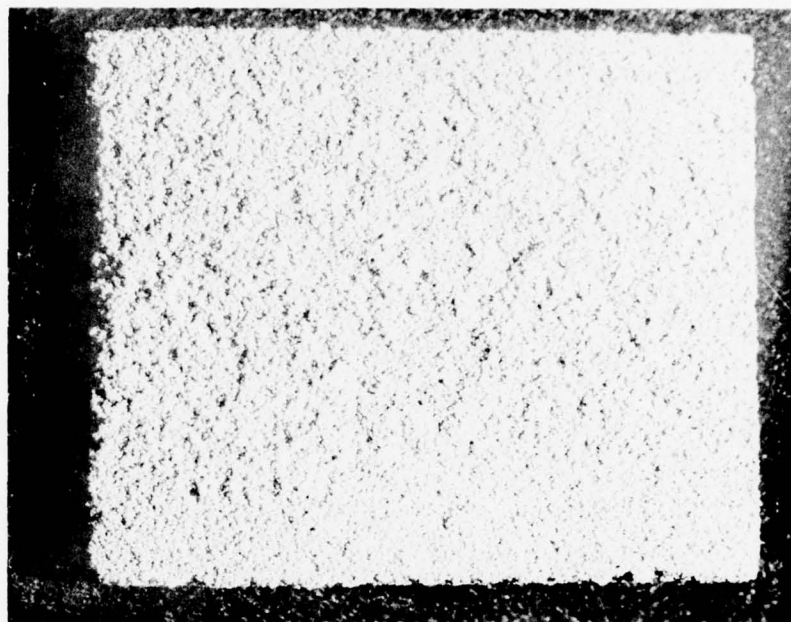


Figure 41: 2150 psi (14.8 MPa) Material A-2 NiCrAl After Being Impinged by 25 g of No. 30 SiC Shot

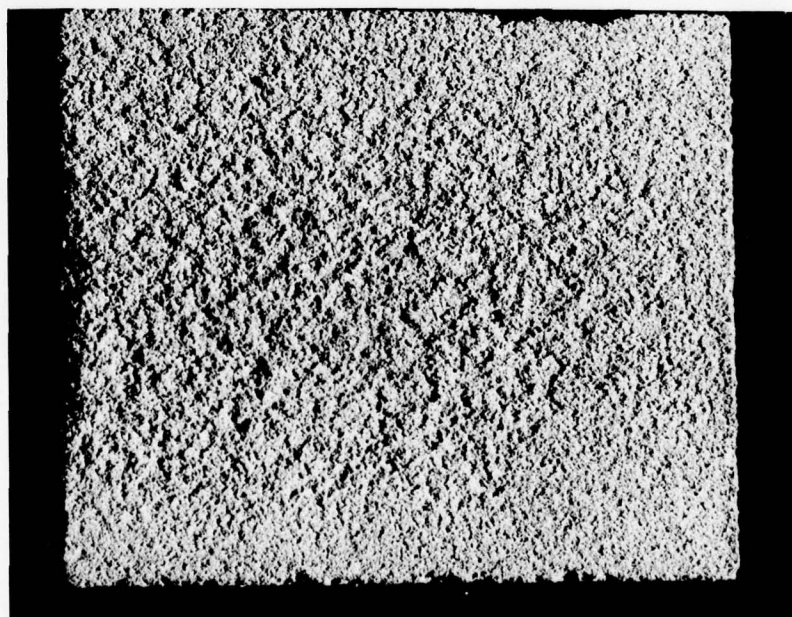


Figure 42: 2600 psi (17.9 MPa) Material A-1 NiCrAl After Being Impinged by 25 g of No. 30 SiC Shot

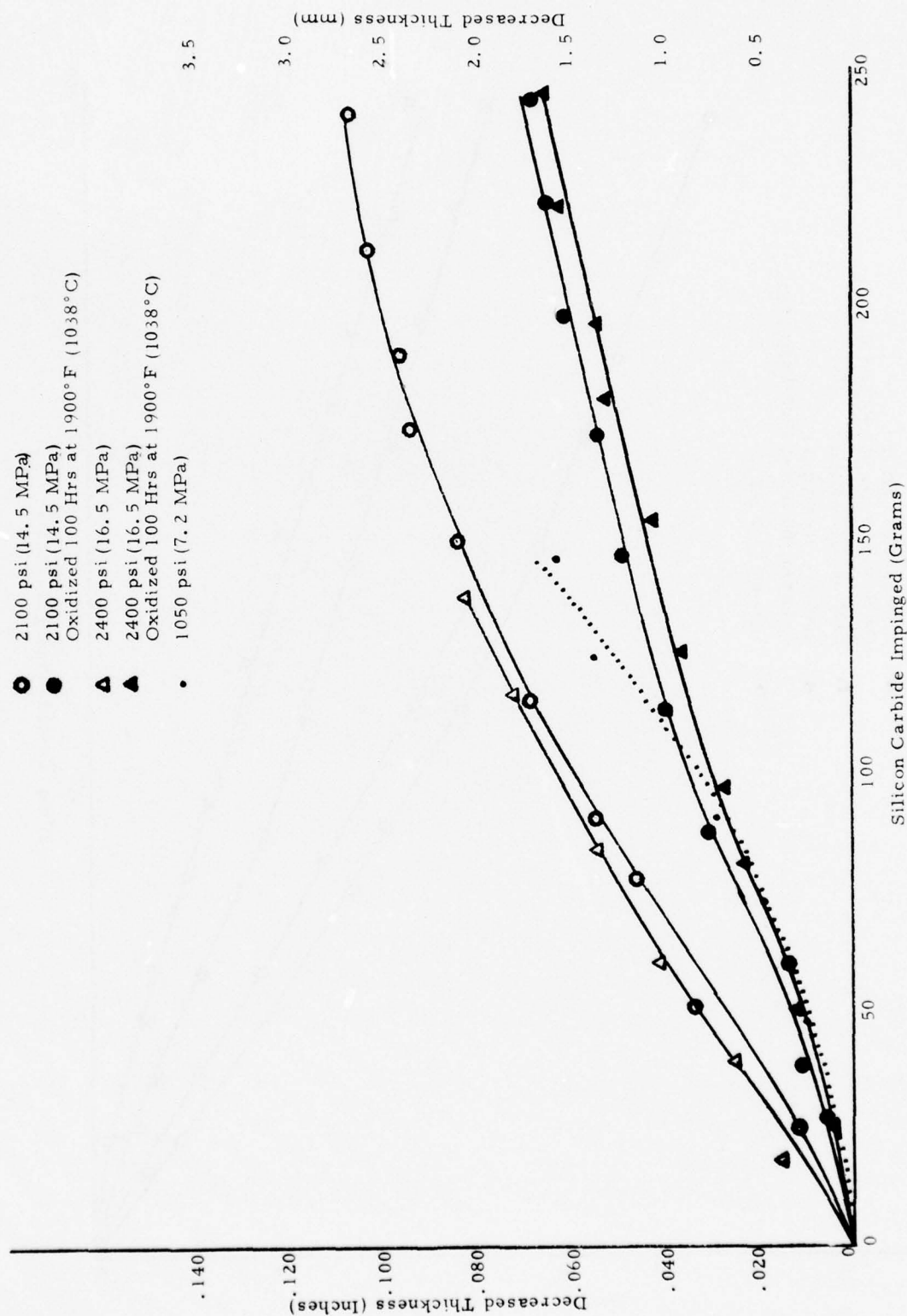


Figure 43: Average Decrease of Sample Thickness as a Function of the Quantity of SiC Impinged

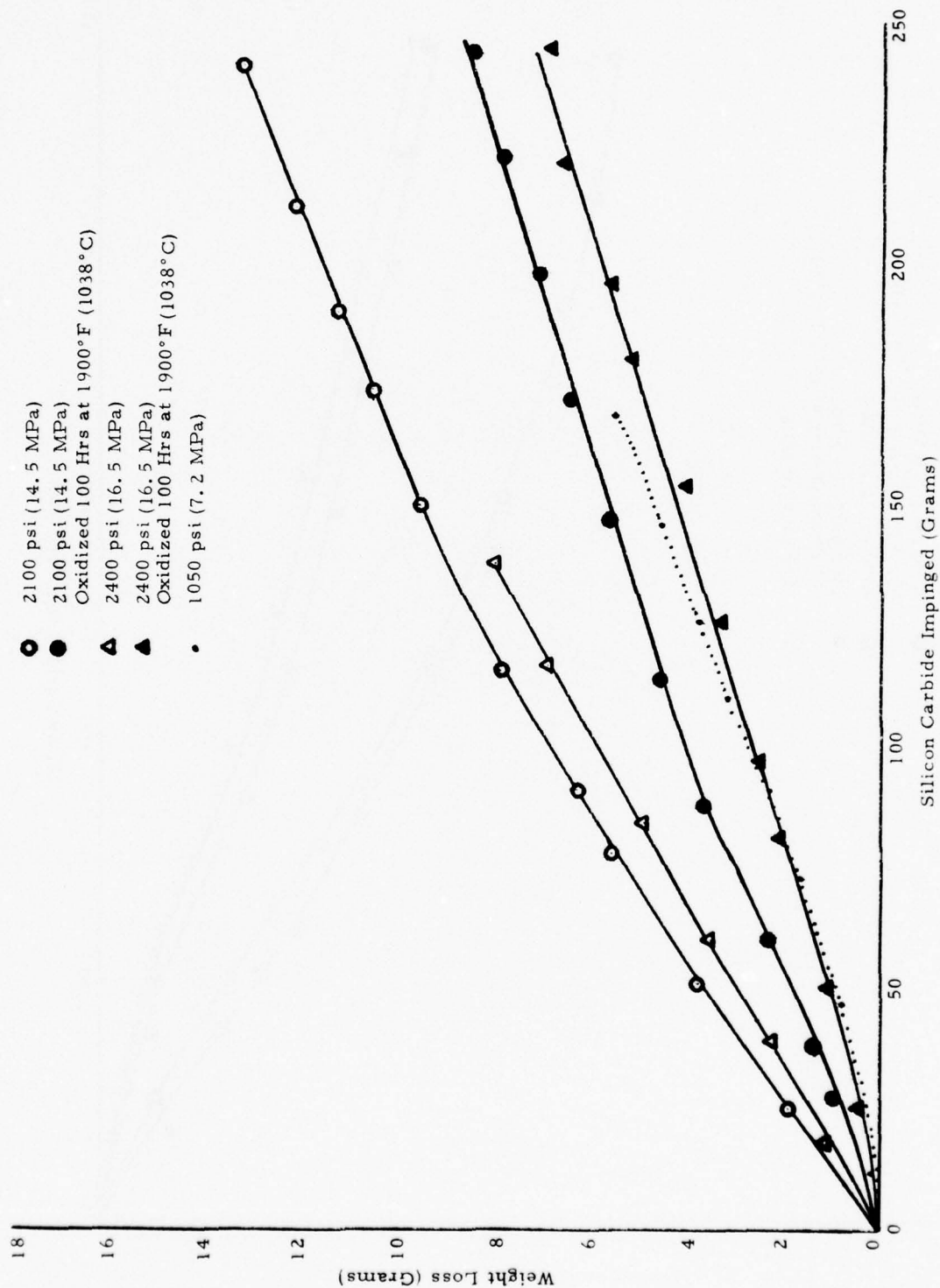


Figure 44: Weight Loss of the Sample as a Function of the Quantity of SiC Impinged

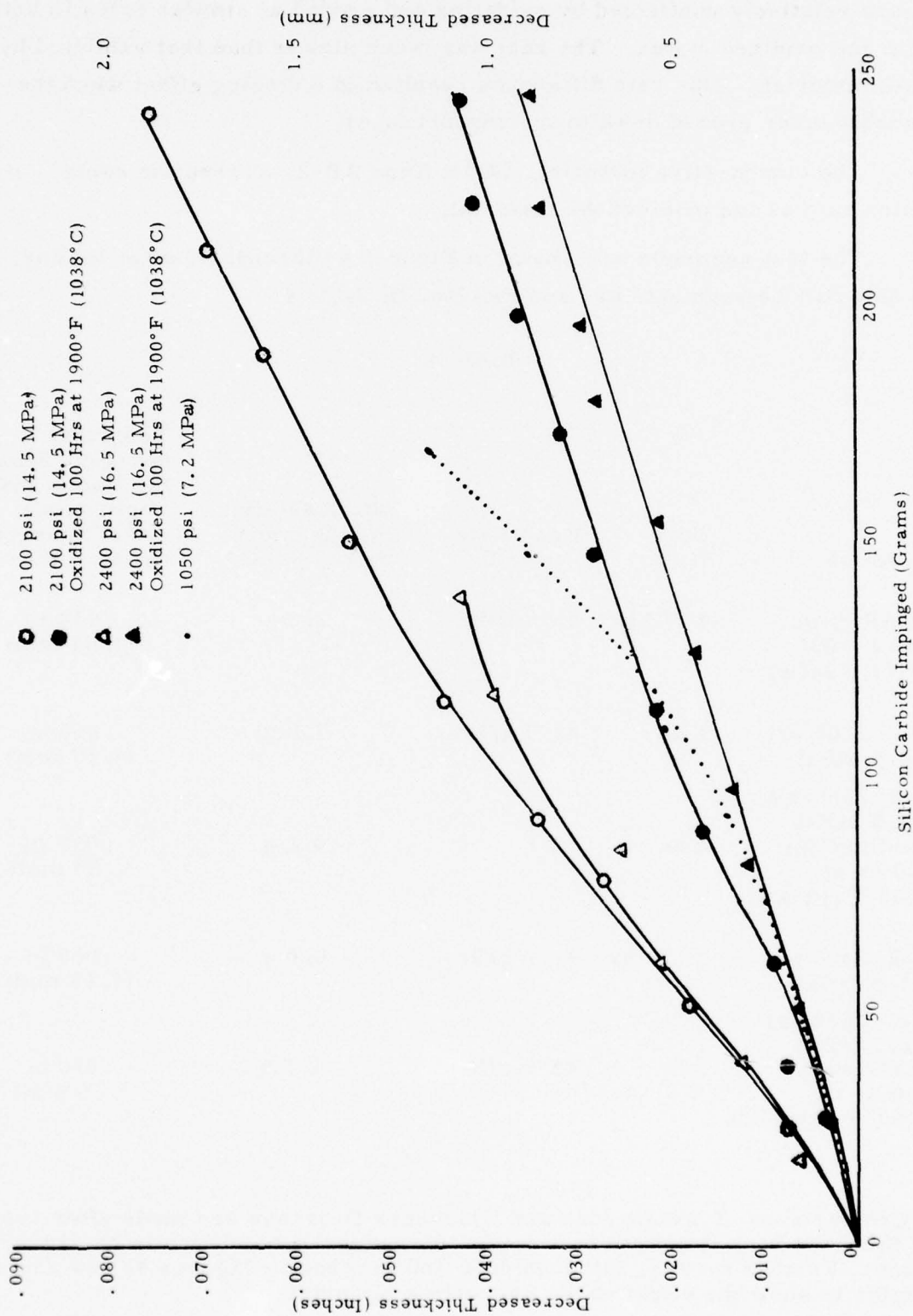


Figure 45: Decrease in Sample Thickness Along the Line of Major Impingement as a Function of the Quantity of SiC Impinged

The support layer (A-1), with an initial strength of 5000 psi (34.5 MPa), appears relatively unaffected by oxidation and eroded at similar rates in both virgin and oxidized states. The rate was much slower than that exhibited by the A-2 material. This rate difference resulted in a dishing effect when the abrasable layer eroded down to the support layer.

The comparative material, UCAR Type AB-2, showed the same erosion rate as the oxidized A-2 material.

The test segments are shown in Figures 46 through 50 after testing. The data for the segments are summarized in Table 4.

Table 4

Material	Test Time	Feed Rate of SiC	Wt. loss after impingement by 100 g SiC*	Thickness decrease along the line of major impingement after impinged by 100 g SiC*
UCAR Type AB-2 1050 psi (7.2 MPa)	4 1/2 hr	41.6 g/hr	2.5 g	.033 in (.84 mm)
A-2 2100 psi (14.5 MPa)	4 hr	41.7 g/hr	7.0 g	.060 in (1.52 mm)
A-2 2100 psi (14.5 MPa) Oxidized for 100 hr at 1900°F (1038°C)	5 hr	42.5 g/hr	4.2 g	.035 in (.89 mm)
A-2 2400 psi (16.5 MPa)	3 1/2 hr	41.1 g/hr	6.0 g	.065 in (1.65 mm)
A-2 2400 psi (16.5 MPa) Oxidized for 100 hr at 1900°F (1038°C)	5 hr	42.5 g/hr	2.5 g	.030 in (.76 mm)

* Comparisons of Weight loss and Thickness Decrease are made after 100 g of SiC have been impinged because at this point the A-2 layer is nearly worn away. Further testing, although done and graphed in Figures 43, 44 and 45, begins to show the effect of the supporting Material.

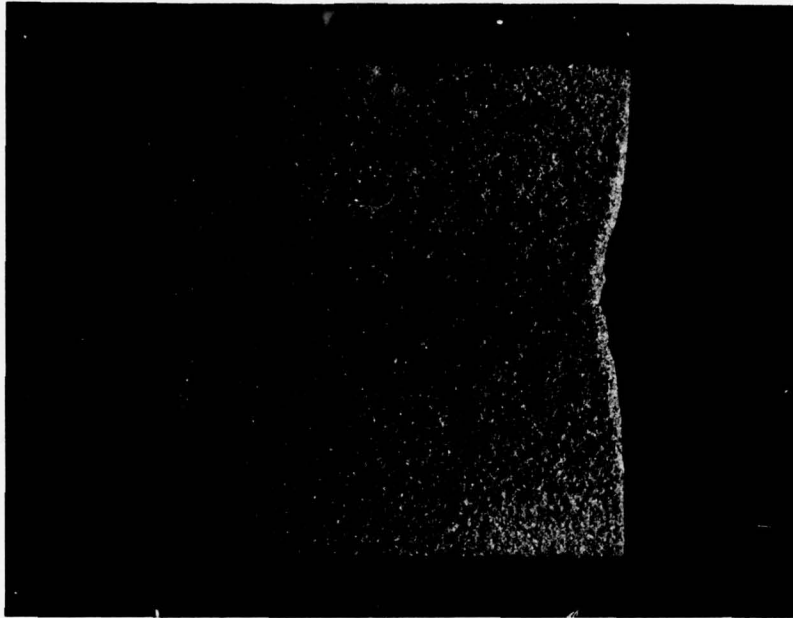


Figure 46: 1050 psi (7.2 MPa) UCAR Type AB-2
Material Subjected to 5 Hours of
Impingement by No. 30 SiC

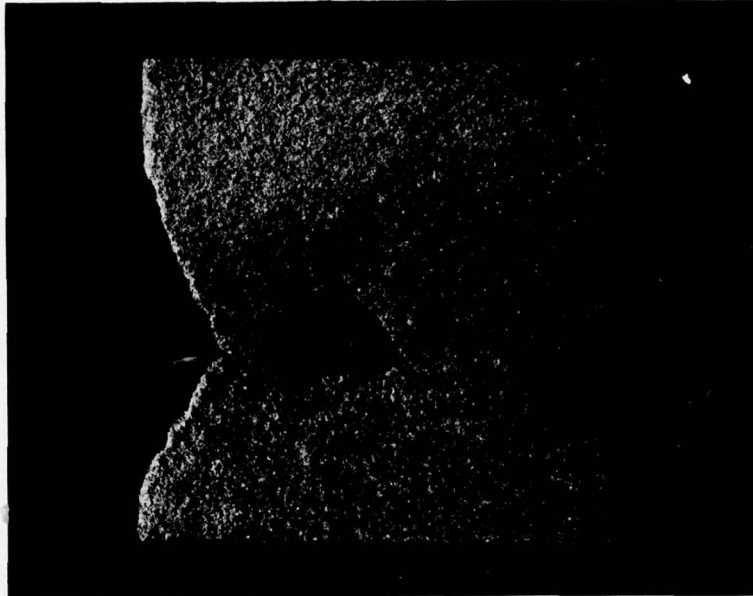


Figure 47: NiCrAl Bi-layer After Being Impinged by No. 30 SiC for 5 Hours (Abradable Layer is 2100 psi (14.5 MPa) Material A-2 and the Support Layer is 5000 psi (34.5 MPa) Material A-1)

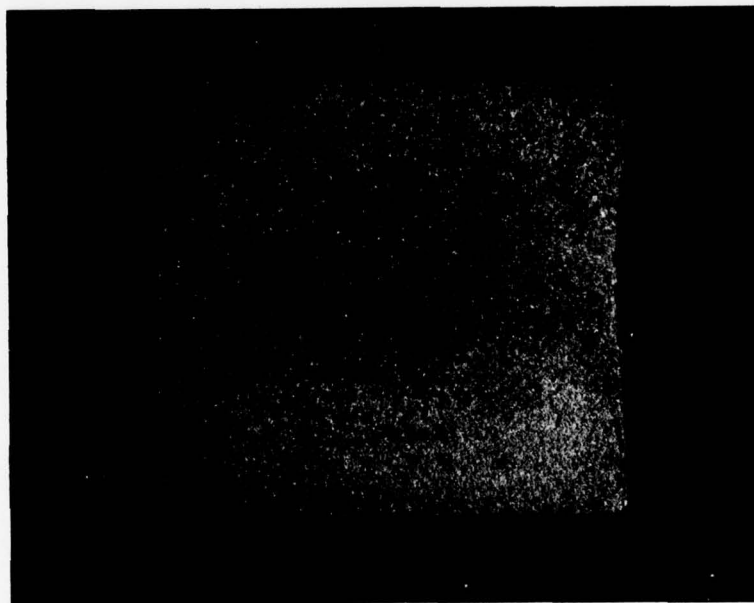


Figure 48: Oxidized NiCrAl Bi-layer After Being Impinged by No. 30 SiC for 5 Hours (Abradable Layer is 2100 psi (14.5 MPa) Material A-2 and the Support Layer is 5000 psi (34.5 MPa) Material A-1)

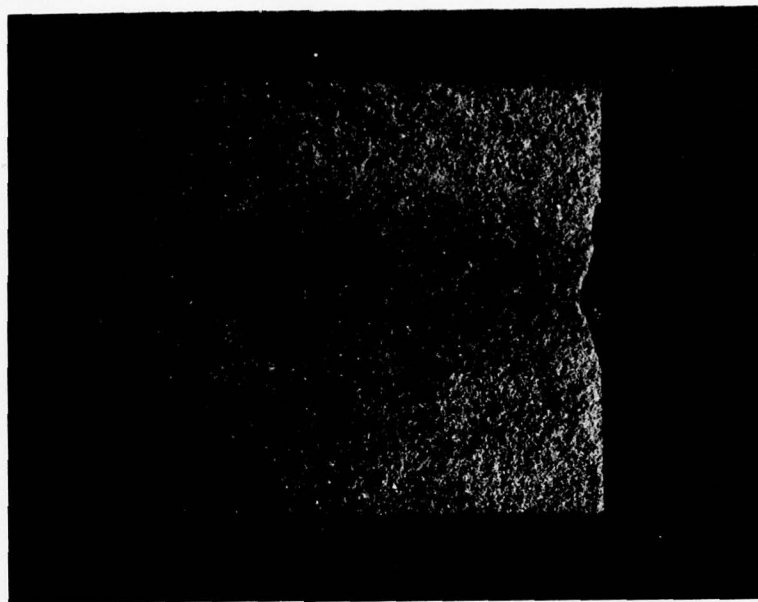


Figure 49: NiCrAl Bi-layer After Being Impinged by No. 30 SiC for 5 Hours (Abradable Layer is 2400 psi (16.5 MPa) Material A-2 and the Support Layer is 5000 psi (34.5 MPa) Material A-1)

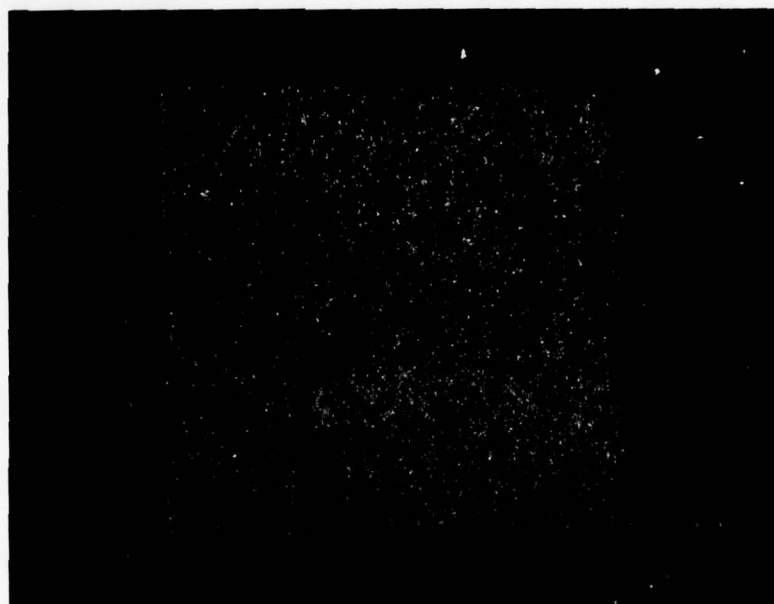


Figure 50: Oxidized NiCrAl Bi-layer After Being Impinged by No. 30 SiC for 5 Hours (Abradable Layer is 2400 psi (16.5 MPa) Material A-2 and the Support Layer is 5000 psi (34.5 MPa) Material A-1)

5. Abradability (In-House)

The A-1 and A-2 structures were subjected to preliminary testing for determination of the strength levels which should be submitted to NASA for final testing and evaluation. These were tested on the in-house abradability tester. The rig was set up to allow an Inconel 600 alloy blade rotating at 175 ft/sec (53 m/sec) to interact with the abradable material at a rate of 0.001 in/sec (25.4 μ /sec) for 0.030 in (762 μ m). In general, these types of visual cuts or rubs were produced by this test. The type of cut is dependent upon the ease with which a material is abraded.

Abradable - Visual appearance of the rub path looks like the unabraded areas.

Moderately Abradable - Visual appearance of the cut shows bright, shiny spots which are approximately the size of the particles used to make the material.

Unabradable - Visual appearance of the cut is smeared and discolored by oxidation of the smeared surface.

Typical rubs on the A-2 structure with strengths of 1650 psi (11.4 MPa) and 2100 psi (14.5 MPa) are shown in Figures 51 and 52, respectively. Rubs of the A-1 structure with strengths of 1800 psi (12.4 MPa) and 2400 psi (16.5 MPa) are shown in Figures 53 and 54. The rub on the 2100 psi (14.5 MPa) A-2 structure falls into the Abradable classification. Is superior to that of either the 1800 psi (12.4 MPa) (rated as Moderately Abradable) or the 2400 psi (16.5 MPa) (rated as Unabradable) A-1 structure. As a result, the A-2 structure has been chosen as the abradable material. Since the 2100 psi (14.5 MPa) A-2 material showed good abradability, it was one of the strength levels chosen. The 2400 psi (16.5 MPa) A-2 material was also chosen to determine whether A-2 materials with strengths higher than 2100 psi (14.5 MPa) are still abradable.*

* The higher the strength of material that still gives an acceptable rub, the better the particle erosion resistance.

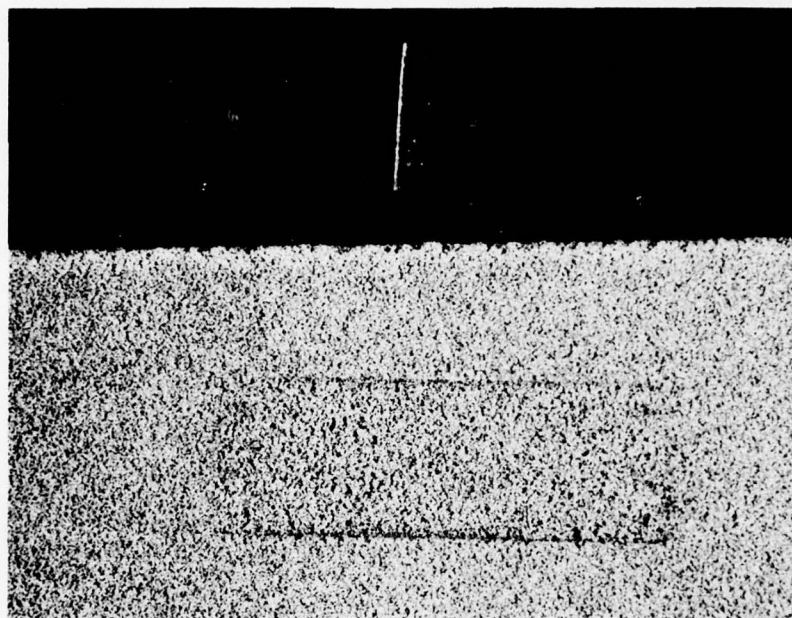


Figure 51: 1650 psi (11.4 MPa) Material A-2 NiCrAl After
a 0.030 in (762 μ m) Rub with an Inconel 600 Blade

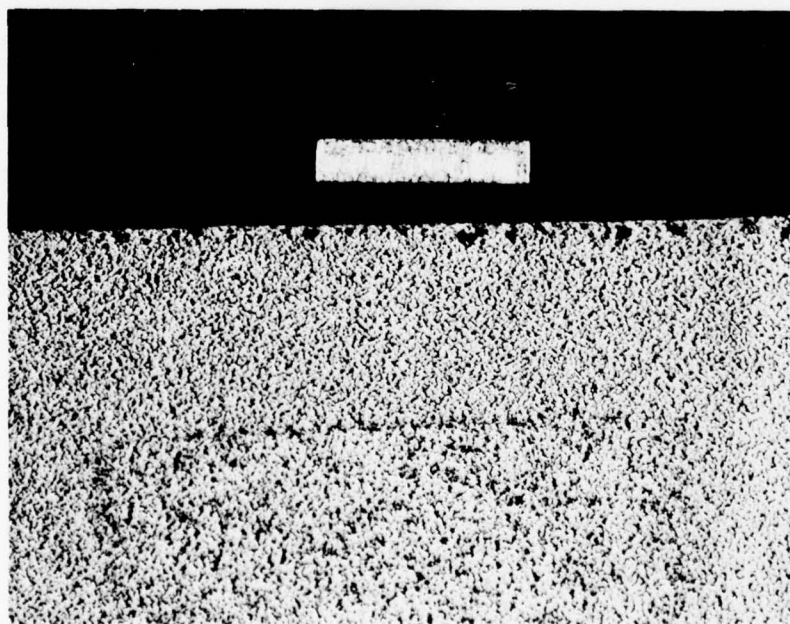


Figure 52: 2100 psi (14.5 MPa) Material A-2 NiCrAl After
a 0.030 in (762 μ m) Rub with an Inconel 600 Blade



Figure 53: 1800 psi (12.4 MPa) Material A-1 NiCrAl After
a 0.030 in (762 μ m) Rub with an Inconel 600 Blade



Figure 54: 2400 psi (16.5 MPa) Material A-1 NiCrAl After
a 0.030 in (762 μ m) Rub with an Inconel 600 Blade

6. Abradability (NASA)*

Purpose - The purpose of this study is to assess the rub tolerance of one type of gas path seal material considered suitable for high temperature applications which might be encountered in some turbine or advanced high pressure compressor applications. Sintered NiCrAl, prepared to two different strength levels, was subjected to rub interactions against simulated blade tips at two levels of rub speed and two incursion rates. Frictional and radial loads were measured, blade tip wear was estimated, and microscopic studies of the rub surfaces and rub debris were undertaken.

Procedure - The abradability test required was performed on equipment at NASA-Lewis. Rub evaluations were conducted on the apparatus shown in Figure 55. Twelve simulated blade tips were rotated at speeds up to 10,000 rpm in this investigation with associated rub velocities of up to 377 ft/sec (115 m/sec). Drive power was provided by a 3 hp induction motor coupled with a continuous speed variator which permitted control of the rub speed.

The gas path seal material sample was supported on a slideway feed mechanism so that it could be driven radially into the rotating blade tips. Radial incursion rates of 0.001 in/sec (25 μ m/sec) and 0.010 in/sec (250 μ m/sec) were employed.

During a rub interaction, the rotating speed was held constant, radial loads and frictional torque were continuously recorded, and the blade tip temperature was monitored and recorded by means of an infrared pyrometer. The signal from the pyrometer provided an indication of the number of blade tips simultaneously participating in the rub interaction as well as the actual tip temperature.

Wear debris generated during the rub interaction was collected on the fixture indicated in Figure 55. Debris particles impinged on a strip of sticky tape, thus being captured for subsequent examination.

Rub interaction depths were monitored during a test by means of a dial gauge indicator which showed the relative radial motion of the feed slideway carriage with respect to the rotating disk. Interaction depths could be controlled to within 0.001 in (25 μ m) of the desired depth.

* Data prepared and summarized by R. Bill of NASA, Lewis Research Center.



Figure 55: Abradable Seal Test Apparatus

Prior to testing, the blade tips were ground so that the tip surface was parallel (to the degree possible) to the supporting root. The tip surface finish was approximately 20 RMS ($0.5\text{ }\mu\text{m}$) after conditioning. The tips were then cleaned with ethanol, and the height of each simulated blade tip was measured. Heights were maintained to within $\pm 0.0002\text{ in}$ ($4\text{ }\mu\text{m}$).

Selected gas path seal material samples were epoxy bonded to a mild steel backing which was screwed to a combination specimen support/cantilever load cell. The blade tips were brought to the desired rotating speed, the selected incursion rate was set, and the rub interaction was initiated. In these tests the interaction was continued to a 0.03 in ($750\text{ }\mu\text{m}$) depth.

Rotational speeds of 187 ft/sec (57 m/sec) and 377 ft/sec (115 m/sec) were selected for this study. Under 187 ft/sec (57 m/sec) conditions, tests were conducted at incursion rates of 0.001 in/sec ($25\text{ }\mu\text{m/sec}$) and 0.010 in/sec ($250\text{ }\mu\text{m/sec}$); under 377 ft/sec (115 m/sec) conditions, only the 0.001 in/sec ($25\text{ }\mu\text{m/sec}$) incursion rate was employed.

Post-test evaluation included blade tip and abradable material rub-surface microscopic examination, and wear-debris examination. A measure of the wear (or transfer) to the blade tips was obtained by observing specimen focus position changes over the tip surface.

The blade tip specimens used in this investigation were made of AM 355 steel, the nominal composition of which is Fe - 15.5% Cr - 4.5% Ni - 3% Mo machined from AMS 5594 stock.

Two variations of sintered NiCrAl seal material were evaluated. Both variations were approximately 40% dense with a particle size of approximately $0.006\text{ to }0.008\text{ in}$ ($150\text{ to }200\text{ }\mu\text{m}$) and a typical pore size of $0.008\text{ to }0.012\text{ in}$ ($200\text{ to }300\text{ }\mu\text{m}$). One variation, to be designated "Material A2-2100," was sintered to an approximate tensile strength of 2100 psi (14.5 MPa); the other variation, to be designated "Material A2-2400," was sintered to an approximate tensile strength of 2400 psi (16.5 MPa). These two sintered NiCrAl materials are considered to be candidates for high temperature gas path seal applications (temperatures up to 1800°F - 1900°F (980°C - 1040°C), such as might be found in some turbine or advanced compressor locations.

Results and Discussion - The results of the friction and radial load studies performed on materials A2-2100 and A2-2400 are presented in Figure 56 along with results for current "state-of-the-art" gas path seal material. The state-of-the-art materials are comparatively low temperature types, intended for compressor seal applications. A few general observations pertaining to these results may be made. Friction forces measured for the A2-2100 and A2-2400 series materials at a 377 ft/sec (115 m/sec) rub speed were significantly lower than those measured at 187 ft/sec (57 m/sec), probably indicating thermal softening effect. Corresponding "friction coefficients" (friction was very unsteady) were less than 0.1 at the high speed and between 0.15 and 0.2 at the low speed. Surprisingly, increasing the incursion rate from 0.001 in/sec (25 μ m/sec) had only a minimal effect on measured frictional and radial loads. However, under high incursion rate conditions, contact was much more continuous than under low incursion rate conditions. During a given revolution of the disk, pyrometer data revealed that virtually all of the blade tips had undergone heavy interaction when the incursion rate was 0.010 in/sec (250 μ m/sec). At 0.001 in/sec (25 μ m/sec) incursion rate, 2 or 3 blade tips usually came into heavy contact during a typical revolution of the disk. With the exception of the high incursion rate test, frictional and radial loads for the A2-2400 material were approximately 25% higher than those for the A2-2100 series.

Frictional forces and radial loads for the state-of-the-art materials were usually 1/4 to 1/3 as high as for the A2-2100 and A2-2400 series materials. Friction coefficients of approximately 0.15 were measured.

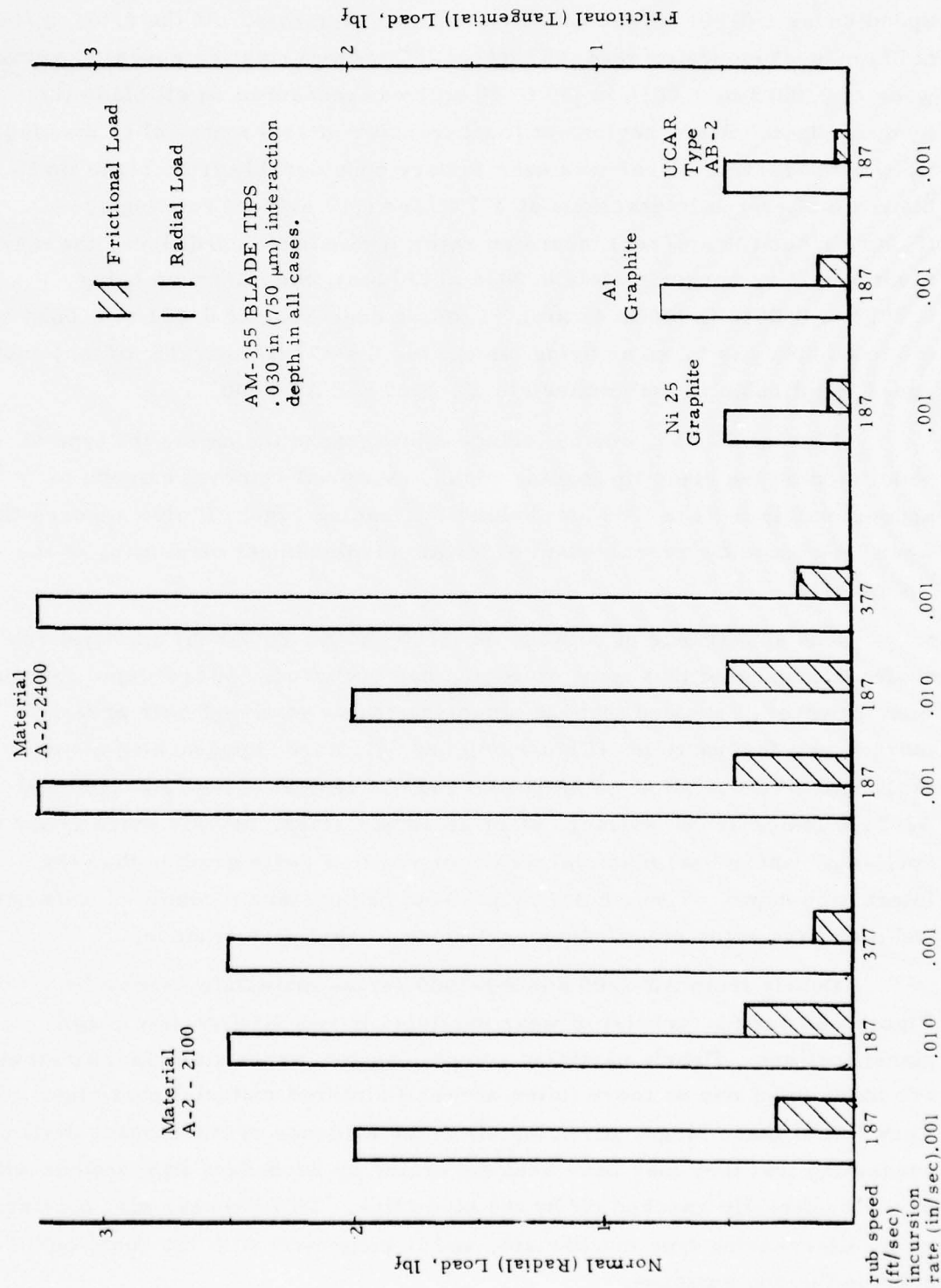


Figure 56: Frictional and Radial Load Results for Sintered NiCrAl Seal Materials Subjected to a Rub

Wear measurements, summarized in Table 5, indicated less than 0.0004 in (10 μm) of wear to the blade tip leading edges after rub interaction with A2-2100 and A2-2400 materials at 187 ft/sec (57 m/sec) rotating speed under a 0.001 in/sec (25 $\mu\text{m}/\text{sec}$) incursion rate. At the 0.010 in/sec (250 $\mu\text{m}/\text{sec}$) incursion rate (187 ft/sec (57 m/sec) rotating speed), however, wear of 0.0012 to 0.0016 in (30 to 40 μm) was measured on all blade tip leading edges. Also, regions of local transfer of seal material to the blade tip were observed. Wear was seen to vary considerably from blade tip to blade tip after rub interactions at 377 ft/sec (115 m/sec) rotating speed (0.001 in/sec (25 $\mu\text{m}/\text{sec}$) incursion rate); under these conditions, the maximum wear was approximately 0.0028 in (70 μm), the minimum being 0.0012 to 0.0016 in (30 to 40 μm). Leading edge wear of 0.002 to 0.0024 in (50 to 60 μm) was taken as being typical for the 377 ft/sec (115 m/sec) rub speed, applicable to both materials A2-2100 and A2-2400.

Figures 57, 58, and 59 include micrographs indicating the type of wear seen on the blade tip leading edges. Material removal extends to approximately 0.03 in (750 μm) behind the leading edge. It also appears that wear took place by a mechanism of plastic displacement or plowing of the tip material.

The appearance of both the A2-2100 and A2-2400 seal material rub surfaces suggested that some smearing had occurred. Microscopic examination, however, revealed that the smearing rarely extended over areas of more than a few particles (Figures 60 and 61), never approaching a continuously smeared condition. Figures 60 and 61, typical of both A2-2100 and A2-2400 material rub surfaces after all interactions, reveals some areas of "pull-out" where seal material was removed to a depth greater than the interaction depth. These holes or pull-out regions are a couple of mils deep and may have some significance pertaining to seal performance.

Debris from A2-2100 and A2-2400 series materials, shown in Figures 62 and 63, consist of wear particles in two distinct size range classifications. Debris particles comprising the larger size classification are made up of one or more (often several) sintered material particles. Very few of these larger particles show any evidence of rub surface distress, suggesting that they may have been generated by secondary interactions with particles directly knocked off by the blade tips. This process may be visualized as a self-scouring type mechanism, and is consistent with the "pull-out" holes seen on the rub surfaces.

Table 5

Material	A-2 - 2100			A-2 - 2400			Ni 25 Graphite	Al Graphite	UCAR Type AB-2
	187	187	377	187	187	377			
Rub Speed ft./sec (m/sec)	187 (57)	187 (57)	377 (115)	187 (57)	187 (57)	377 (115)	187 (57)	187 (57)	187 (57)
Incursion Rate in/sec (μ m/sec)	.001 (25)	.010 (250)	.001 (25)	.001 (25)	.010 (250)	.001 (25)	.001 (25)	.001 (25)	.001 (25)
Blade Wear inches (μ m)	0- .0004 (0-10)	.0012- .0016 (30-40)	.0016- .0024 (40-60)	0- .0004 (0-10)	.0012- .0016 (30-40)	.002- .0024 (50-60)	-	-	-
Material Transfer inches (μ m)	-	.0004- .0008 (10-20)	-	-	.0008- .0012 (20-30)	-	-	-	.002 (50)

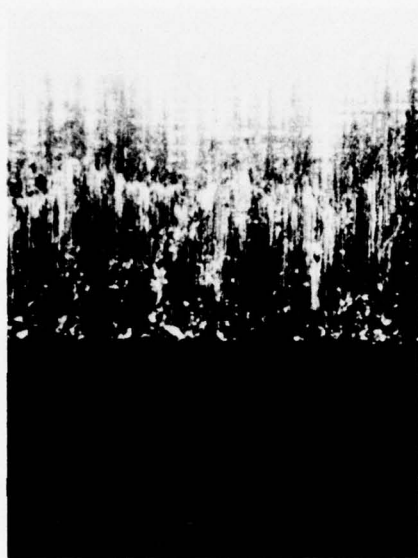


Figure 57: Micrograph of the Leading Edge of an AM 355 Blade Tip After Interaction with Material A-2 NiCrAl. Blade was rotating at 377 ft/sec (115 m/sec) and had an incursion rate of 0.001 in/sec (25 μ m/sec). 35X



Figure 58: Micrograph of the Leading Edge of an AM 355 Blade Tip After Interaction with Material A-2 NiCrAl. Blade was rotating at 377 ft/sec (115 m/sec) and had an incursion rate of 0.001 in/sec (25 μ m/sec). 127X

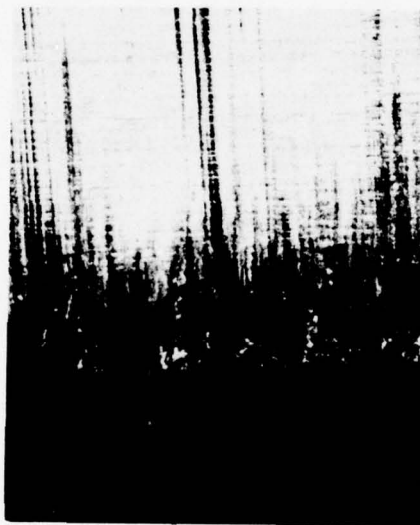


Figure 59: Micrograph of the Leading Edge of an AM 355 Blade Tip After Interaction with Material A-2 NiCrAl. Blade was rotating at 187 ft/sec (57 m/sec) and had an incursion rate of 0.010 in/sec (250 μ m/sec). 35X



Figure 60: Micrograph of Material A-2 NiCrAl After Interaction
with AM 355 Blade Tips Showing Smeared Areas 65X

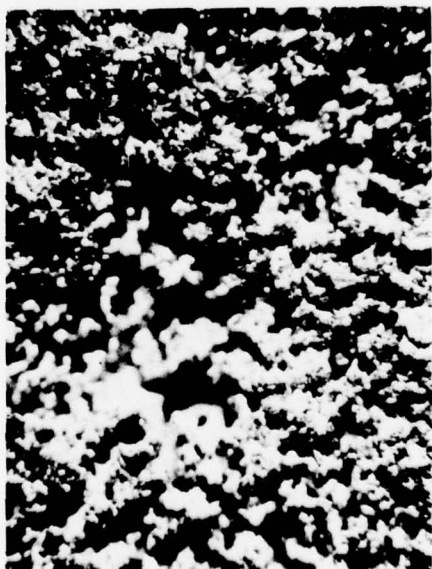


Figure 61: Micrograph of Material A-2 NiCrAl After Interaction
with AM 355 Blade Tips Showing Areas of Pull-Outs 35X



Figure 62: Large Particle Size Debris Collected After
Rub Interaction Between AM 355 Blade Tips
and Material A-2 NiCrAl 65X

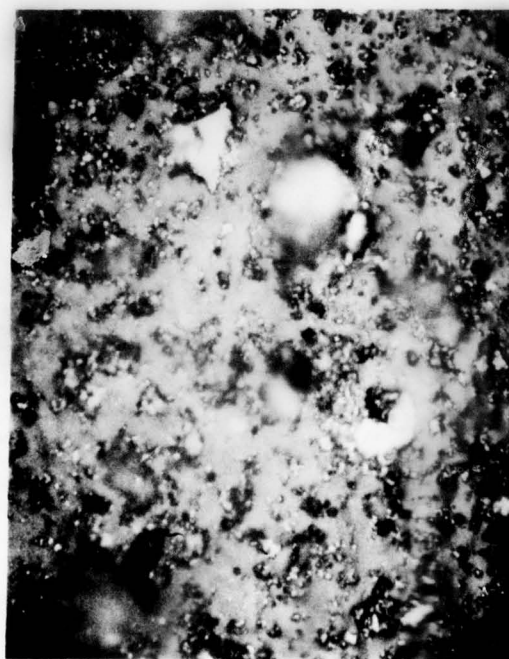


Figure 63: Fine Particle Size Debris Collected After
Rub Interaction Between AM 355 Blade Tips
and Material A-2 NiCrAl 327X

The very fine particles are thought to have been generated directly by the rub process and to consist of both the NiCrAl from which the seal material is made and the AM 355 blade tip material.

The results of this investigation indicate that:

Frictional and radial loads of the high strength seal material were about 25% higher than those measured for the lower strength material. No significant differences in blade tip wear were observed for the two NiCrAl seal materials.

Wear of the NiCrAl seal materials was characterized by material removal to a depth greater than the incursion depth, indicating possible scouring effects or secondary particle interactions.

Wear to the blade tips was by a plowing mechanism.

IV. TRANSPIRATION-COOLED SHROUD DESIGN AND EVALUATION

The transpiration-cooled shroud design calls for three functional layers: an abradable layer, a flow control layer, and a support structure. The previous section of this report, "Abradable Material Optimization", was dedicated to the selection of the abradable layer. The design and evaluation of the other two members are presented in this section of the report.

1. Plenum Design

Purpose - The purpose of this test was to determine experimentally the plenum design which will most efficiently cool the surface of the abradable material to below 1900°F (1040°C) when exposed to a 2600°F (1430°C) flame temperature. The support structure must utilize the cooling air efficiently by supplying the cooling air only to the areas of the abradable surface which would normally operate at above 1900°F (1040°C) in the test rig.

Procedure - The jet exhaust rig, shown in Figures 64 and 65, provides test conditions similar to those produced in an actual jet turbine engine. The jet exhaust rig is a small jet engine consisting of a burner can with a convergent exhaust nozzle.

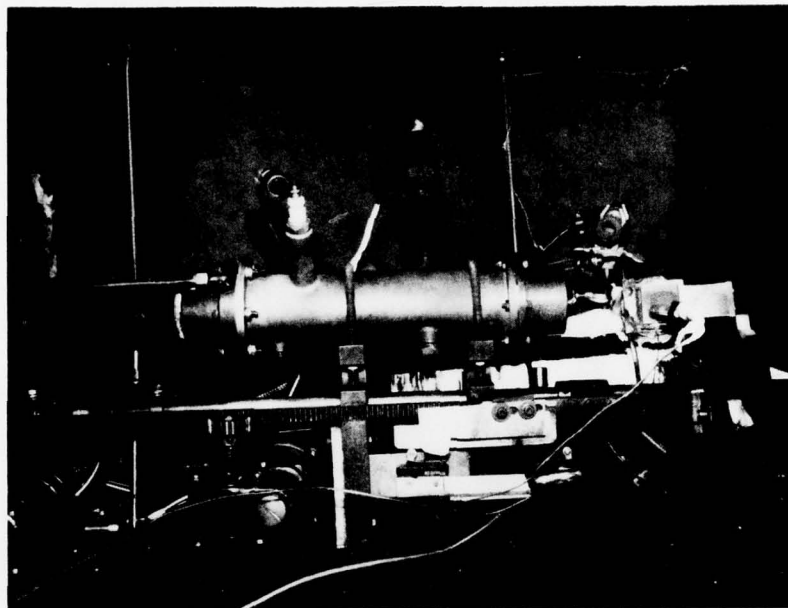


Figure 64: Jet Exhaust Rig

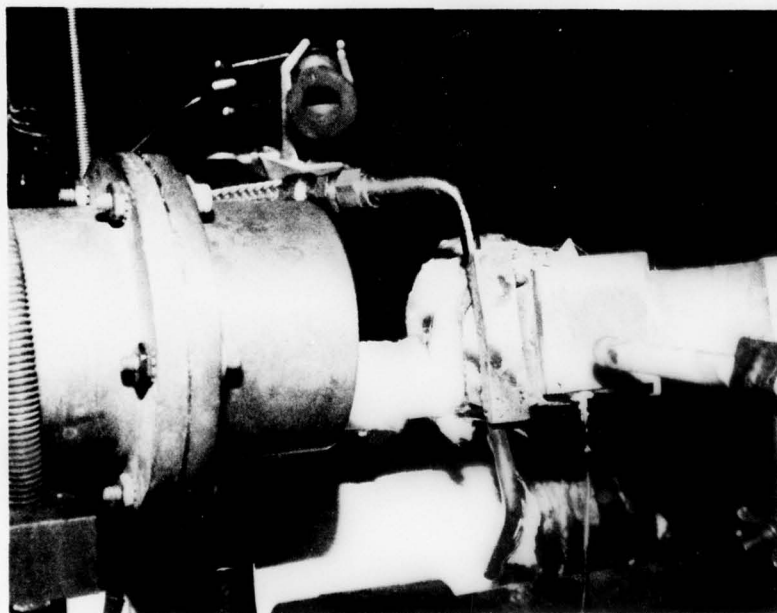


Figure 65: Jet Nozzle and Sample

Combustion air, furnished by an 80 (38 l /sec) CFM reciprocating air compressor, and Jet "A" fuel, which is injected into the burner through a domestic oil furnace nozzle, are mixed in the burner. The hot gas stream is developed by supplying a spark to ignite the mix. The jet exhaust rig is capable of developing a gas stream temperature in excess of 3200°F (1760°C) and gas velocities up to Mach 1 at the nozzle. Figure 66 is a schematic of the jet exhaust rig.

The jet exhaust rig is a flexible piece of equipment which can be adapted to produce many different test conditions. Included in this list of variable test conditions are: the gas stream temperature and velocity; the sample orientation and location; and the cooling air temperature, pressure, and flow rate. These variables can be controlled and/or monitored at the test stand.

As a starting point, the support structure designed for Contract F33615-76-C-2026 (Figures 67 and 68) was used in some preliminary tests. The support structures were made from Inconel 600 (a Ni-Cr-Fe alloy) and contained three air plenums which ran from leading to trailing edges (lengthwise). Each plenum was designed to be supplied with cooling air through orifices of either 0.015 in (381 μ m), 0.018 in (457 μ m), or 0.025 in (635 μ m) diameter. (In the initial contract, at least four such holes were required in each chamber to give a relatively uniform air distribution. This arrangement, however, did not give a uniform surface temperature free of hot and cold spots.)* Several changes in the plenum design were deemed necessary.

The orientation of the plenums was changed by rotating the support structure 90° with respect to the gas stream. This change made possible the control of the amount of cooling air distributed to each of the parallel regions (above the plenum chambers) from the leading to the trailing edge independently of one another.

A change in the size of the support structure was made from 1 1/4 in (3.2 cm) by 3 in (7.6 cm) to 1 1/2 in (3.8 cm) by 1 1/2 in (3.8 cm). This change reduced the surface area outside of the jet stream and thereby minimized the heat loss through the support structure.

* Technical Report AFAPL-TR-75-12

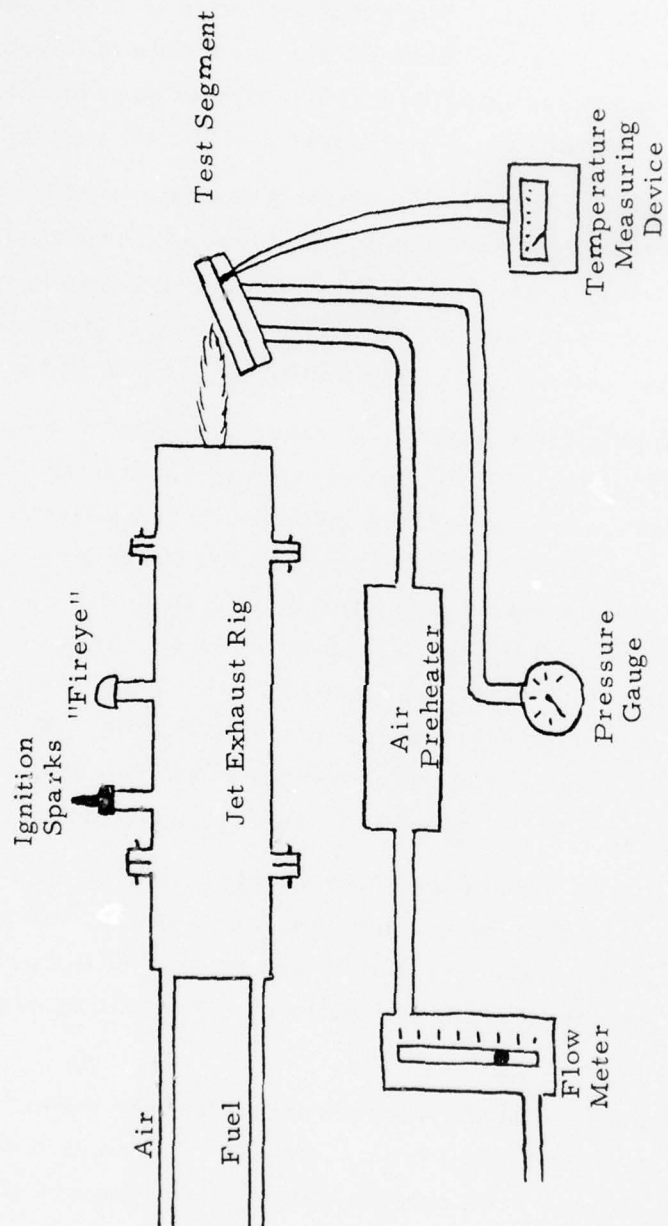


Figure 66: Schematic of Jet Exhaust Rig

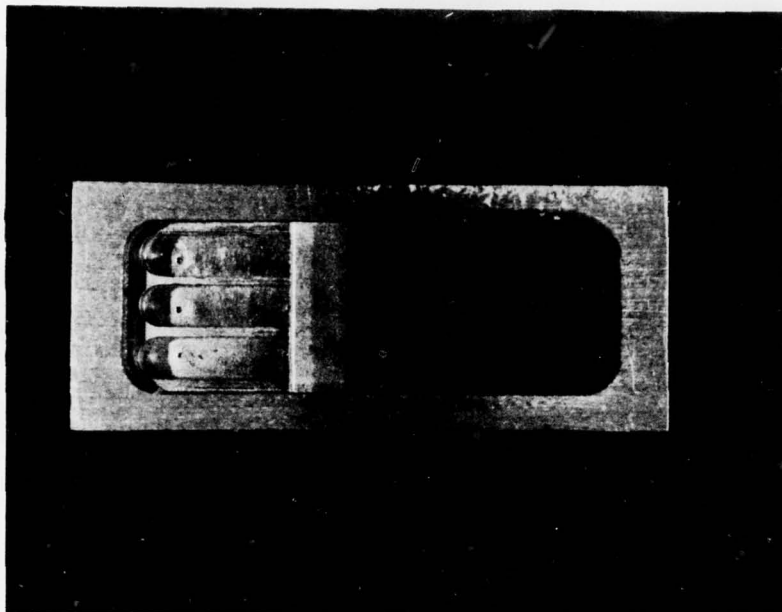


Figure 67: Cut-Away View of Transpiration-Cooled Shroud Used in Contract F33615-76-C-2026

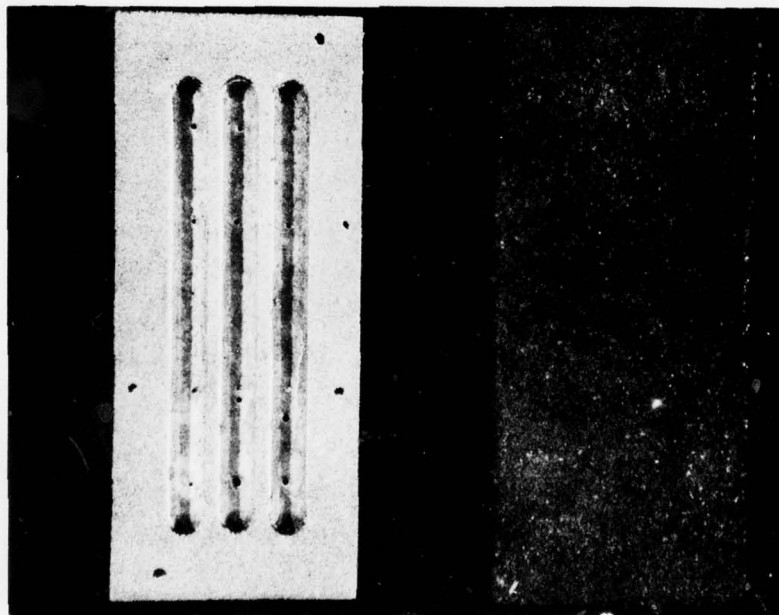


Figure 68: Transpiration-Cooled Shroud Initially Used in This Contract

Also, it made the support structure similar in width to actual engine shroud segments.

Unlike the support structure used in the initial contract which merely supplied cooling gas to the porous metal layers, the support structures tested in this program were in all cases the site of the major cooling gas pressure drop and the support; thereby controlling the cooling gas flow. The cooling air injection orifices were reduced to 0.010 in (250 μ m) in size and angled to the base plane. The numerous smaller holes were used to achieve a more uniform cooling air distribution. The angled arrangement was used to provide a mechanism to disperse the air and reduce its velocity prior to its passing through the flow control layer.

An additional plenum chamber was also added because of the increased width of the support structure. For the initial tests, two support structures were made. Distribution of the air to the four plenum chambers was in the following ratios: for the first support structure, 1/4, 1/4, 1/4, 1/4; and, for the second support structure, 1, 0, 0, 0. These arrangements are shown in Figures 69 through 72.

Additional testing was done on three other variations of the support structure. The first, shown in Figure 73, had only a single plenum chamber at the leading portion; the second, shown in Figure 74, had two plenum chambers at the leading half of the support structure; and the third, shown in Figures 75, 76, and 77, replaced the plenum chambers with a series of small holes, which were located at the leading half of the support structure. In all three designs, the cooling air injection orifices were located on the back of the support structure near the trailing edge (Figures 73, 74, and 77). By forcing the cooling air to traverse the length of the support structure from the trailing to the leading edge before being exhausted through the abradable material, the velocity of the air is reduced and the air can be more completely dispersed. Also, the cooling air removes heat which has been conducted through the support structure before being used to transpiration cool the lead edge.

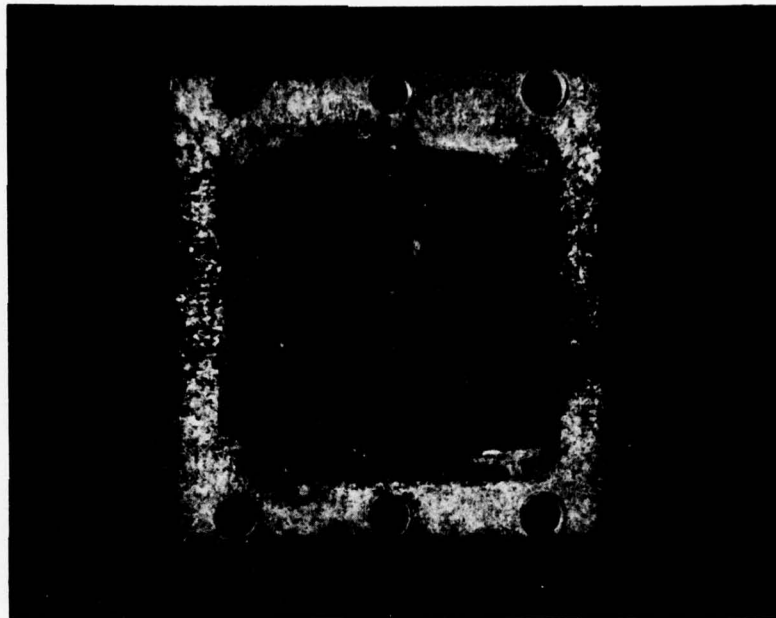


Figure 69: Support Structure with Uniform Cooling Air Distribution 2X

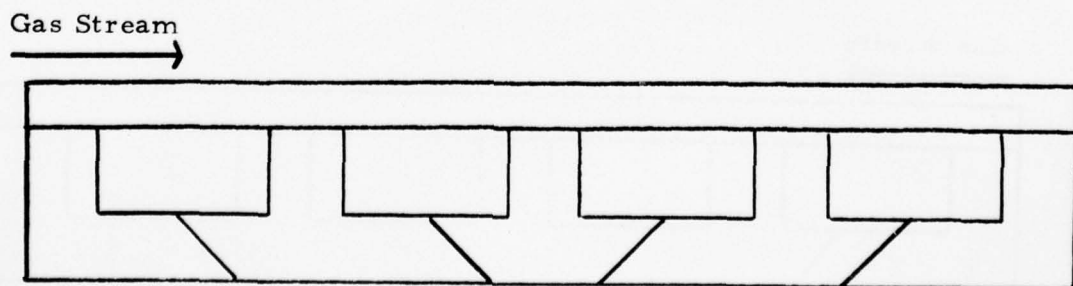


Figure 70: Schematic of Support Structure with Uniform Cooling Air Distribution

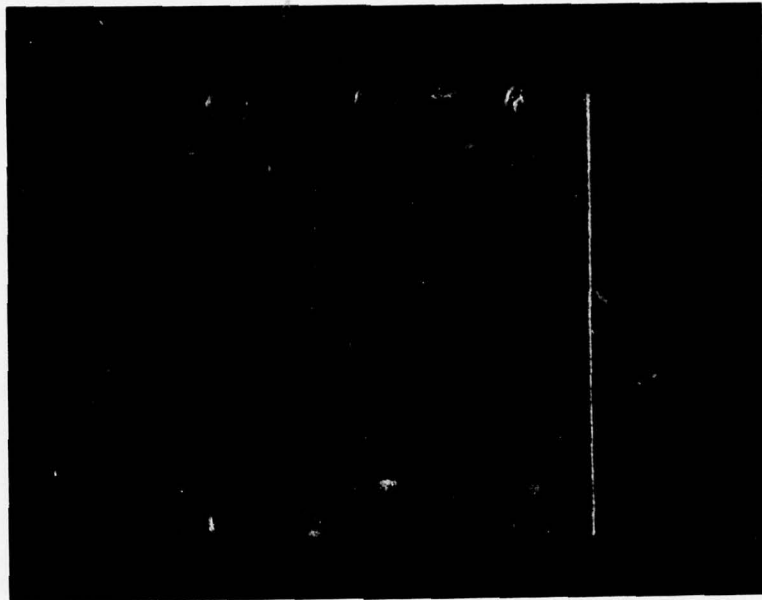


Figure 71: Support Structure with Preferential Cooling to the Lead Chamber 2X

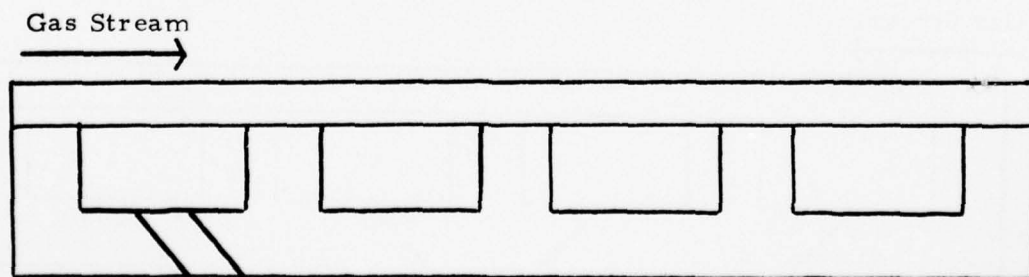


Figure 72: Schematic of Support Structure with Preferential Cooling to the Lead Edge

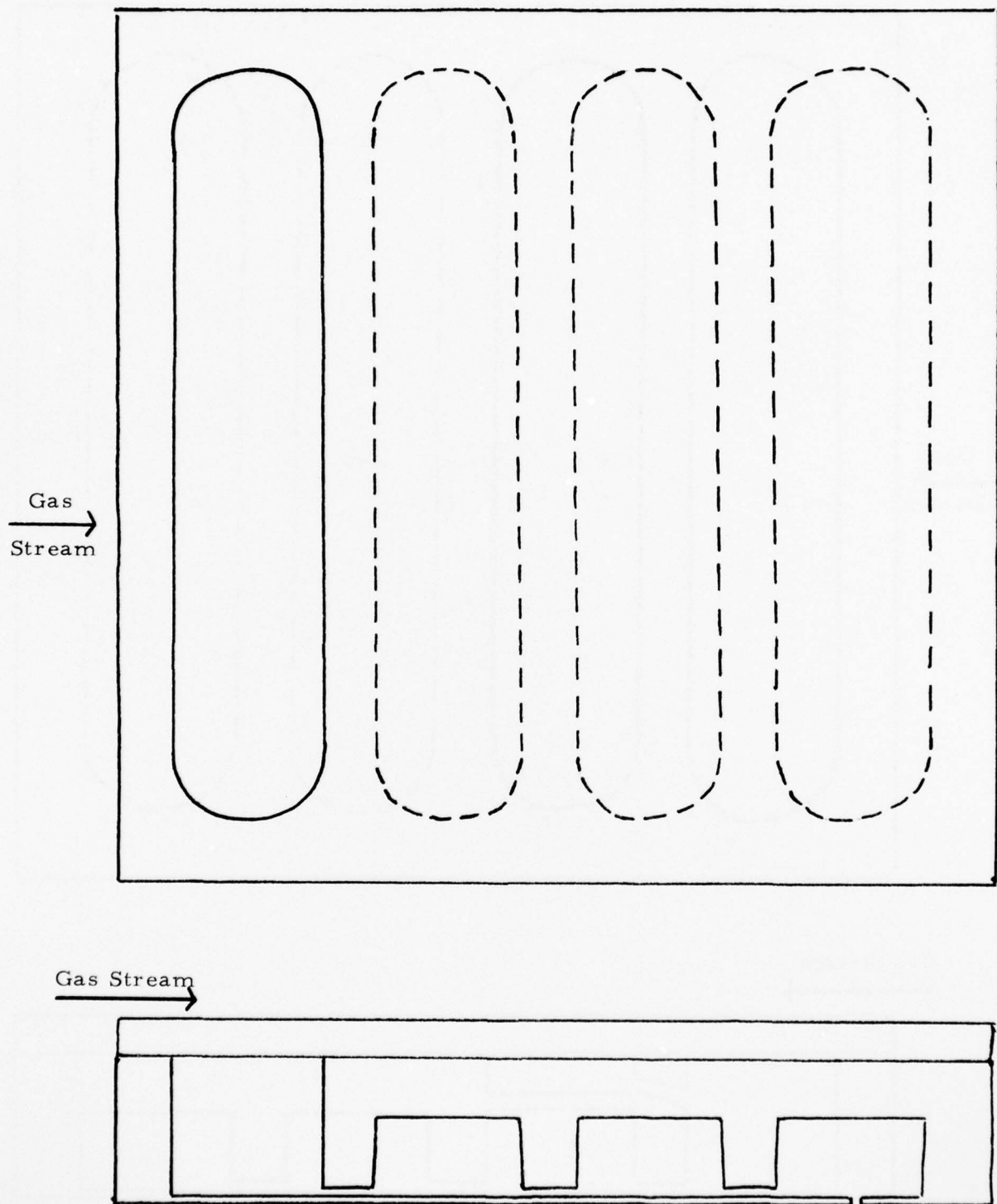


Figure 73: Support Structure with Open Plenum Chambers at the Lead Edge

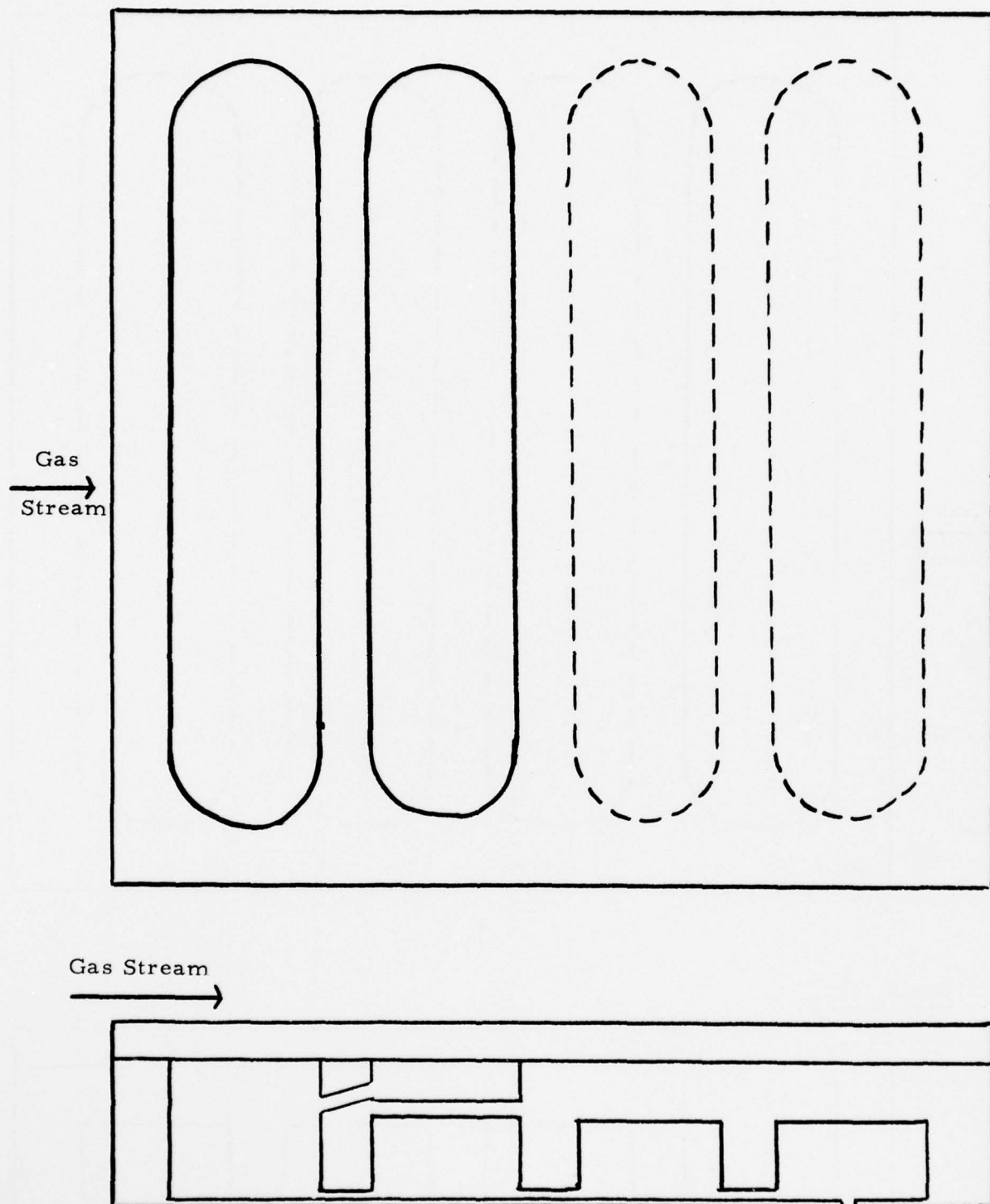


Figure 74: Support Structure with Two Open Plenum Chambers at the Lead Edge

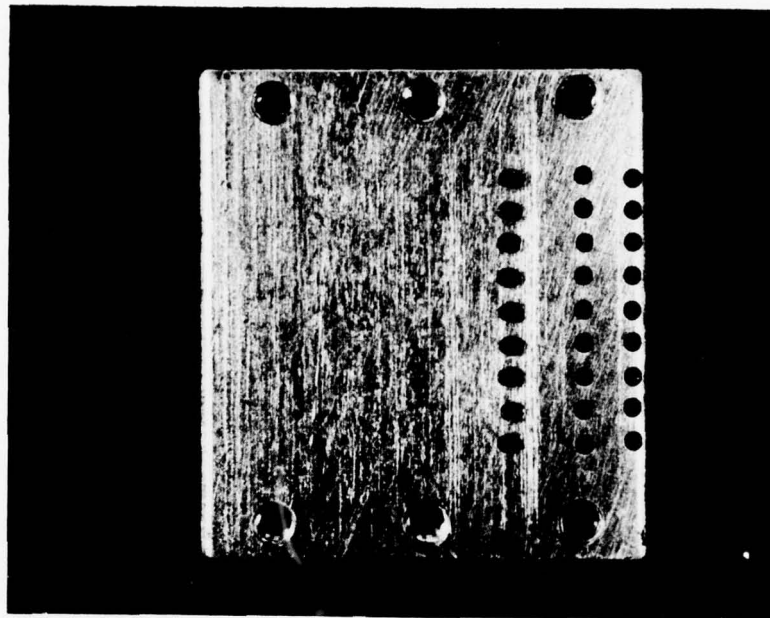


Figure 75: Surface of Optimum Support Structure Design 2X

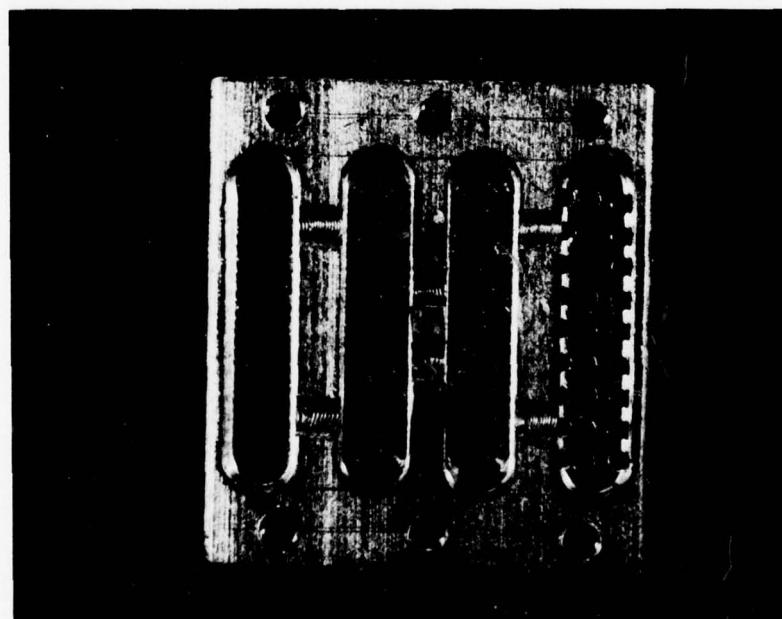


Figure 76: Substrate of Optimum Support Structure Design 2X

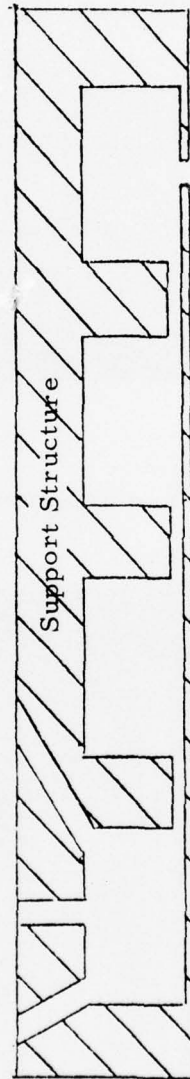


Figure 77: Schematic of Optimum Support Structure Design

To complete the test shroud segments, a bi-layer structure fabricated from Material A-1 and A-2 was brazed to the five different support structures. The test segments were mounted vertically at 30° with respect to the jet exhaust stream. A gradual temperature drop was obtained across the sample surface from the leading to the trailing edge. The leading edge of each test segment was positioned 4 in (10.2 cm) from the nozzle, where the gas temperature was 2600°F (1430°C) at a calculated velocity of 0.7 Mach. Because of the limited size of the jet exhaust stream, a hot band (from leading to trailing edges) of approximately 1 in (2.54 cm) in width was generated. Of this distance, only the center 0.5 to 0.75 in (1.27 to 1.90 cm) reaches maximum temperature (for that distance from the jet nozzle). The cooling air was specified at 1200°F (650°C); therefore, this temperature was duplicated in this test. A 30 psi (210 KPa) pressure drop across the support structure was maintained. This pressure drop was maintained by application of a surface pressure of 5 psig (34.5 KPa) and a pressure on the back of the support structure of 35 psig (241 KPa). The target flow rate for all of the segments was 25 SCFH (11.8 l /min).

Under these conditions, each segment was subjected to 10 test cycles consisting of seven minutes in the gas stream and three minutes out. An optical pyrometer and a radiation pyrometer were used to measure the temperature at several locations from the leading edge to the trailing edge in the center of the hot band. The surface temperatures were measured for different flows of cooling air on the different support structures. Chromel-Alumel thermocouples were used to measure the temperature at the flow control layer/support interface. These data are presented in graphic form.

Results and Discussion - This test yielded a new support structure design which could be adapted to engines presently using heavy cast shroud segments in the high pressure turbine section. The design of this support structure, which is referred to as the optimum support structure, evolved as a result of extensive testing of several prior designs.

In the first test, equal quantities of cooling air were supplied to each plenum of the initial test support structure, shown in Figure 69, which gave a uniform temperature drop across the abratable surface. Since the trailing edge never exceeded 1900°F (1040°C) under rig test conditions, any cooling air supplied to plenums 3 and 4 was not required to maintain the seal at a usable temperature (Figure 78). It was concluded that preferential cooling to the leading half of the surface would be a more efficient use of the cooling air.

The second support structure tested was shown in Figure 71. This basic design was the same as that for the initial support structure, but all of the air was supplied to the first plenum chamber. This arrangement resulted in a better utilization of cooling air (Figure 79), but it still was not adequate. There were some faults with the basic design of the support structure:

There were four 1 1/4 in (6.35 mm) wide plenum chambers which had to be spanned in the support structure. This design required that either an abratable layer with a higher strength be used or that a second layer be inserted between the abratable layer and the support structure. Although the second choice was the most likely, neither was totally acceptable. Increasing the strength of the abratable would reduce its rub tolerance capabilities. Putting in a second layer would reduce the depth to which a good rub could be achieved.

Also, the support structure required that the air be supplied to the plenums through orifices no larger than 0.010 in (250 μ m) in diameter (see Figures 69 and 71). This design caused two problems. First, the holes were extremely difficult to fabricate into the support structure. Second, once fabricated, they are difficult to keep open during the brazing operation required to attach the abratable layer. Also, during rig testing, they tended to become plugged by oxide scales or other small particles carried by the cooling air stream. When the orifice diameter exceeded the specified size, cold spots developed on the abratable surface. Because of the velocity of the cooling air stream, these cold spots appeared even when a flow control layer having a finer pore size was placed between the abratable layer and the support structure. Increasing the angle of the larger holes to 45° with respect to the abratable surface did not cause sufficient air dispersion to eliminate cold surface spots.

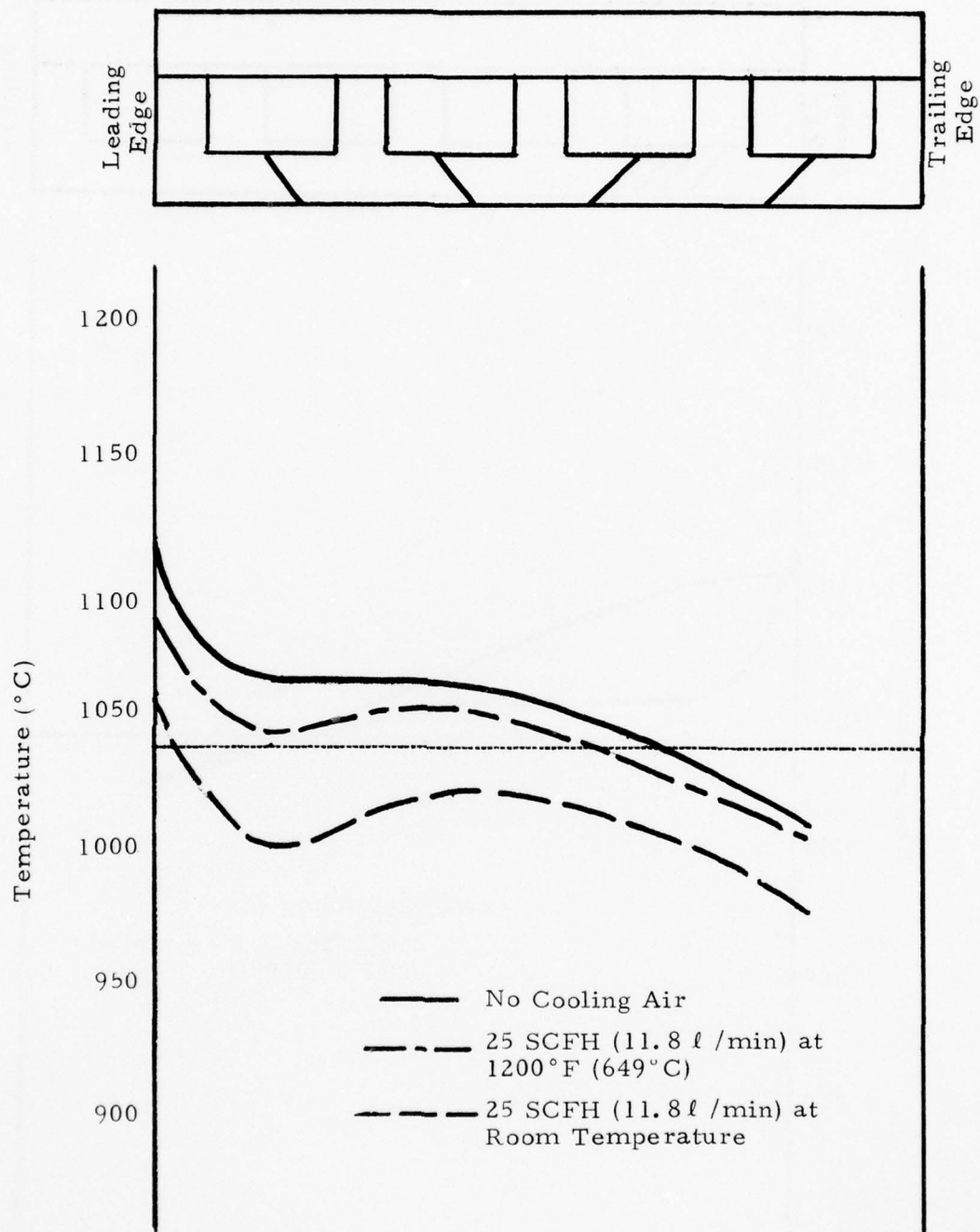


Figure 78: Temperature Profile Across the Surface of the Shroud Segment with Uniform Cooling Air Supplied to Each Plenum Chamber

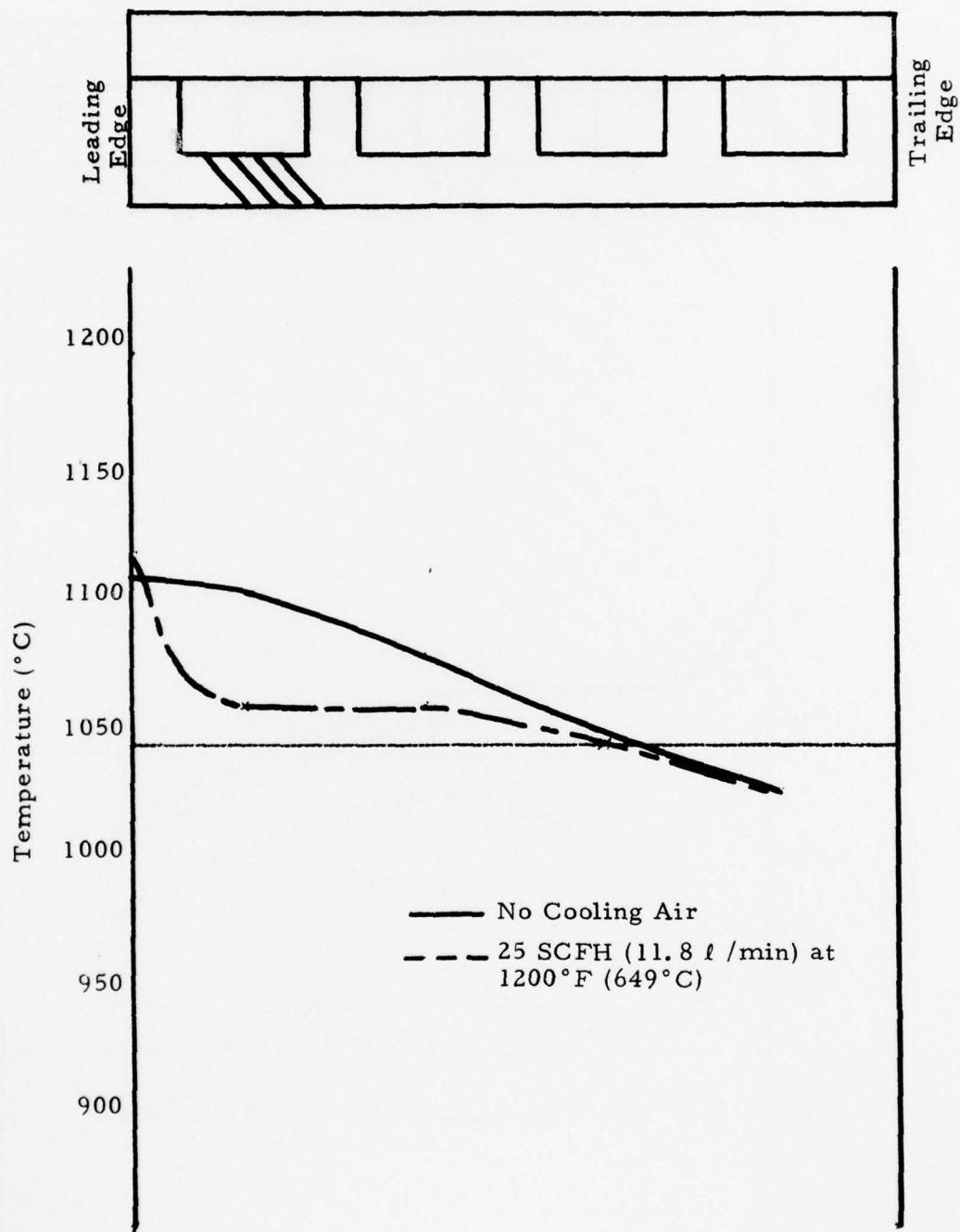


Figure 79: Temperature Profile Across the Surface of the Shroud Segment with Preferential Cooling Air Supplied to the Lead Edge Chamber

In addition, the lack of contacts between the abradable layer and the support structure caused a restriction on the amount of heat conducted through the shroud. During testing, the unsupported sections of the NiCrAl abradable layer were hotter than the supported sections when no cooling air was supplied. This condition could occur if the orifices supplying air to the plenums became plugged, an occurrence which might cause potential oxidation problems. Figures 80, 81, and 82 show the effect of conductive cooling on surface temperature.

As a result of these considerations, a third support structure was designed, which is shown in Figure 73. This structure was designed to:

Reduce the number of open plenum chambers from four to one and thereby reduce the number of unsupported regions.

Preferentially supply cooling air to the leading edge of the sample.

Allow for easier fabrication of the cooling air orifices. Instead of locating orifices directly into the plenums, they were positioned behind several baffles (Figure 77) to allow for more complete dispersion of the air prior to reaching the abradable layer. The sixteen (16) 0.010 in (250 μ m) diameter holes, which were difficult to fabricate, were replaced by three (3) 0.020 in (500 μ m) diameter holes. The number and size of holes were selected to control the flow and pressure drop in the system.

Provide a better heat conduction path. With the last three plenums closed there were more contact points between the abradable layer and the support structure.

Although this design was closer to that which was actually needed, the area immediately behind the transpiration cooled section did not receive sufficient conduction cooling to achieve the desired temperature profile. As a result, the second chamber was reopened, giving rise to a fourth support structure, shown in Figure 74. This design did give a more uniform surface temperature distribution (Figure 83). However, it brought a return to the potential problem of poor heat transfer if plugging of the flow control orifices were to occur. Also, this increased the number of unsupported areas of the porous layers.

AD-A051 000

UNION CARBIDE CORP PARMA OHIO PARMA TECHNICAL CENTER
RUB TOLERANT MATERIALS DEVELOPMENT. NICKEL-CHROMIUM-ALUMINUM FO--ETC(U)
OCT 77 R J DUFALA

F/G 21/5

F33615-76-C-2098

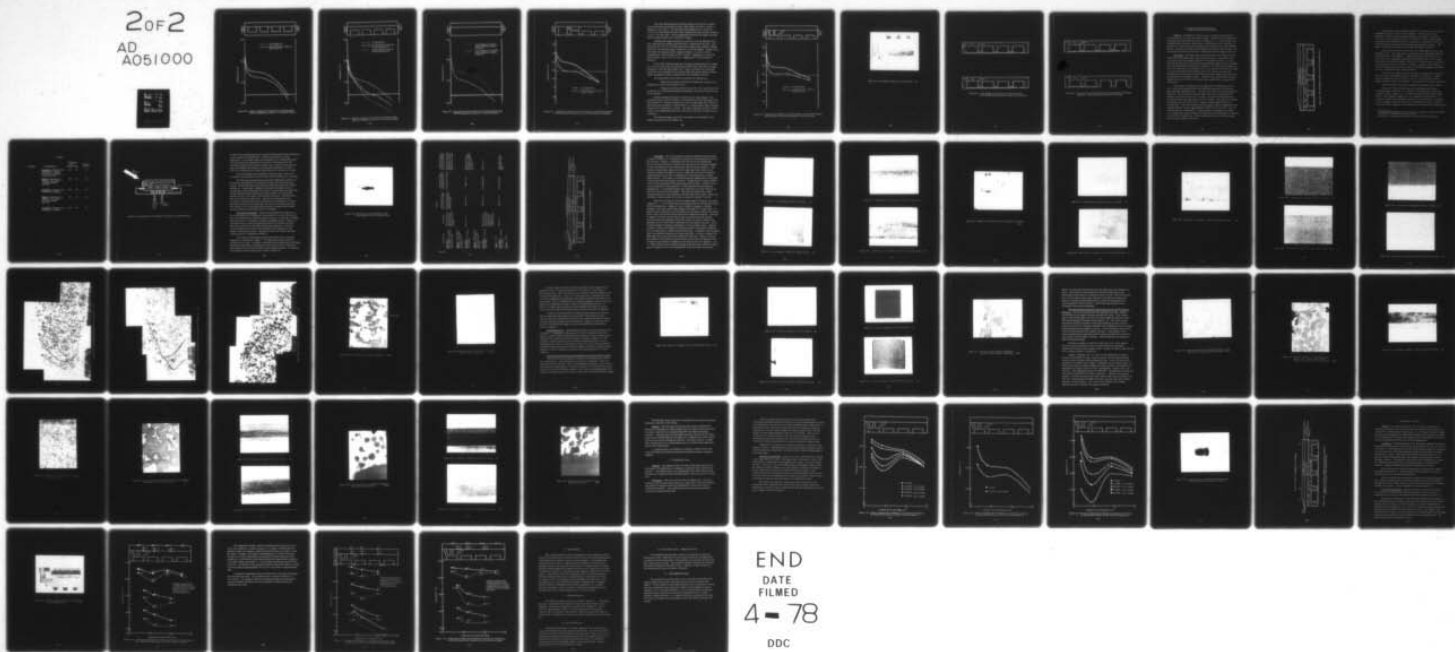
NL

AFAPL-TR-77-46

UNCLASSIFIED

20F2

AD
A051000



END

DATE
FILMED

4-78

DDC

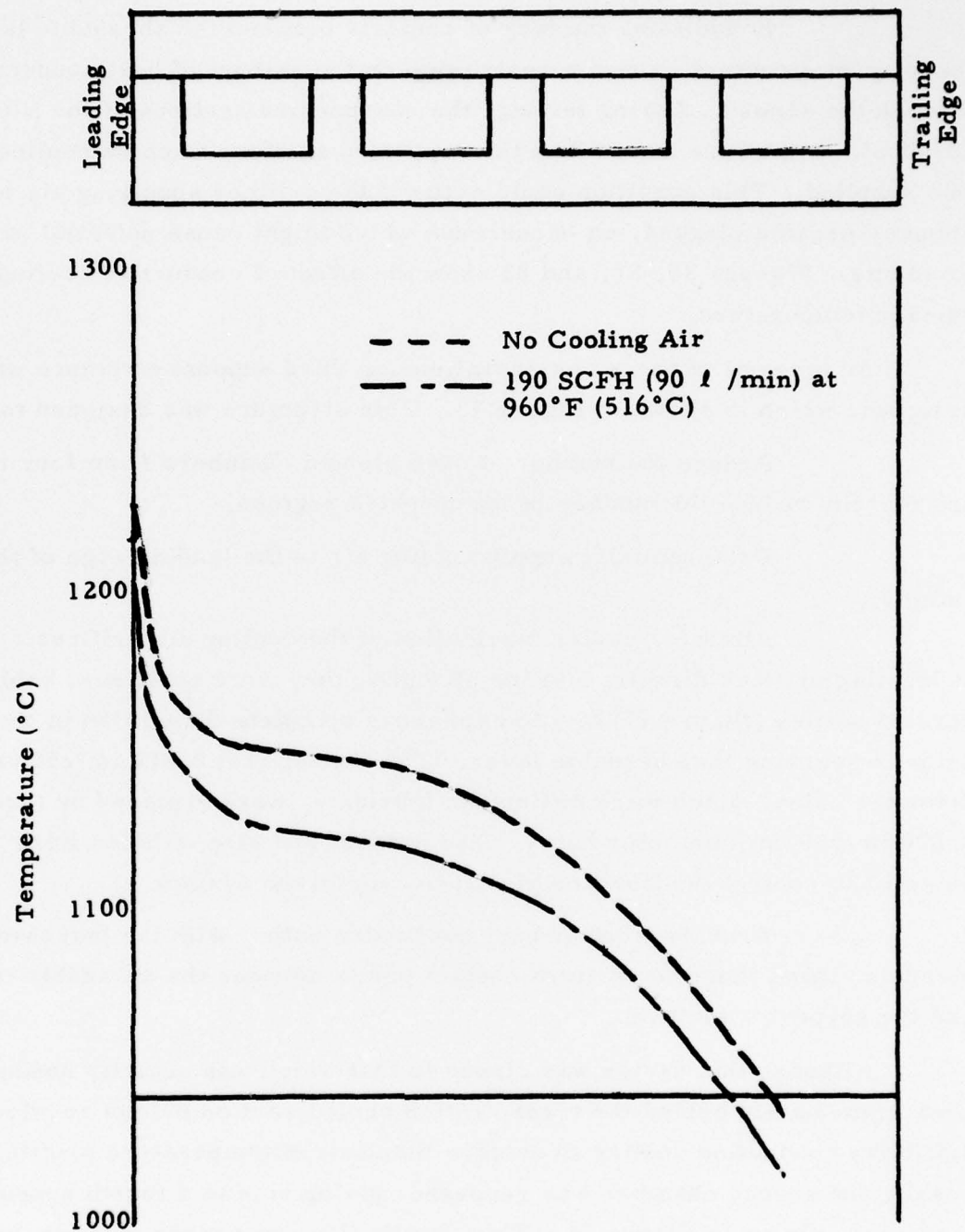


Figure 80: Surface Cooling of the Shroud by Conducting Heat Away by Impinging Cooling Air on the Back Surface

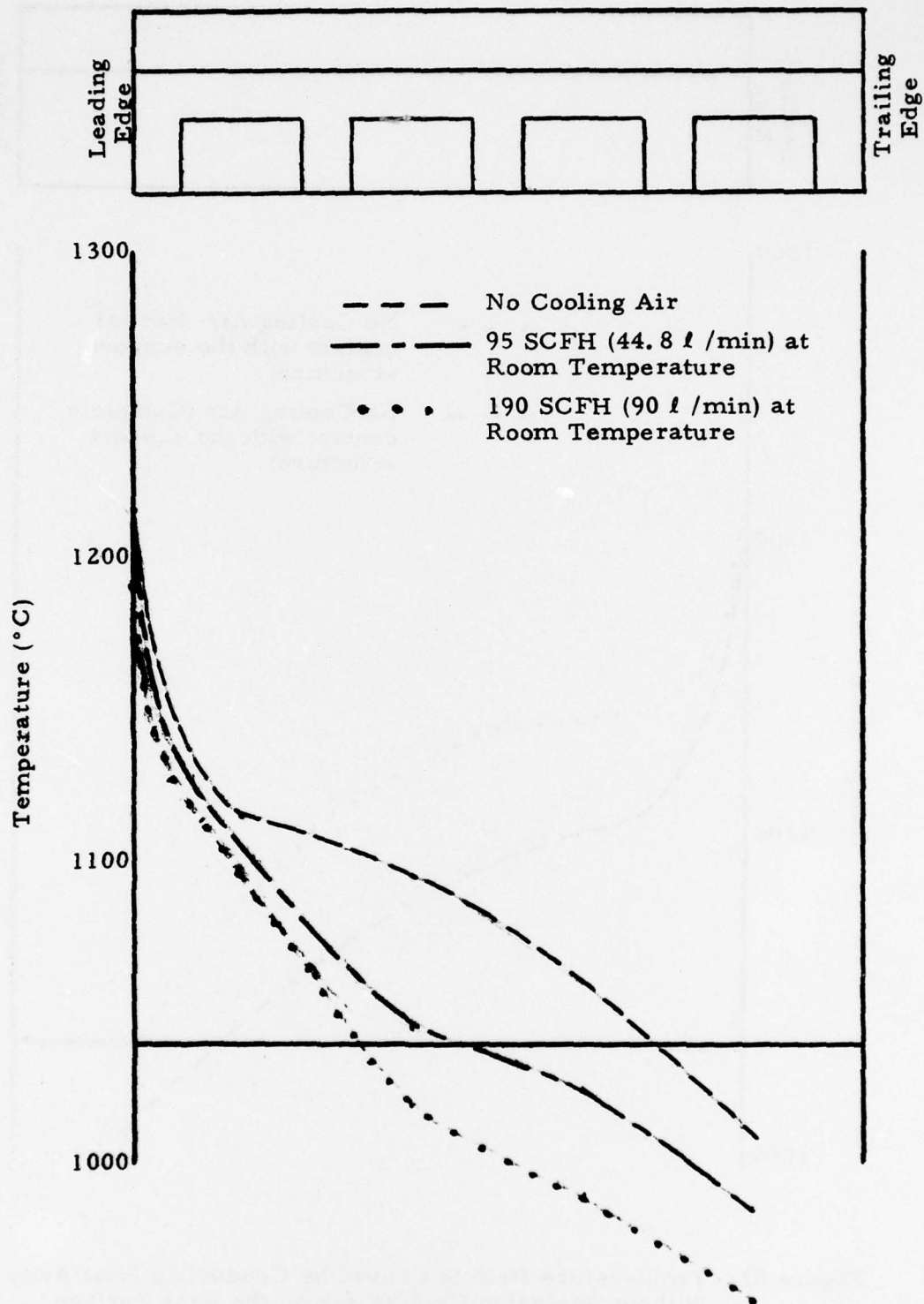


Figure 81: Surface Cooling of the Shroud by Conducting Heat Away by Impinging Cooling Air on the Back Surface

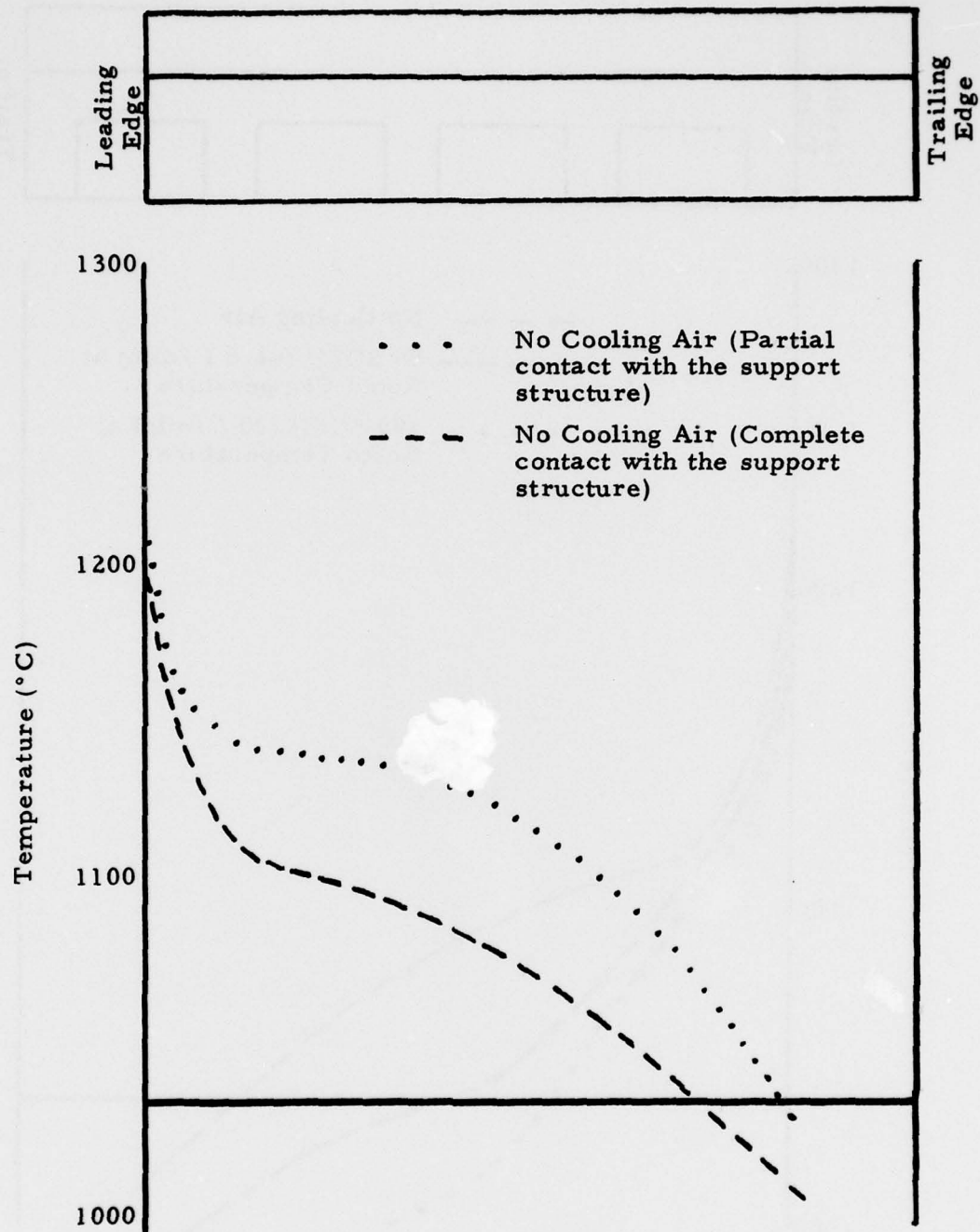


Figure 82: Temperature Profile Caused by Conducting Heat Away Without Impinging Cooling Air on the Back Surface

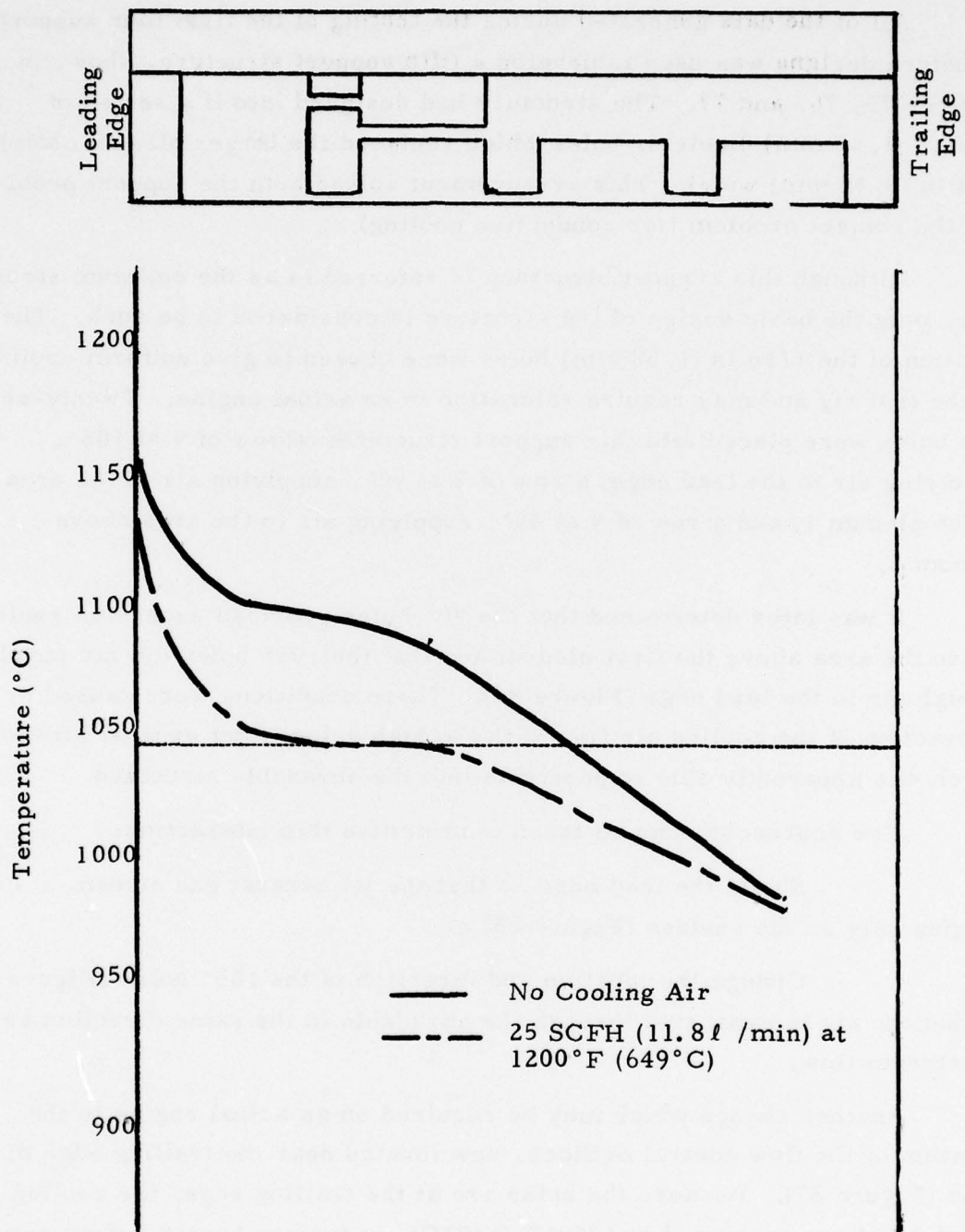


Figure 83: Temperature Profile Across the Surface of the Shroud Segment with Preferential Cooling to the Two Lead Plenum Chambers

All of the data generated during the testing of the first four support structure designs was used to develop a fifth support structure, shown in Figures 75, 76, and 77. The structure had designed into it a series of 1/16 in (1.58 mm) diameter holes which replaced the larger plenum chambers (1/4 in (6.35 mm) wide). This arrangement solved both the support problem and the contact problem (for conductive cooling).

Although this support structure is referred to as the optimum structure, only the basic design of the structure is considered to be such. The position of the 1/16 in (1.58 mm) holes were chosen to give uniform cooling on the test rig and may require relocation in an actual engine. Twenty-seven (27) holes were placed into this support structure: a row of 9 at 105°, supplying air to the lead edge; a row of 9 at 90°, supplying air to the area above plenum 1; and a row of 9 at 45°, supplying air to the area above plenum 2.

It was later determined that the 90° holes provided excessive cooling air to the area above the first plenum and that the 105° holes did not supply enough air to the lead edge (Figure 84). These conditions were caused by interaction of the cooling air flow with the high velocity jet exhaust stream, which was apparently able to penetrate into the abradable structure.

Two approaches can be taken to minimize this interaction:

Shield the lead edge so that the jet exhaust gas stream is impinging only on the surface (Figure 85) or,

Change the location and direction of the 105° holes (Figure 86) to that the air is exhausted through the abradable in the same direction as the jet stream flow.

Another change which may be required on an actual engine is the location of the flow control orifices, now located near the trailing edge of the shoe (Figure 87). Because the holes are at the trailing edge, the cooling air, which has been preheated to 1200° F (649° C), is further heated before actually being used for transpiration cooling. Therefore, placement of these orifices closer to the leading edge may prove to be a more efficient utilization of the cooling air.

The optimum support structure was used for the remainder of the testing required on the jet exhaust rig.

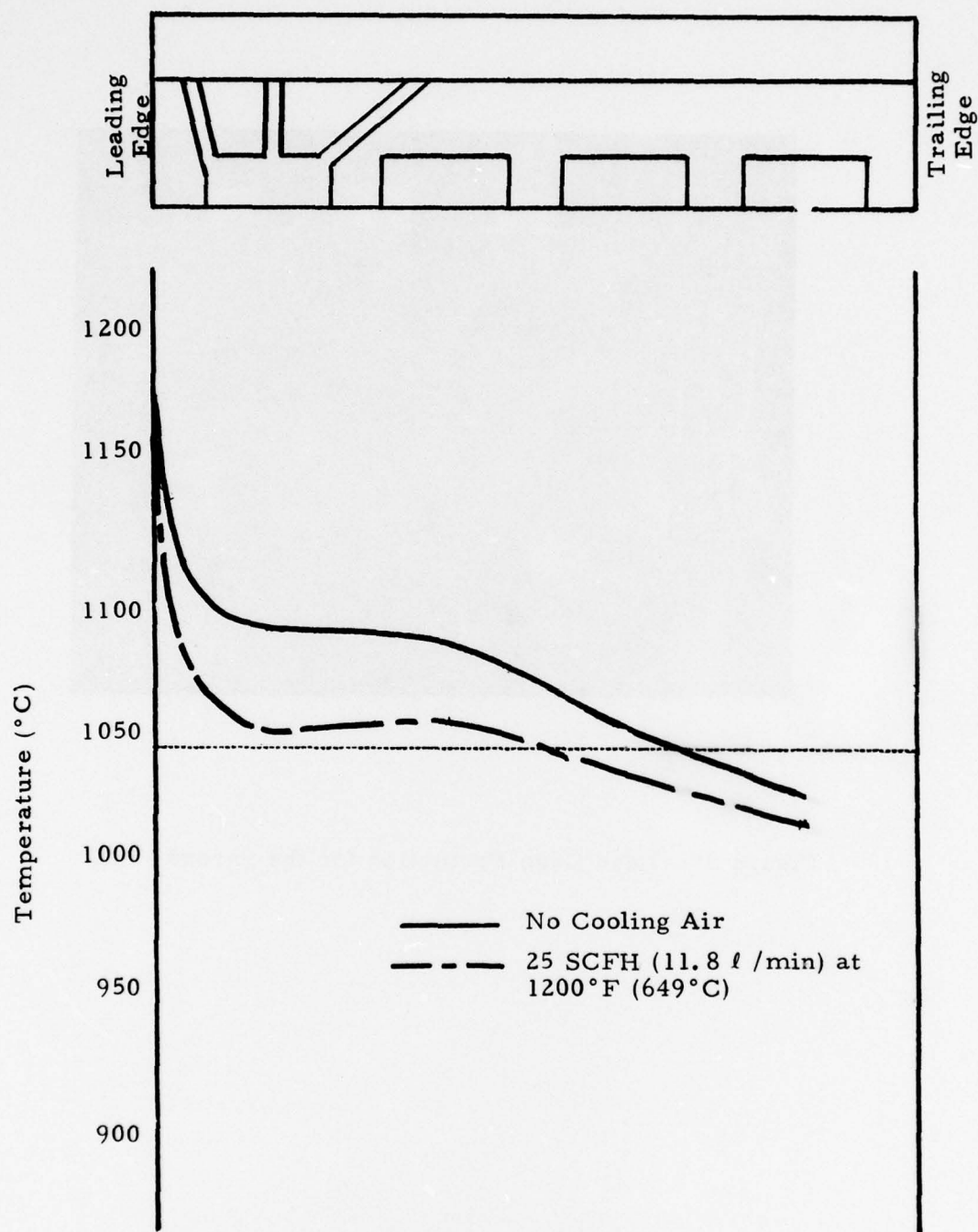


Figure 84: Temperature Profile Across the Surface of the Shroud Segment Which Utilizes the Optimized Support Structure Design

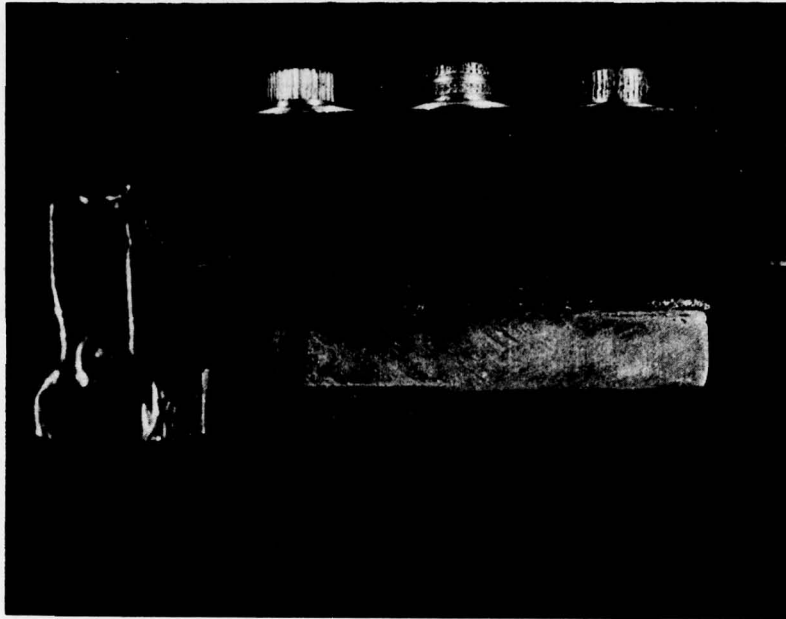


Figure 85: Lead Edge Protection for the Shroud 2X

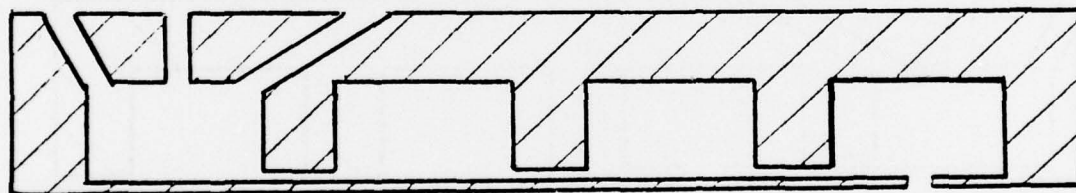
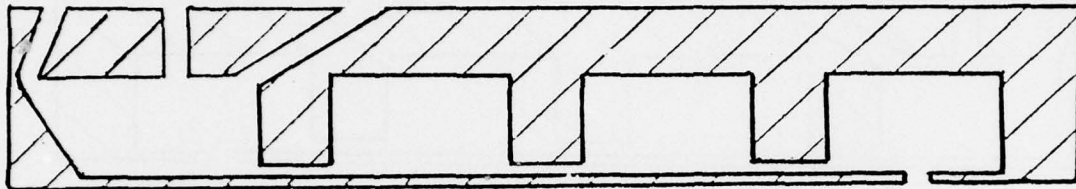


Figure 86: (Top) Change in Direction of Cooling Air Holes
from the Optimized Design for Rig Testing (Bottom)

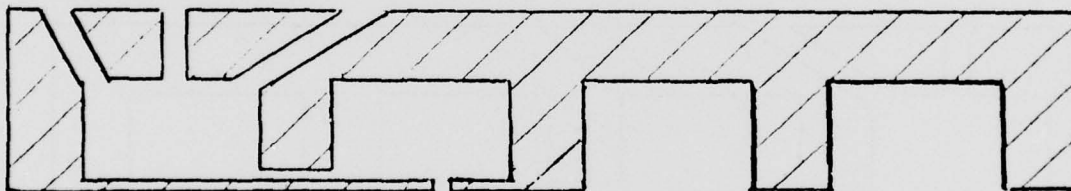
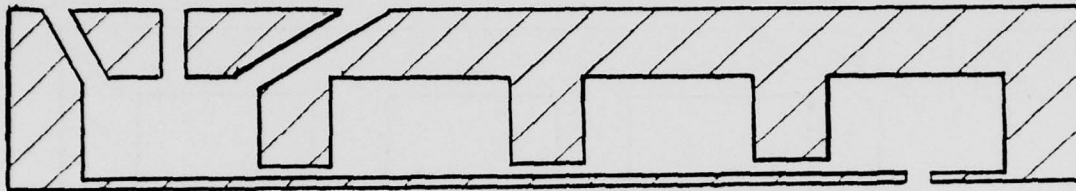


Figure 87: (Top) Location of Injection Orifices of the Optimized Support Structure. (Bottom) Proposed Alternative Design

2. Thermal Cycle/Hot Gas Erosion Testing for Structure Optimization

Purpose - The purpose of this test was to design a porous NiCrAl structure for use as a part of the HPT shroud. The shroud would support the abradable layer and control the flow of cooling air to it. This structure was evaluated under oxidation, thermal shock, and hot gas erosion conditions to determine the effect that these conditions had at the lead edge, the abradable surface, the interface between the abradable and the flow control layers, and the interfacial bond between the flow control layer and the support structure.

Procedure - Past experience (Contract F33615-76-C-2026) has indicated that the abradable layer of the shroud may have to span large (1/4 in (6.35 mm) wide) open plenum chambers in the support structure. It was required that the flow control layer provide adequate support for the abradable layer while spanning the open plenum chambers. The flow control characteristic was required for two reasons: first, to control the rate at which cooling air would flow through the abradable layer; and, second, to assure that adequate dispersion of the cooling air would prevent localized cold spots from developing on the abradable surface. However, when used with the optimum support structure, the flow control layer was required only to disperse the cooling air.

Three types of simulated shroud segments were fabricated for this test. Each of the segments had three functional areas but not necessarily three distinctly different layers. The three areas are shown schematically in Figure 88. The first area, at the shroud surface, was designed for rub tolerance and was 0.060 in (0.15 cm) thick. The area directly beneath the rub tolerant layer was also 0.060 in (0.15 cm) thick. This zone was designed to disperse and control the flow of cooling air being supplied to the rub tolerant layer. The third member was the support structure optimized in the "Plenum Design" section, approximately 0.250 in (0.64 cm) thick. The rub tolerant area was chamfered 15° on the lead edge to eliminate an extreme over-temperature condition which was observed during preliminary testing and set-up of the jet exhaust rig. (The temperatures observed at the lead edge were as high as 2282° F (1250° C).)

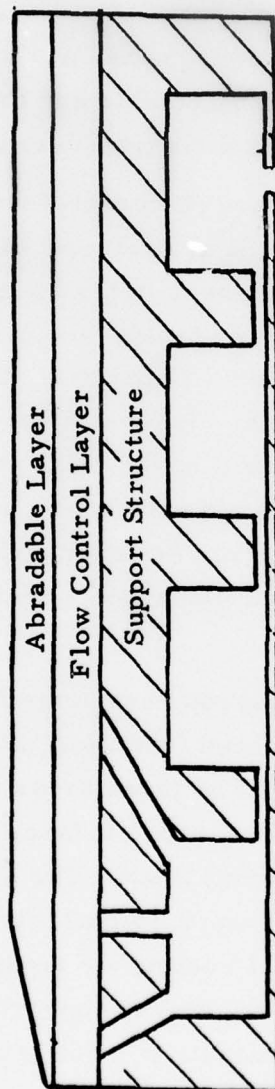


Figure 88: Shroud Segment with Its Three Functional Layers

Material A-2, with a strength of 2400 psi (16.5 KPa), was used as the abradable structure in the first test segment. The flow control layer (Material A-1) had a tensile strength of 5000 psi (34.5 MPa), a density of 2.8 g/cm³, and an average pore size of 0.0026 in (65 μm). The abradable layer was direct sintered to the flow control layer to eliminate the pore constriction which may result from brazing porous materials together. This bilayer structure was brazed to the Inconel 600 support structure.

The second structure used 2100 psi (14.5 MPa) Material A2* as the abradable layer. The support/flow control layer was considerably different from that used in test segment 1. Spherical particles (Material B) were used rather than irregularly-shaped particles (Material A). The resultant structure had a tensile strength of 7500 psi (51.7 MPa), a density of 4.2 g/cm³, and an average pore size of 0.0014 in (35 μm). Because of the small pore size, the support layer was direct sintered to both the abradable layer and to the shoe, avoiding the braze wicking problem.

The third test segment, which consisted of a single layer of Material A2, had a tensile strength of 2100 psi (14.5 MPa), a density of 2.7 g/cm³, and an average pore size of 0.0037 in (95 μm). This structure, like the bilayer structure used in test segment 1, was brazed to the support structure.

Data pertaining to these three segments are summarized in Table 6.

Each of the three test segments was individually tested under simulated engine conditions (i. e., oxidation, thermal shock, and hot gas erosion) on the jet exhaust rig. The segments were attached to the sample holder, which supplied cooling air to the simulated shroud segment. A "Grafoil" gasket was inserted to maintain an air-tight seal. A schematic of the assembly is shown in Figure 89. Temperature, pressure, and flow rate at which the cooling air was supplied were measured at the sample holder.

* The different strength level was used since conclusive results from NASA abradability testing were not yet available.

** "Grafoil" is a registered trademark of Union Carbide Corporation.

Table 6

Sample	Composition	Pore Size (μm)		Density (g/cc)
		Large	Avg.	
1	<u>Abradable</u> - Material A-2 2400 psi (16.5 MPa) structure of irregular shaped particles	110	95	2.7
	<u>Support</u> - Material A-1 5000 psi (34.5 MPa) irregular shaped particles	80	65	2.8
2	<u>Abradable</u> - Material A-2 2100 psi (14.5 MPa)	110	95	2.7
	<u>Support</u> - Material B-2 7500 psi (51.7 MPa) spherical shaped particles	45	35	4.2
3	<u>Abradable</u> - Material A-2 2100 psi (14.5 MPa)	110	95	2.7

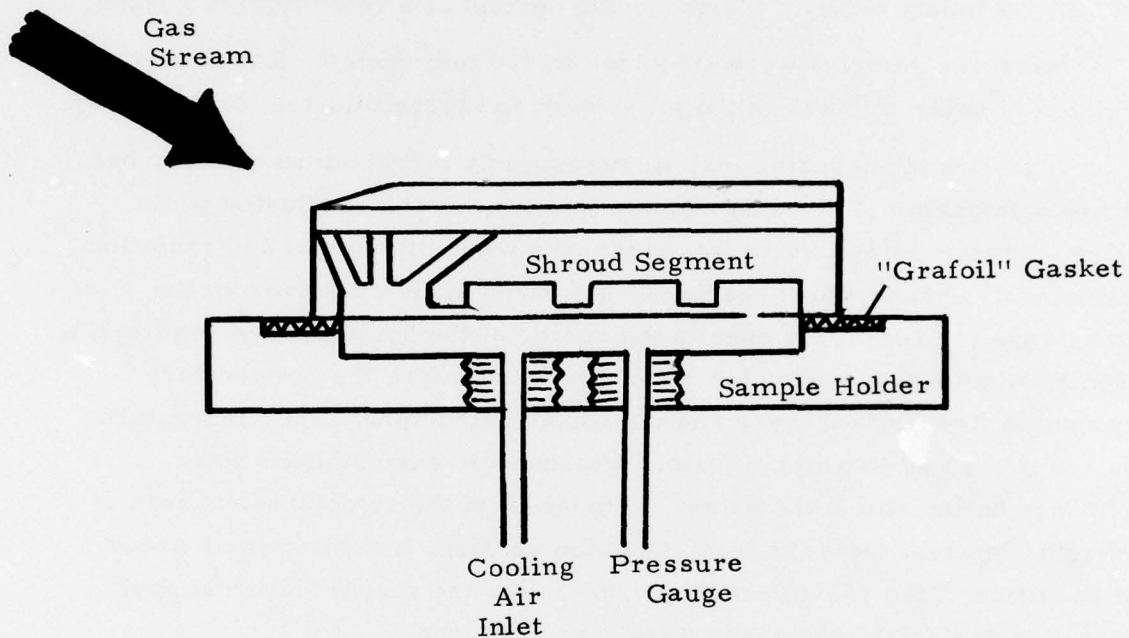


Figure 89: Schematic of Test Segment Assembly for Jet Exhaust Rig

A 1200°F (649°C) temperature and 30 psig (205 KPa) pressure were maintained on the cooling air during this test. The flow was varied for cooling optimization. The sample holder was positioned at a 30° angle with respect to the jet exhaust gas stream and at a 4 in (10.2 cm) distance from the convergent exhaust nozzle of the jet exhaust rig. At this location, the lead edge of the sample was exposed to a gas stream temperature of 2600°F (1427°C) (as measured by a thermocouple device) at a velocity of 0.7 Mach.

All three samples were subjected to 100 test cycles. Each cycle consisted of seven minutes in the jet stream and three minutes for cool down.

The data taken during testing were mainly temperature related, but microscopic examination of the sample was done at the conclusion of the testing. Surface temperature was measured with both optical and radiation pyrometers. Temperature readings were taken at five points from the leading edge to the trailing edge in the center of the hot band (see Figure 90). Chromel-Alumel thermocouples were used to measure the temperature between the flow control layer and the support structure. All temperature data are presented in graphic form. Microscopic examinations were performed to determine the extent of oxidation of the structures. Areas of particular interest were the lead edge, the surface, and the plenum areas. The condition of the rub-tolerant/support layer and support layer/support structure interfacial bond areas were also examined.

Discussion and Results - This test demonstrated that Material A-2 has the strength and air dispersion characteristics to act as a flow-control layer when attached to the optimum support structure. It also has a strength level that allows it to maintain acceptable abrasability levels. However, a protective barrier at the lead edge would reduce the amount by which the lead edge exceeded the recommended operating temperature. Since the erosion damage in this area is also attributed to the temperature, this damage would also be reduced. (Work with a protective barrier was done under the section "Temperature Profile").

The results of the thermal cycle/hot gas erosion test on each test segment are summarized in Table 7. The discussion of these results is divided into five areas: Lead Edge, Abradable Surface (Beyond the Lead Edge), Interfacial Bonds Between Abradable and Flow Control Layers, Interfacial Bond Between the Flow Control Layer and the Support Structure, and General. The location of each of these areas is shown in Figure 91.

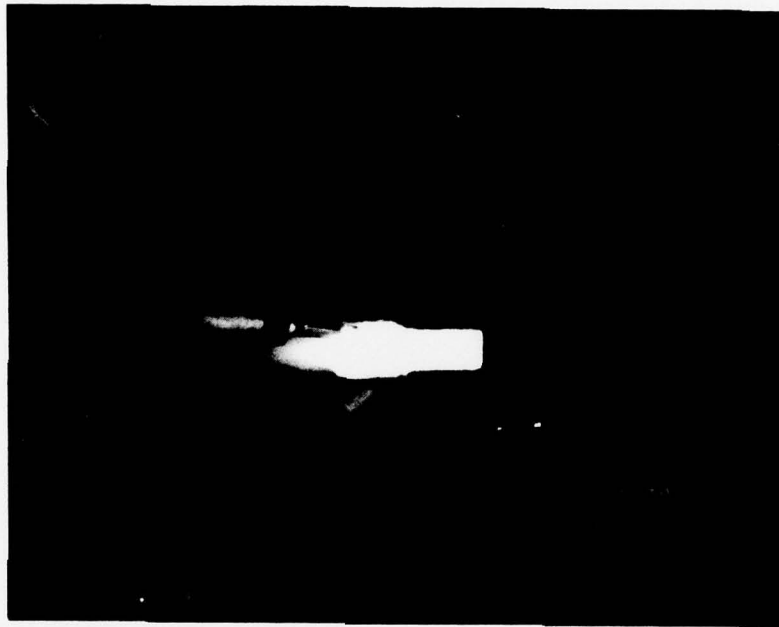


Figure 90: Hot Band Across the Surface of the
Test Segment on the Jet Exhaust Rig

Table 7

Sample	Composition	Lead Edge	Abradable Surface (Beyond Lead Edge)	Interfacial Bond Between Abradable and Support Layers	Interfacial Bond Between the Support Layer and the Shoe
1	Abradable - Material A-2 2400 psi (16.5 MPa) irregular shaped particles	Small amounts of erosion on lead edge where tem- perature reached > 1150°C	No apparent erosion Extent of oxidation undetermined	No apparent disbond	Disbond at lead edge due to poor initial braze bond. Braze AMS 4777 was used
	Support - Material A-1 5000 psi (34.5 MPa) irregular shaped particles				
2	Abradable - Material A-2 2100 psi (14.5 MPa)	Same as #1	Same as #1	Same as #1	Direct sinter of material to support structure resulting in no disbond in this area
	Support - Material B-2 7500 psi (51.7 MPa) spherical shaped particles				
3	Abradable - Material A-2 2100 psi (14.5 MPa)	Heavy erosion at the lead edge due to the lack of strength in the support layer. Temperature reached >1150°C	Same as #1	Not Applicable	Same as #1
	Support - None				
4	Abradable - Material A-2 2100 psi (14.5 MPa)	Same as #1	Same as #1	Not Applicable	No disbond noted. AMS 4783 braze used
	Support - None				

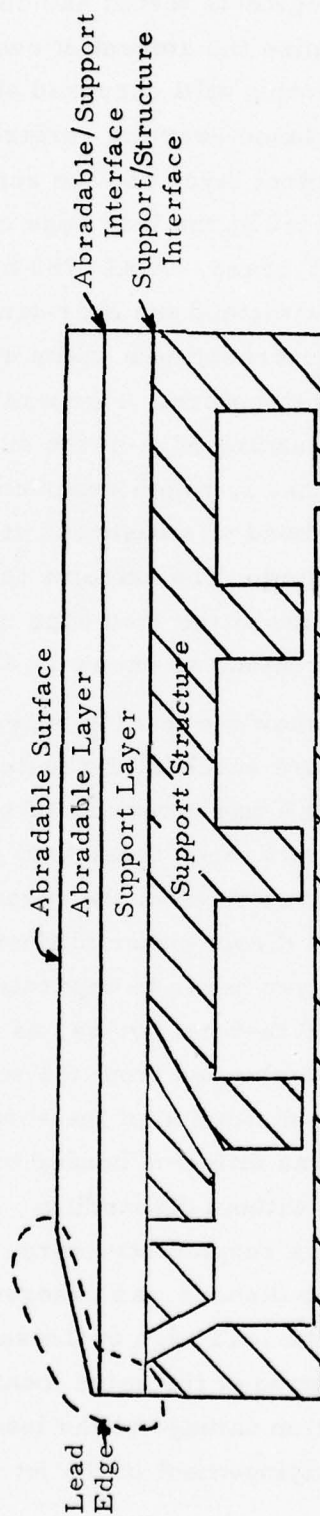


Figure 91: Location of Areas of Evaluation

Lead Edge - All of the segments tested had chamfered leading edges, as shown in Figure 91, to minimize the amount of overheating that occurs at this location. However, overheating still occurred at the leading edge because the jet stream did not glance over the surface but actually impinged on the area between the flow control layer and the support structure. The excessive temperature experienced at the lead edge caused failure of all interfaces bonded with AMS 4777 braze. AMS 4783 braze and all diffusion bonded interfaces were able to withstand the over-temperature condition without failure. The degree of overheating became exaggerated if disbonding occurred just above the support structure. Temperatures as high as 2280°F (1250°C) were developed at the leading edge of the surface. Figures 92 and 93 are photographs of test segment 3, which experienced these extreme temperatures. A noticeable disbond was observed at 60 cycles (Figures 94 and 95) and the test was terminated. The extreme temperature caused extensive oxidation to the particles at the lead edge of the surface (Figure 96), resulting in heavy amounts of erosion, as shown in Figures 97 and 98.

Figures 99 through 103 show the leading edges of the three structures (segments 1, 2, and 4) which were successfully tested for 100 thermal cycles of the jet exhaust rig. (Segment 4 was a remake of segment 3 with the exception of the braze which was changed from AMS 4777 to AMS 4783). No disbonds were observed in the area between the abradable and the flow control layers which were bonded by the direct sinter (diffusion) technique. However, in segment 1 the flow control layer began to separate from the support structure after approximately 70 thermal cycles, as shown in Figure 104. Although the flow control layer disbonded from the support structure, it had enough strength to minimize the distortion of the abradable layer. Segment 2 (shown in Figure 105) which was diffusion bonded to the support withstood the over-temperature condition without disbonding. In Segment 4 the abradable layer was attached directly to the support structure, as shown in Figure 106. AMS 4783 braze was used and no disbond was observed. Figure 107 shows the oxidation of the particle at the lead edge of the surface of segment 4 and is typical of the amount of oxidation at the same location for segments 1 and 2. Figure 108 shows the oxidation damage at the lead edge of the flow control layer of segment 2 due to the impingement of the jet stream at that point.

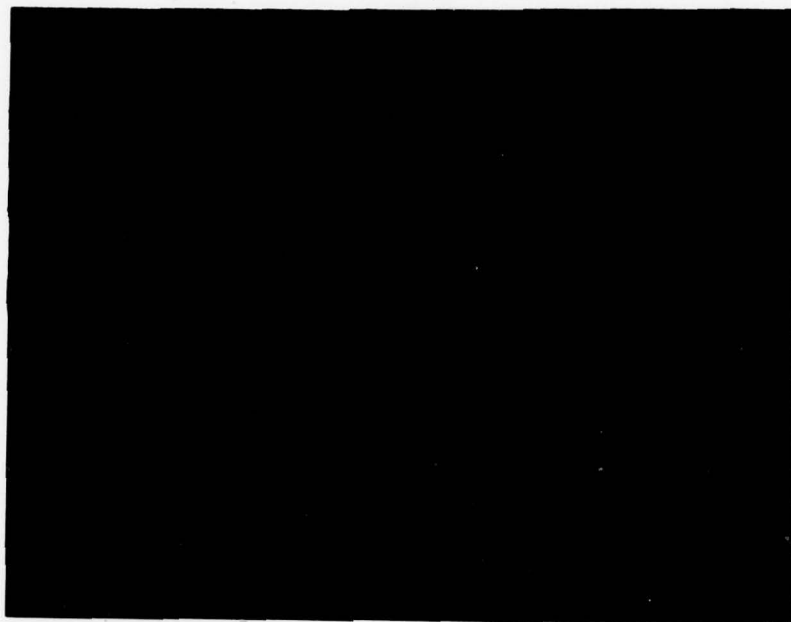


Figure 92: Test Segment 3 Prior to Testing 2X

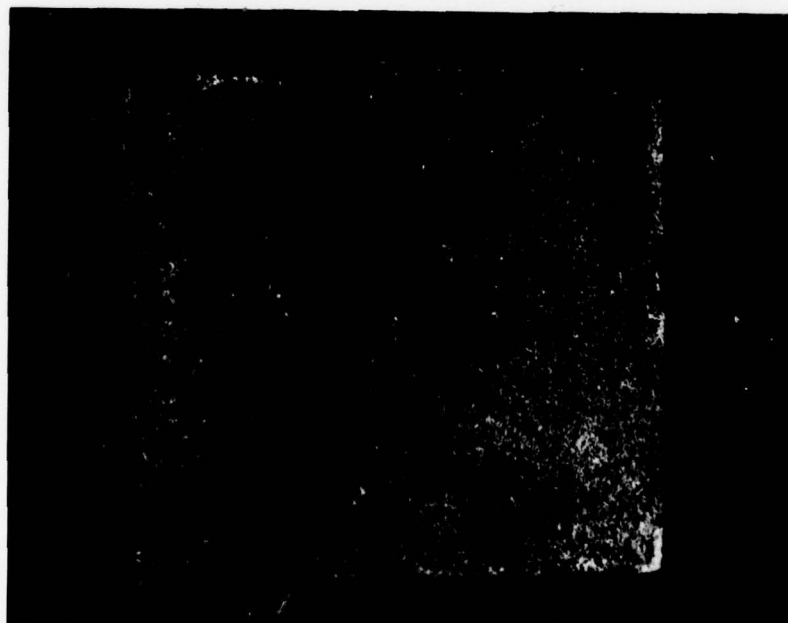


Figure 93: Test Segment 3 After 60 Thermal Cycles 2X

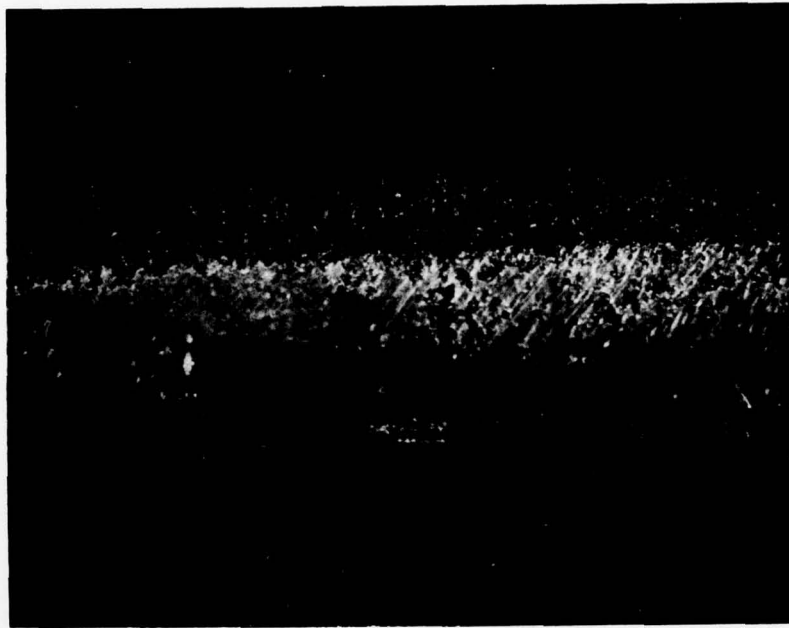


Figure 94: Lead Edge of Test Segment 3 Prior to Testing 4X



Figure 95: Lead Edge of Test Segment 3 After 60 Thermal Cycles 4X

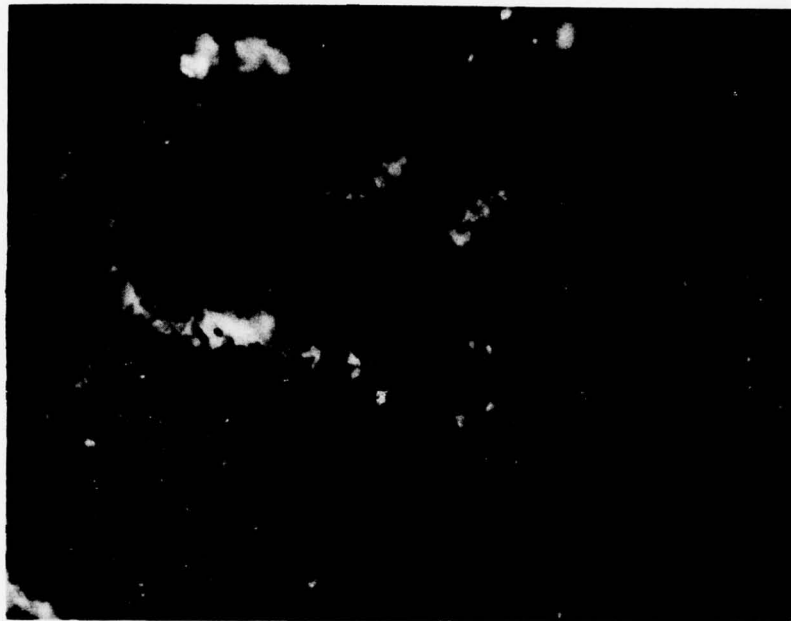


Figure 96: Oxidation of Particles at the Lead Edge of Segment 3
500X



Figure 97: Lead Surface of Segment 3 Prior to Testing 4X



Figure 98: Lead Surface of Segment 3 After 60 Thermal Cycles 4X

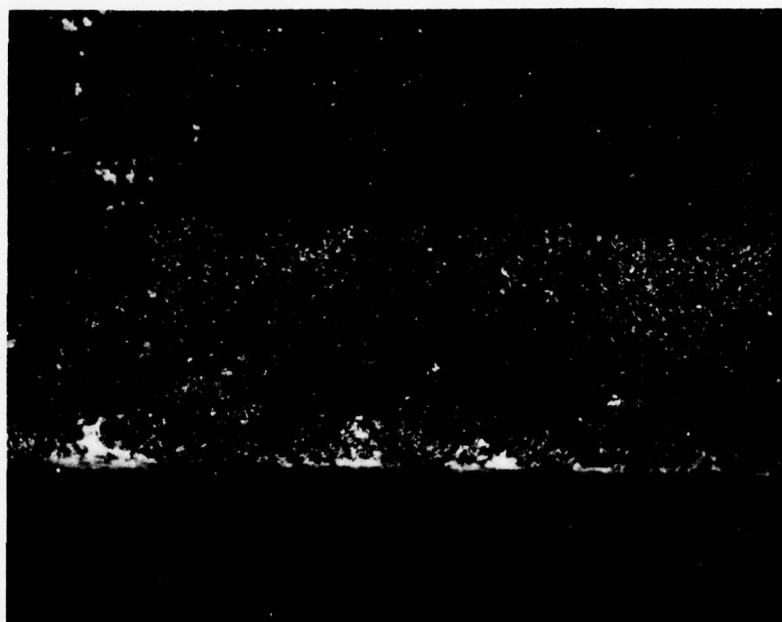


Figure 99: Lead Surface of Segment 1 After 100 Thermal Cycles 4X

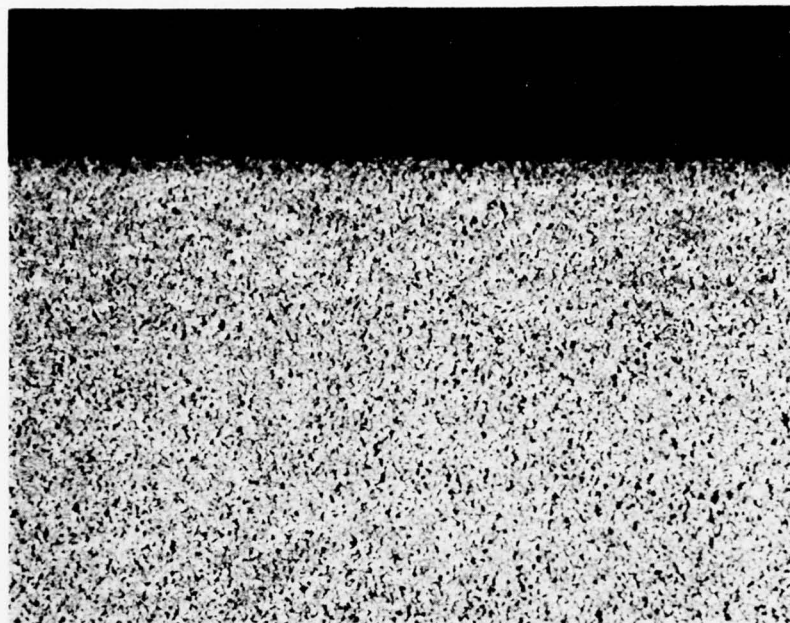


Figure 100: Lead Surface of Segment 2 Prior to Testing 4X

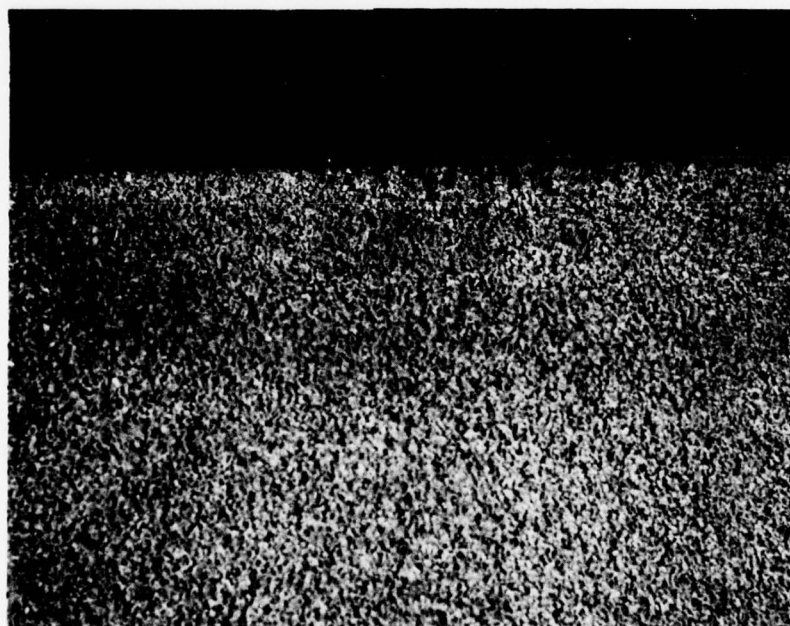


Figure 101: Lead Surface of Segment 2 After 100 Thermal Cycles 4X

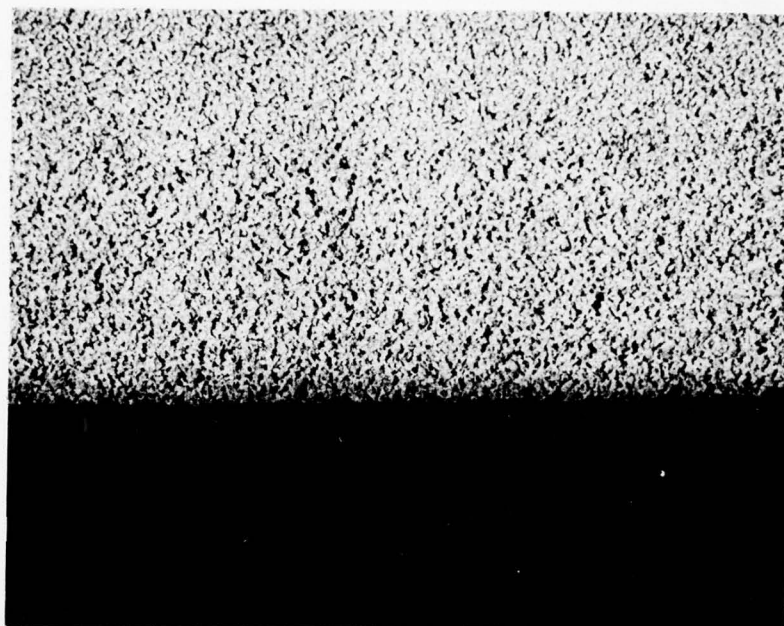


Figure 102: Lead Surface of Segment 4 Prior to Testing 4X



Figure 103: Lead Surface of Segment 4 After 100 Thermal Cycles 4X

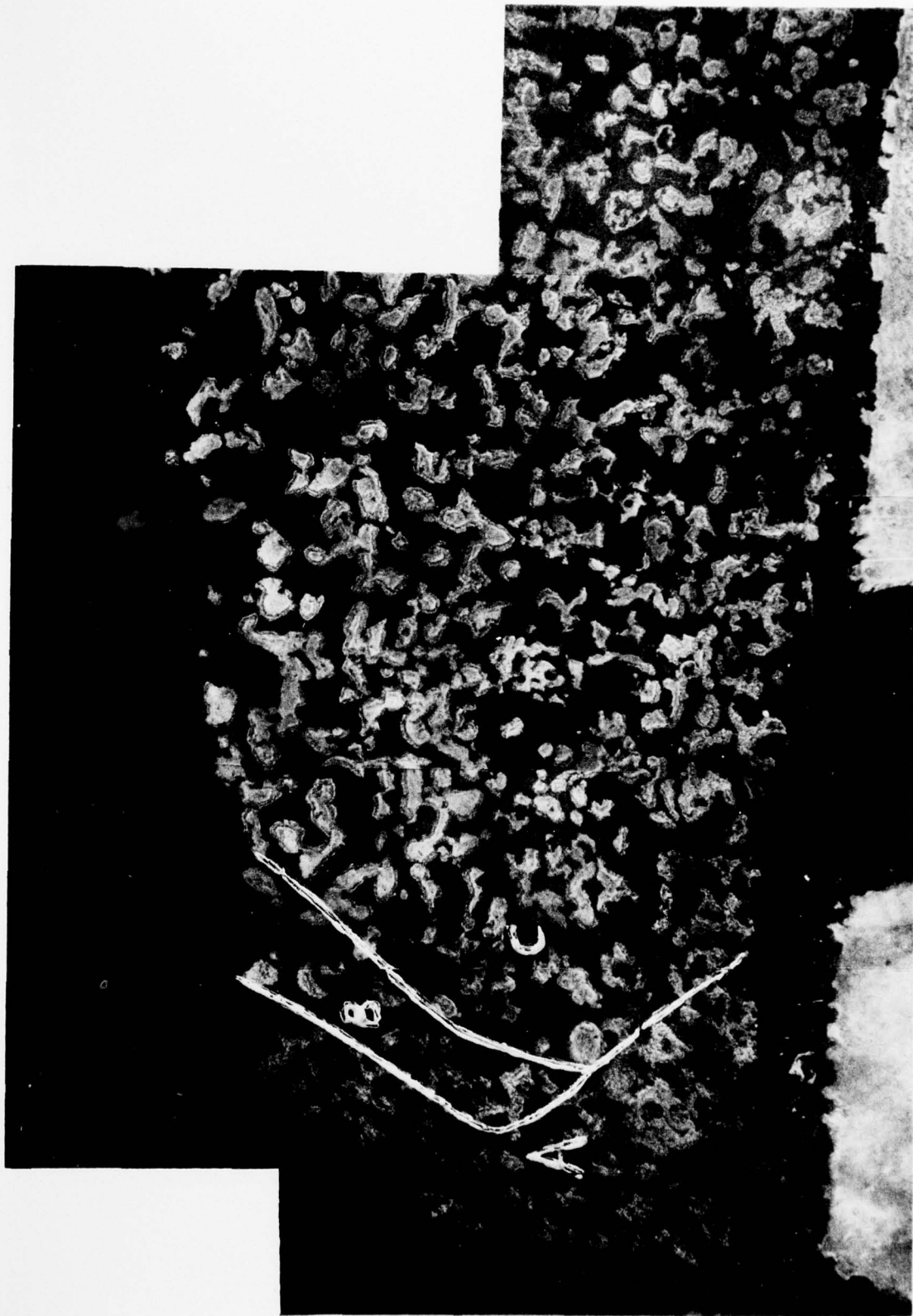


Figure 104: Micrograph of the Lead Edge of Segment I 50X

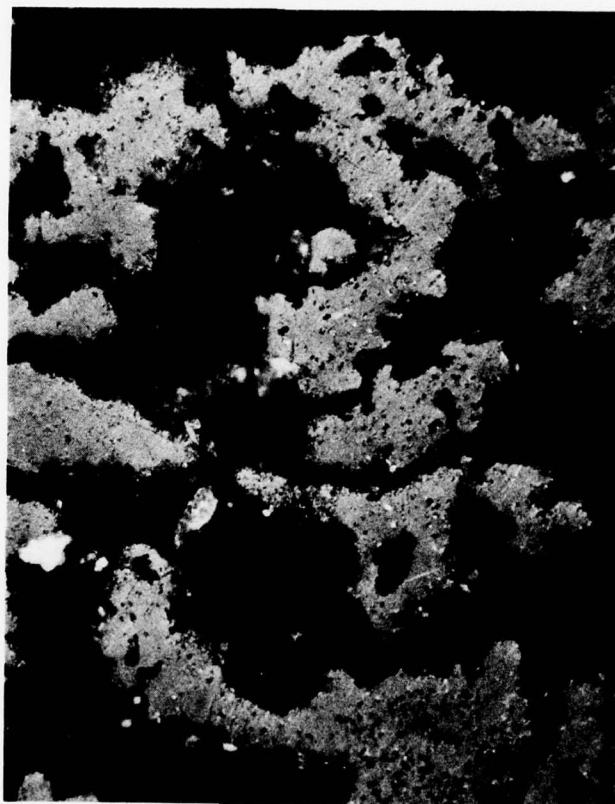


Figure 105: Micrograph of the Lead Edge of Segment 2 50X



Figure 106: Micrograph of the Lead Edge of Segment 4 50X

Surface



Lead Edge

Figure 107: Particles at Lead Edge of Segment 4 200X



Figure 108: Particles at the Lead Edge of the Flow
Control Layer of Segment 2 200X

The lead edge of the three different segments which completed 100 thermal cycles are shown in Figures 104, 105, and 106. Each figure is divided into zones. Zone "A" particles have extensive external oxidation with some internal oxidation. Zone "B" is a bordering layer; although there was no internal oxidation of the particles, the amount of the protective phase was decreasing. Zone "C" particles have no internal oxidation, and the protective phases are in quantities similar to those at the beginning of testing. As Figures 95 and 96 show, the more severe oxidation areas and the erosion areas were areas that were directly exposed to the jet stream impingement.

Areas as far back as the first cooling chamber show more oxidation than was expected at the support structure/flow control layer interface. This increase was attributed to heat which was conducted through the support structure and then transferred to the particles. Figures 121 and 124 show cracks in the Inconel 600 support structure and indicate the harshness of the test conditions.

Abradable Surface - The abradable surfaces are shown in Figures 109 through 113. Although the temperature at 1/4 in (6.35 mm) from the lead edge was 1900°F (1040°C), the extent of the structure's severe oxidation was limited to less than a full particle in depth, as shown in Figure 114. The protective rimming phase was still present in quantities similar to those initially present. Also, no discernible erosion occurred, indicating that the material demonstrates good erosion and oxidation resistance properties when tested at or below a maximum continuous operating temperature of 1900°F (1040°C).

Interfacial Bonds Between the Abradable and the Flow Control Layers -

There was no sign of separation between the abradable layer and the flow control layer. The bonds between the layers in segments 1 and 2 were formed by direct sintering. (This is not applicable to segments 3 and 4 which were formed as single layers.) Because no braze was used between the layers (such as occurred in the initial contract), there was no accompanying particle growth or reduction in pore size which would reduce air flow through the sample.

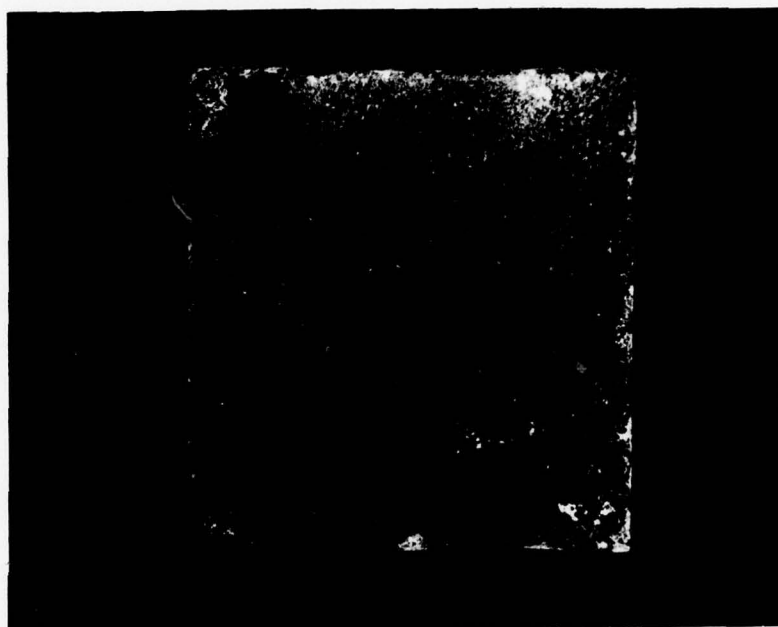


Figure 109: Surface of Segment 1 After 100 Thermal Cycles 2X

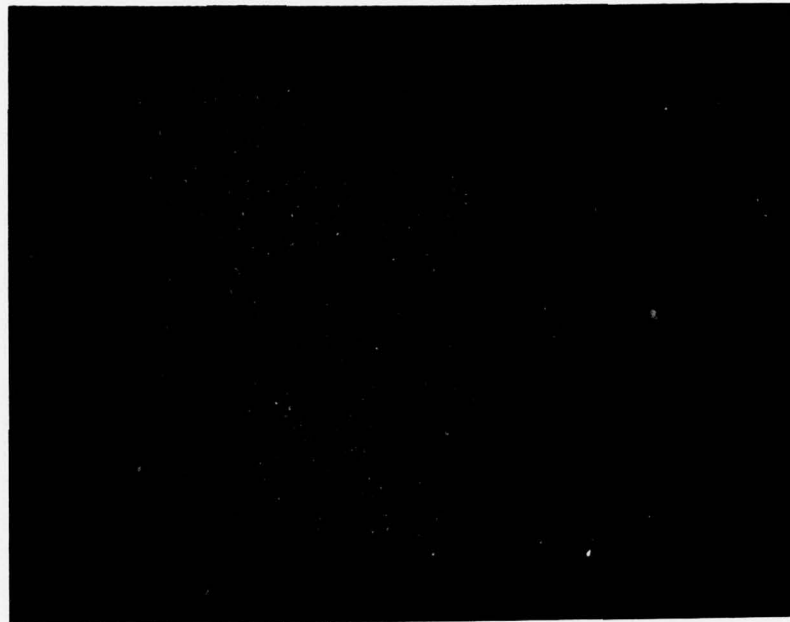


Figure 110: Surface of Segment 2 Prior to Testing 2X



Figure 111: Surface of Segment 2 After 100 Thermal Cycles 2X

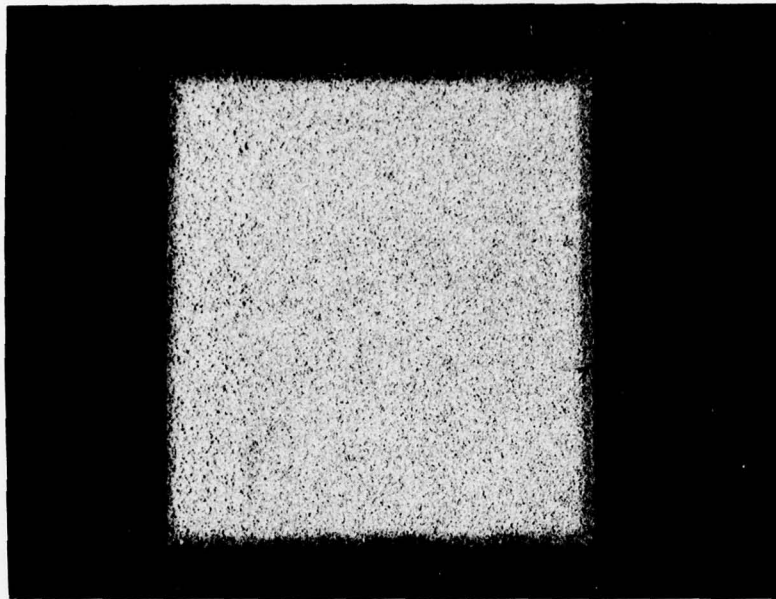


Figure 112: Surface of Segment 4 Prior to Testing 2X

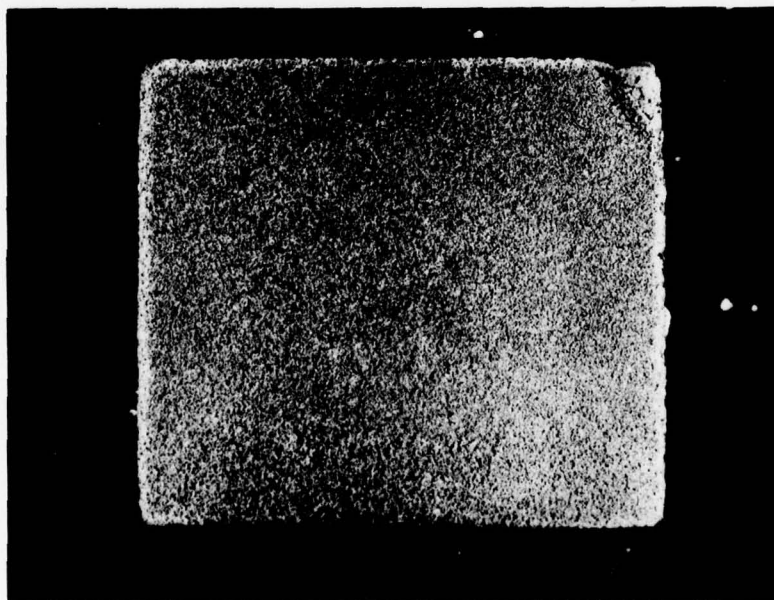


Figure 113: Surface of Segment 4 After 100 Thermal Cycles 2X



Figure 114: Particles at the Surface of Segment 4
1/4 in (6.3 mm) from the Lead Edge 200X

Figure 115 shows the interface near the lead edge where the oxidation was heavy. Since this area was subjected to excessive temperature some deterioration of the particle-to-particle bonds occurred. The deterioration was no worse than at other areas subjected to the extreme temperature. Figure 116 shows the interfacial bond area where the temperature was maintained below 1900°F (1040°C). Most of the material was nearly unchanged from the initial condition.

Interfacial Bonds Between the Flow Control Layer and the Support Structure - This area presented the most difficulty in testing. Sample 1 was attached to the support structure by AMS 4777 braze. This element began to lift off the support structure at the lead edge (the hottest location) after approximately 70 thermal cycles (Figure 117). The cross-section showed that extensive amounts of braze had wicked up into the structure (Figures 118 and 119), causing a reduction in the number and size of contacts between NiCrAl and the support structure. It also resulted in densification of the area directly above the support structure. Like brazing, direct sintering requires that maximum particle contact be made between the flow control layer and the support structure. This is difficult to accomplish in either attachment method.

Brazing of sample 2, which has a finer pore size, to the support structure was not considered, since wicking of the braze would have significantly restricted the cooling air path. Instead, the NiCrAl material was direct sintered (Figures 102 and 103).

Sample 3 (Figures 120, 121, and 122) was attached to the support structure with AMS 4777 braze. After 60 cycles, the lead edge lifted and serious erosion resulted in the unsupported areas. Cross-sections of this sample also revealed braze wicking. In addition to the wicking problem, the braze did not have acceptable oxidation resistances when it was exposed to a temperature as high as 2192°F (1200°C) continuously. Another braze was required. The replacement braze was AMS 4783. The amount of wicking was more easily controlled by using this composition. Sample 4 (the same as sample 3, with the exception of the braze composition, shown in Figures 123 and 124), when attached with AMS 4783 braze, survived 100 cycles without separation at the interface. The cross-section (Figure 125) revealed numerous particles bonded to the support structure.

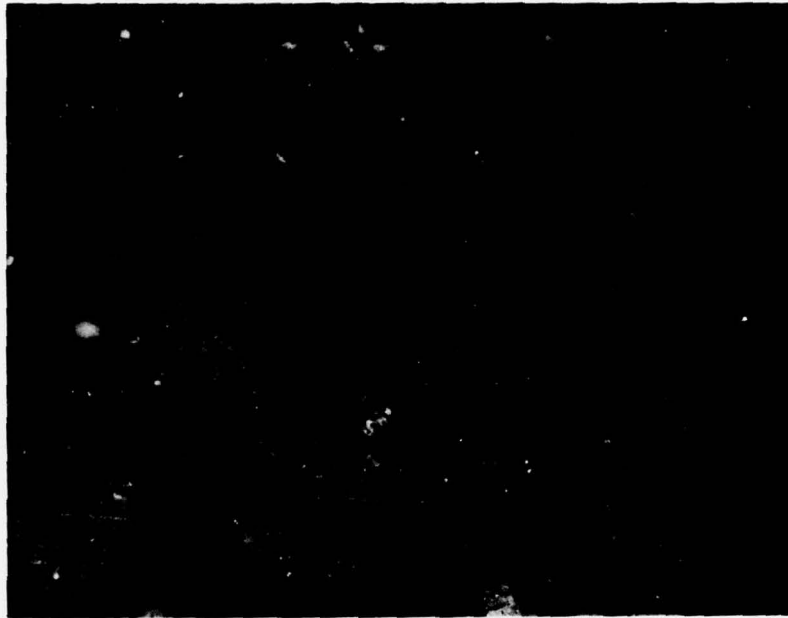


Figure 115: Interface Between the Abradable Layer and the
Flow Control Layer Near the Lead Edge 200X



Figure 116: Interface Between the Abradable Layer
and the Flow Control Layer Halfway
Between the Leading and Trailing Edges 200X



Figure 117: Lead Edge of Segment 1 After 100 Thermal Cycles 4X

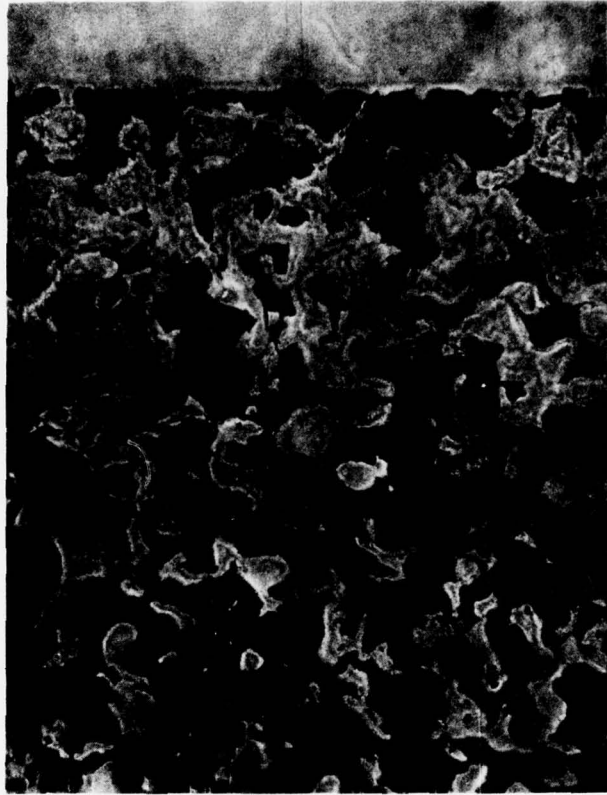


Figure 118: Microstructure of Segment 1 Showing
the Braze Wicking 50X

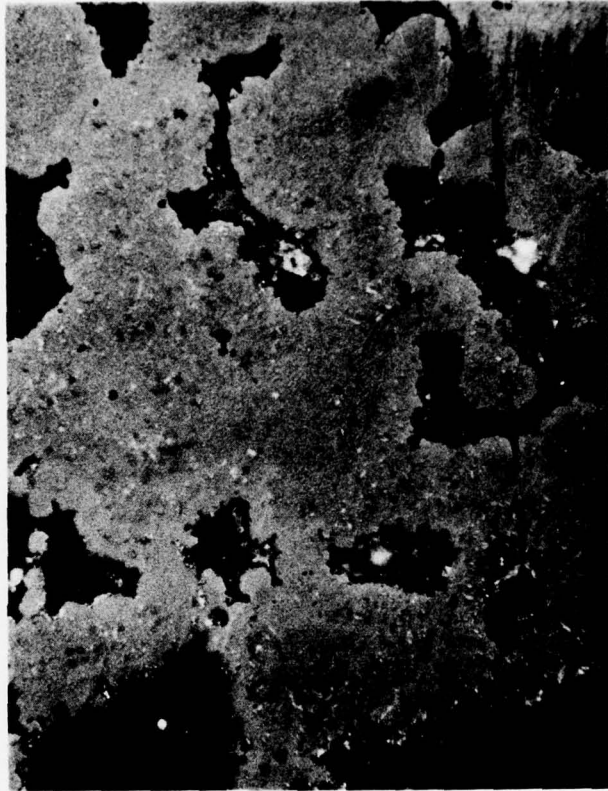


Figure 119: Microstructure Showing the Structure Densification
of Segment 1 Due to Braze Wicking 200X

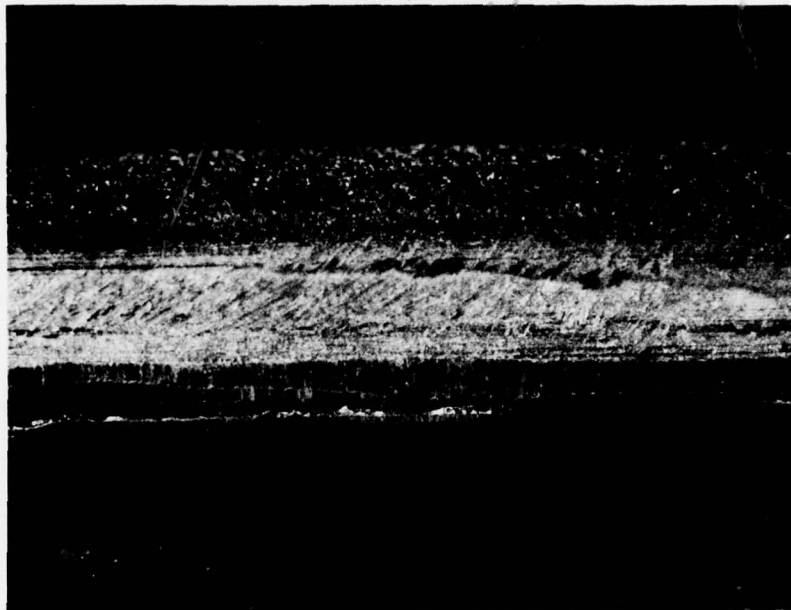


Figure 120: Lead Edge of Segment 2 Prior to Testing 4X

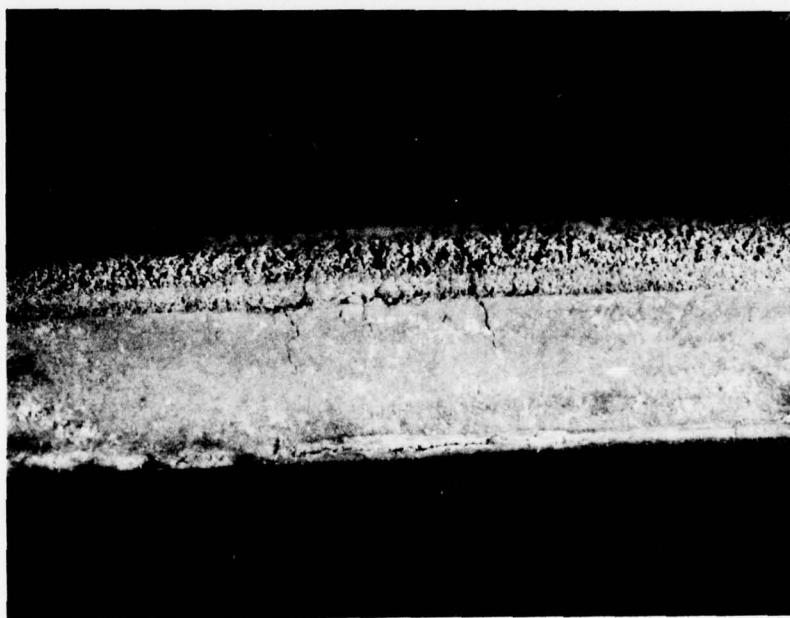


Figure 121: Lead Edge of Segment 2 After 100 Thermal Cycles 4X

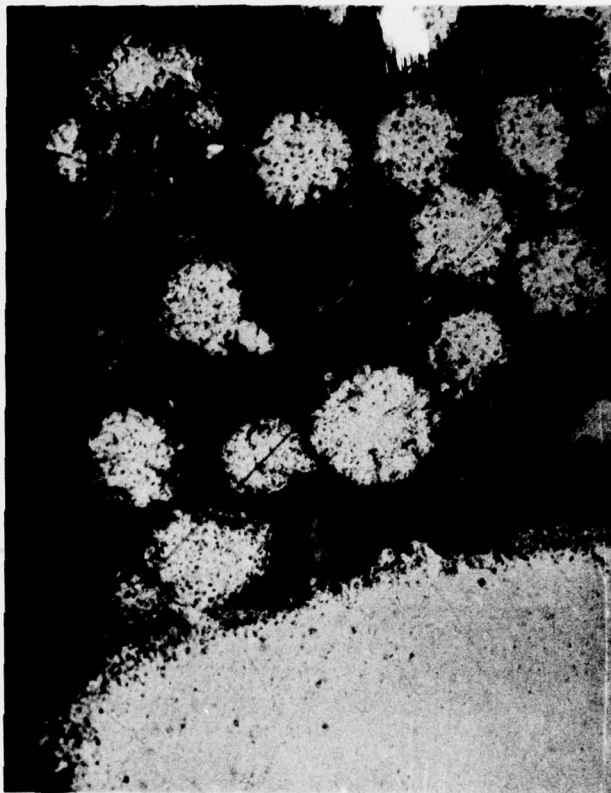


Figure 122: Microstructure of Lead Edge of Segment 2
After 100 Thermal Cycles 200X

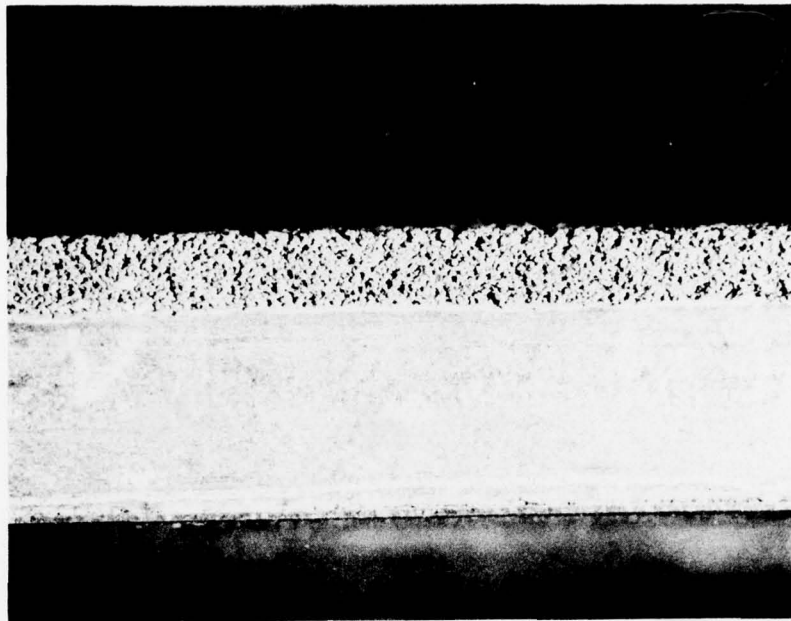


Figure 123: Lead Edge of Segment 4 Prior to Testing 4X



Figure 124: Lead Edge of Segment 4 After 100 Thermal Cycles 4X



Figure 125: Microstructure of Segment 4 After
100 Thermal Cycles 200X

The AMS 4783 braze was used for attachment to the support structure during the remainder of the testing.

General - The data taken and general observations indicated that there was no advantage to using stronger layers or layers having finer pore structures when they were properly attached to the optimized support structure. The large pore size abrasable structure reduced the possibility of pore size reduction and pore blockage due to oxidation that would result in restriction of air flow through the material. For these reasons, a single layer of Material A-2 is recommended to serve as both the abrasable layer and the flow control layer.

A cooling air flow of 25 SCFH (11.8 l/min) at 1200°F (649°C) and 30 psi (207 KPa) was needed to provide the necessary surface cooling per segment.

3. Variable Flow Test

Purpose - The purpose of this test was to determine what effect an increased or decreased flow of cooling air would have on the surface temperature. The optimized flow rate established in the "Thermal Cycle/Hot Gas Erosion Testing for Structure Optimization" section was used as a baseline.

Procedure - This test was run on the jet exhaust rig. The same conditions and test parameters which were used in the "Thermal Cycle/Hot Gas Erosion Testing for Structure Optimization" section were used to establish the baseline. The cooling gas flows were then increased and decreased by approximately 50%.

The test sample was the optimum structure determined in the "Thermal Cycle/Hot Gas Erosion Testing for Structure Optimization" section. This sample was a 0.120 in (0.30 cm) thick abradable layer of Material A-2, selected from the "Thermal Cycle/Hot Gas Erosion Testing for Structure Optimization" section, and the support structure designed in the "Plenum Design" section (approximately 0.250 in (0.64 cm) thick). This test was required by the contract; however, the test was also repeated on the remaining two structures tested in the "Thermal Cycle/Hot Gas Erosion Testing for Structure Optimization" section to obtain more complete data.

Temperature variations were plotted as a function of position on the sample's surface. These positions were limited to points within the confines of the hot band which existed on the sample surface from the leading edge to the trailing edge.

Discussion and Results - Figures 126, 127, and 128 show the cooling curves generated in this task. The shape of the curve may be, in part, due to the surface configuration of the segment and, in part, due to the cooling air flow. A narrow, cool zone resulted where the abradable surface meets the chamfered surface (Figure 129), even when no cooling air was applied. As the cooling flow increased, the width of the band increased. This variation affected the temperature taken at position B (Figure 130); however, since this effect was not apparent when testing was limited to low flow rates, no attempt was made to take temperatures at a different location.

The figures show that the cooling experienced with the flow rate established in the "Thermal Cycle/Hot Gas Erosion Testing for Structure Optimization" section is close to optimum and that the temperature variations due to changes in flow are distinct.

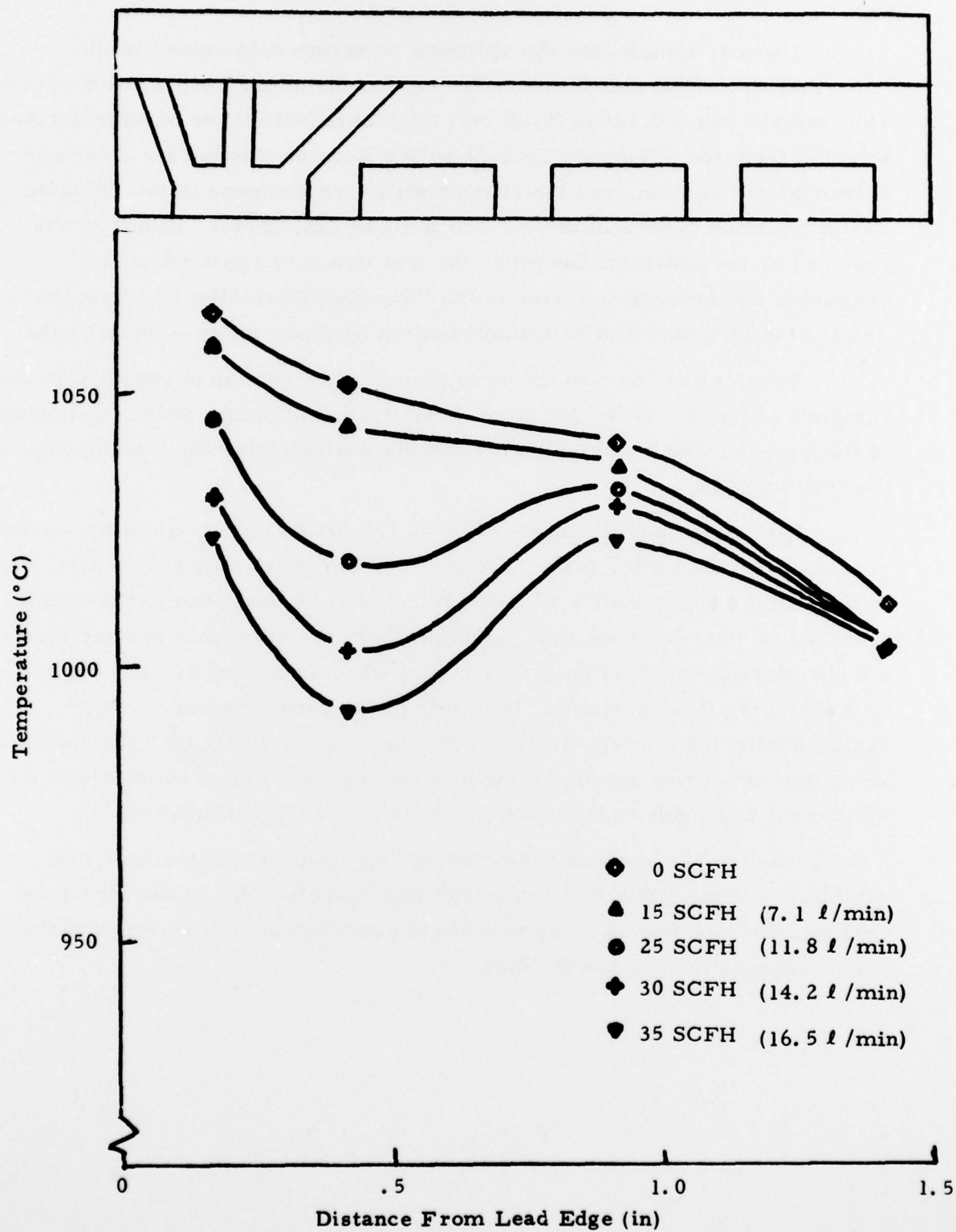


Figure 126: Surface Temperature of Segment 1 as a Function of Position for Different Flow Rates of 1200°F (649°C) Cooling Air

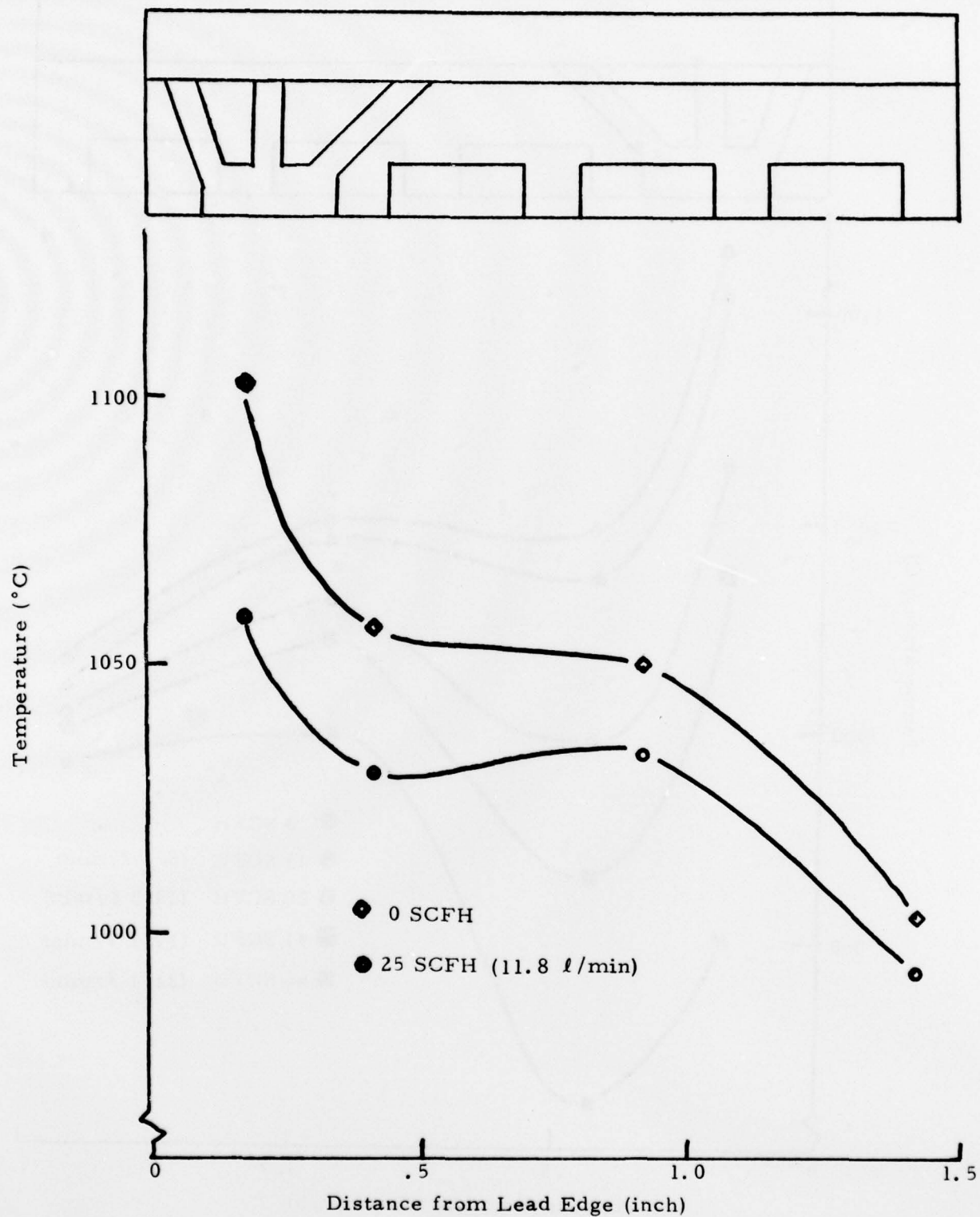


Figure 127: Surface Temperature of Segment 2 as a Function of Position for Different Flow Rates of 1200°F (649°C) Cooling Air

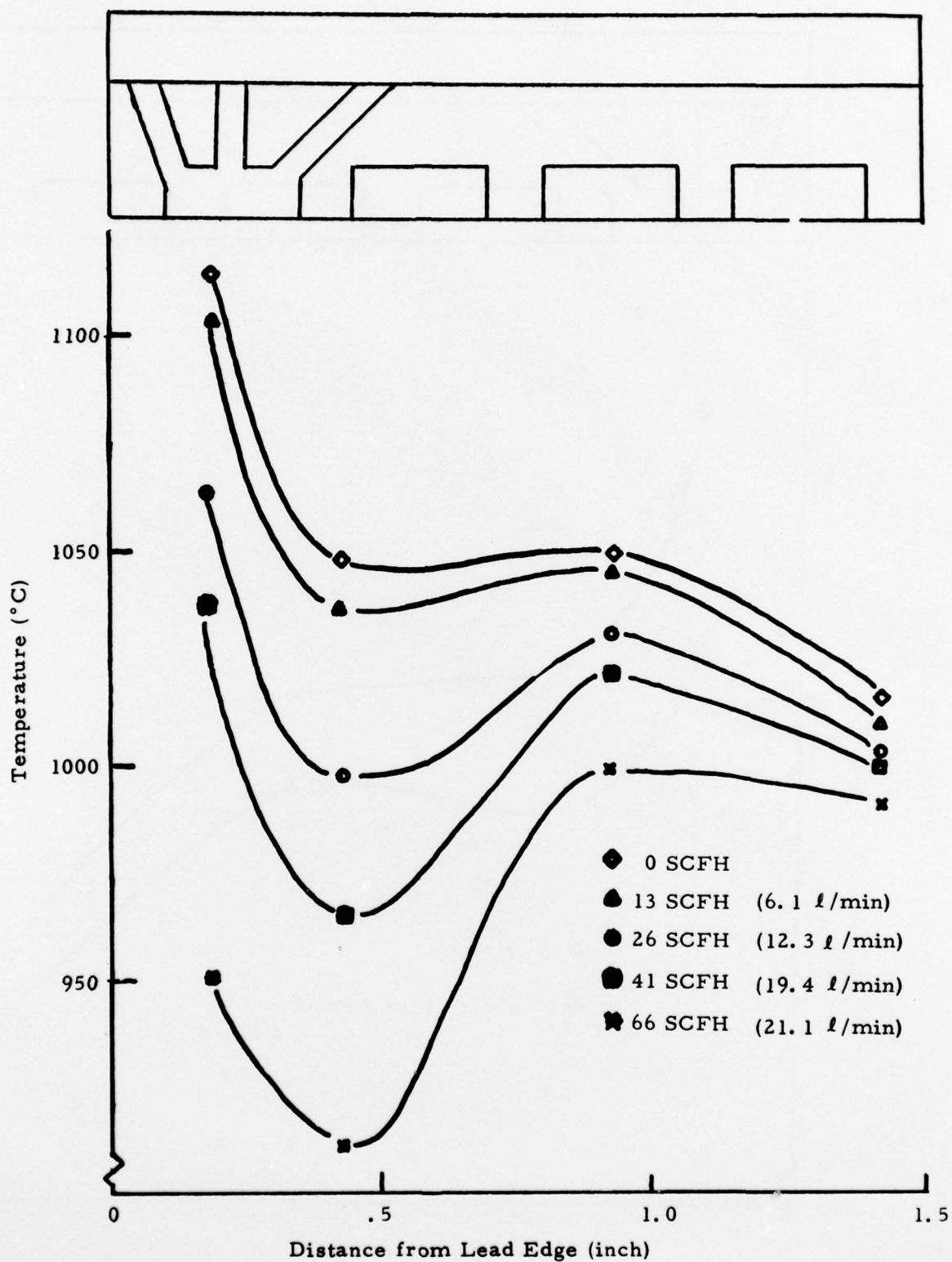


Figure 128: Surface Temperature of Setment 4 as a Function of Position for Different Flow Rates of 1200°F (649°C) Cooling Air

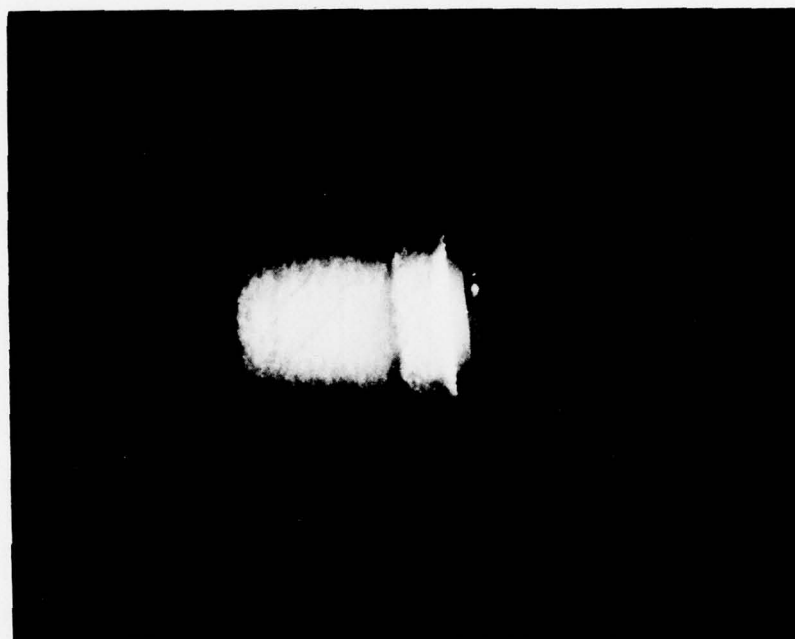


Figure 129: Test Segment on Jet Exhaust Rig Showing the Cool Area Behind the Chamfered Surface

A, B, C, and D - Temperature Positions

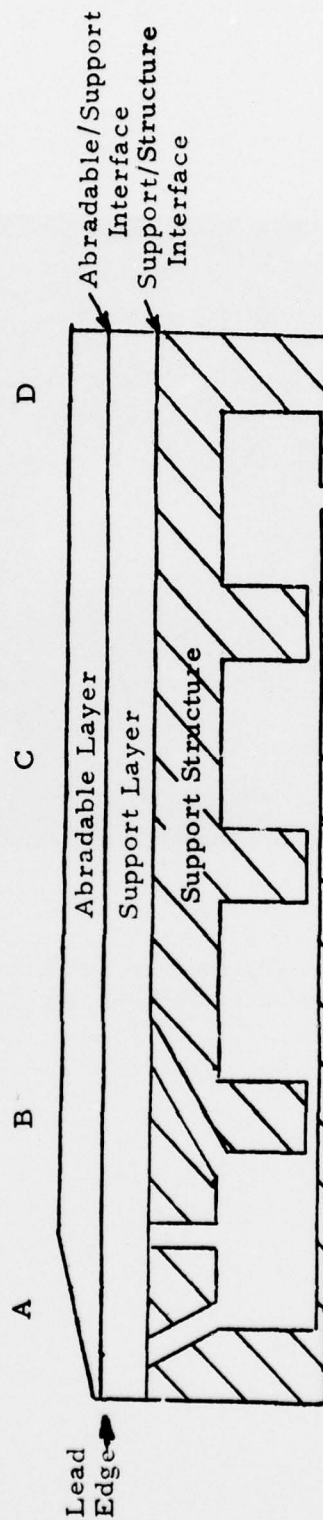


Figure 130: Location of Surface Temperatures Taken on Segment Subjected to Testing on the Jet Exhaust Rig

4. Temperature Profile

Purpose - The original purpose of this task was to determine the temperature gradient which existed through the optimum shroud design when subjected to simulated engine temperature. At the request of Captain Vonada, this purpose was expanded to include determination of the temperature profile which resulted when a barrier was positioned at the lead edge (which shielded the shroud segment from direct gas stream impingement).

Procedure - The determination of the temperature gradient through the optimized test shroud was carried out on the jet exhaust rig. The test was run in two parts. The first part was carried out by using the same test parameters as those used in the "Thermal Cycle/Hot Gas Erosion Testing for Structure Optimization" section. The second part called for a physical barrier to be placed in front of the leading edge of the sample and nearly flush with the abradable surface. The purpose of the barrier was to simulate more closely the conditions which existed in an actual engine where, for aerodynamic reasons, a segment should not jut into the combustion gas stream.

For both tests, the surface temperatures were measured by optical and radiation pyrometers. Chromel-alumel thermocouples were used for determination of the interfacial temperatures.

Since the optimized porous metal structure was a single homogeneous layer with no interfacial areas, the thermocouples were positioned halfway through the structure rather than at a distinct interface between the abradable and flow control layer. This arrangement is shown in Figure 131.

Discussion and Results - The first test part, which was run exactly the same as the "Thermal Cycle/Hot Gas Erosion Testing for Structure Optimization" section, gave the temperature gradient shown in Figure 132.

The addition of the barrier to the lead edge required some changes in the testing parameters from those used in the previous section of this report. With the barrier in place, as shown in Figure 131, the jet stream did not adequately heat the segment. As a result, the orientation of the segment with respect to the gas stream was increased from a 30° to a 45° angle. Also, with the barrier in place, since the chamfer at the leading edge of the abradable segment was not required, it was eliminated from the sample design. All other test parameters remained the same.

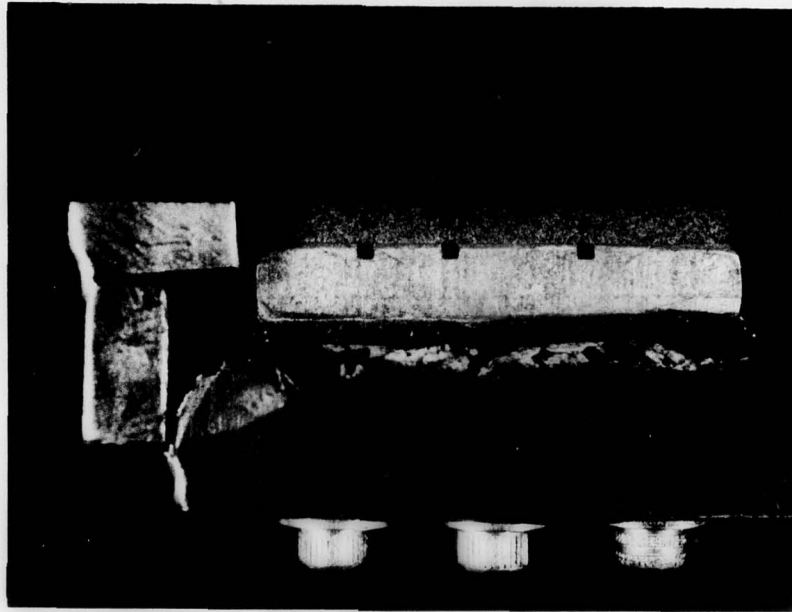


Figure 131: Thermocouple Location for Temperature
Profile Measurement 2X

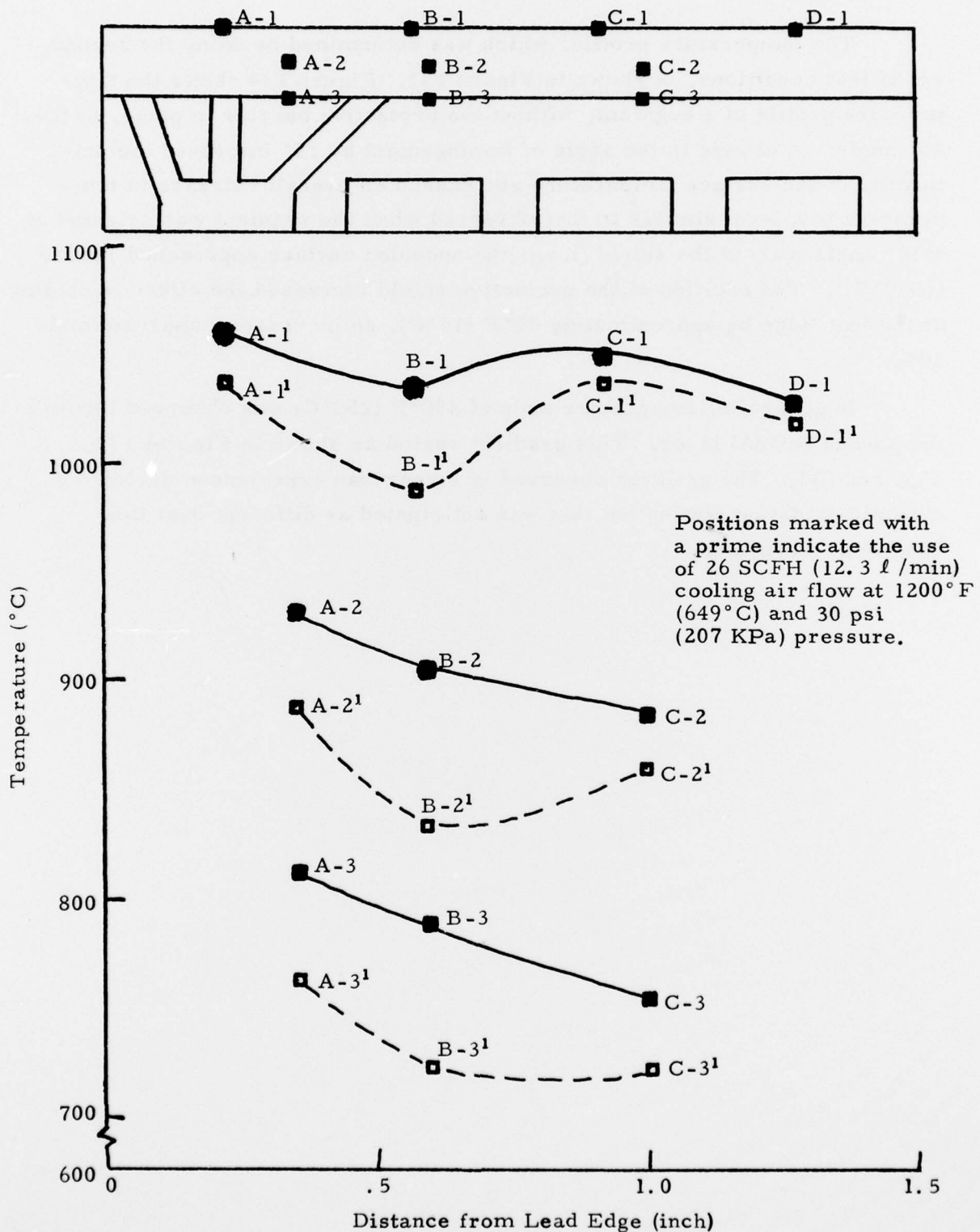


Figure 132: Temperature Profile of Test Structure Oriented 30° with Respect to the Jet Stream and No Protective Barrier at the Lead Edge

The temperature profile, which was determined by using the second set of test conditions, is shown in Figure 133. Figure 134 shows the temperature profile of a segment, without the protective barrier in place, at the 45° angle. A change in the angle of impingement by 15° improved the uniformity of the surface temperature and caused an overall increase in temperature to a level similar to that observed when the segment was oriented at a 30° angle without the shield (i. e. , the uncooled surface approached 1960°F (1070°C)). The addition of the protective shield increased the effective cooling at the lead edge by approximately 27°F (15°C), an increase of approximately 30%.

In general a temperature drop of 450°F (250°C) was observed through the porous NiCrAl layer. This gradient varied as shown in Figures 132, 133, and 134. The gradient observed is larger than experienced during the dynamic oxidation testing but this was anticipated as different heat flow conditions were used.

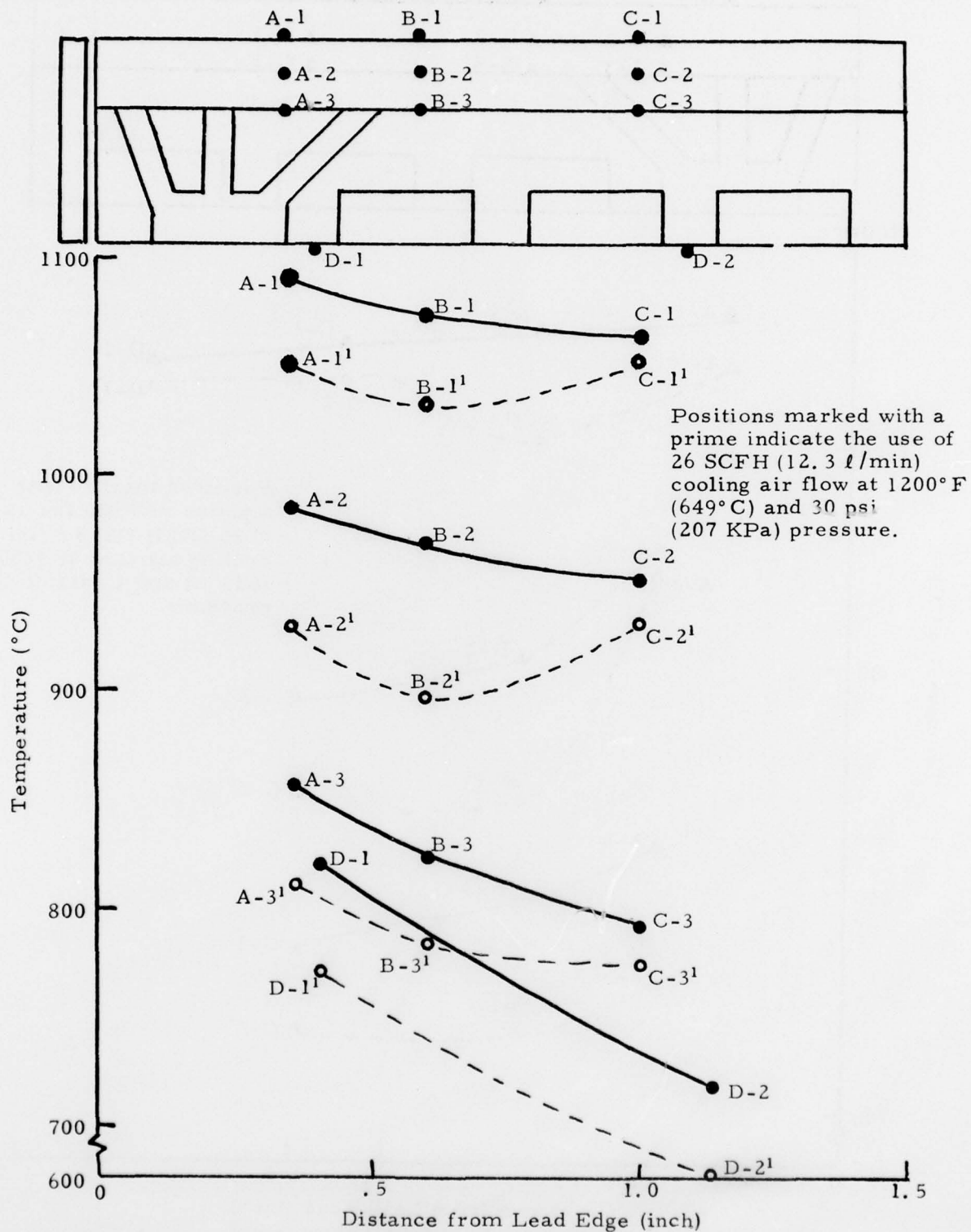


Figure 133: Temperature Profile of Test Structure Oriented 45° with Respect to the Jet Stream and with a Protected Lead Edge

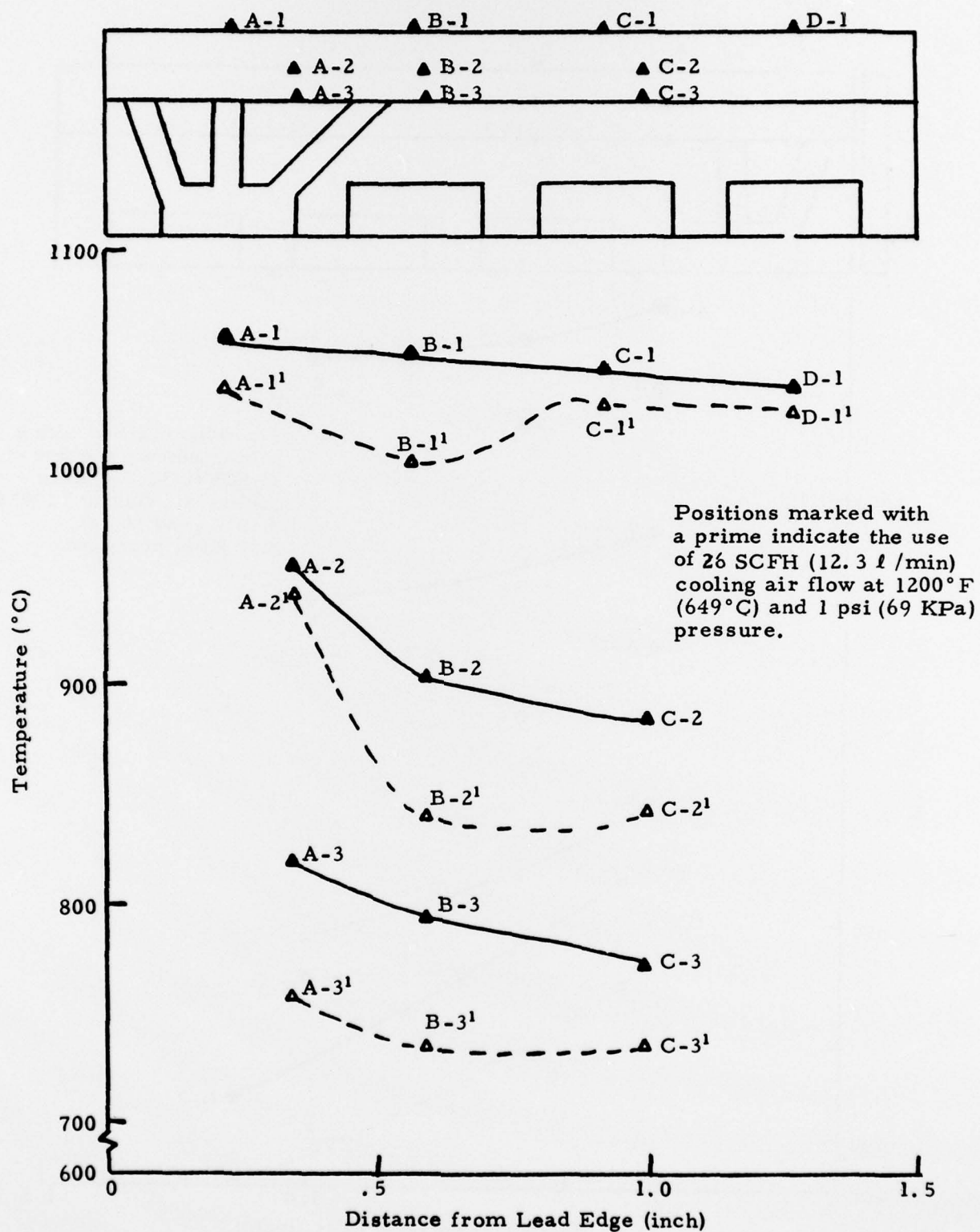


Figure 134: Temperature Profile of Test Structure Oriented 45° with Respect to the Jet Stream and No Protective Barrier at the Lead Edge

V. CONCLUSION

This program has shown that a transpiration-cooled abradable coated shroud can be produced that will withstand the severe environments anticipated in the high pressure turbine section of most jet engines. By designing the support structure properly, sufficient physical support can be given to the abradable portion of the shroud to permit use of a simple practical structure. Although simply designed this support structure can be constructed to provide transpiration cooling in critical regions and conductive cooling in less critical regions. This permits use of the cooling gas in the most efficient manner. The flow stability of the system is maximized by controlling the air flow at the support structure and using a porous abradable layer which has a very low pressure drop. By using these principles combined with a distended NiCrAl structure, designated in this report as Material A-2, a simple efficient, abradable, erosion resistant, coated shroud assembly has been developed for use at surface temperatures of 1900°F (1040°C).

1. Support Structure

The optimized support structure is shown in Figure 77. The cooling gas flow is controlled by the support through holes large enough to resist plugging. The largest unsupported span under the abradable is .0625 in (15.9 mm) eliminating the need of a strong support layer in the porous coating. The rear portion of the shroud is cooled by conductivity while the front portion is transpiration-cooled, providing for efficient use of the cooling gas.

2. Porous Metal Layer

The porous metal layer is a simple single layer of porous NiCrAl; it is a distended structure that enhances abrasability. The structure resists oxidation at 1900°F (1040°C) to the extent that only minor changes occur in its mechanical properties during long term testing. The oxidation that occurs only has minor effects on its flow properties and since it is a high flow structure and not the controlling member in the coated shroud, it has no significant effect on the flow through the shroud.

3. Porous Metal Layer - Support Structure

The abradable seal structure attached to the support structure by brazing was tested. AMS 4783 was the preferred braze for this application. A protective lip at the lead edge of the abradable was desirable to protect the braze and the porous metal. The abradable-support structure was tested by both gradient heating and thermal cycling. Segment 4 of the test series is the recommended system for further evaluation.

VI. RECOMMENDATIONS

This program has demonstrated on test rigs that an abradable seal-support system can be used in the high pressure turbine sections of jet engines. In this program actual engine hardware was not produced or tested. The test configuration was simple and should be easily adapted to permit evaluation on current engine hardware. Since rig testing does not directly duplicate engine conditions and optimized configuration can be readily adapted to engine hardware, it is suggested that the next phase of this effort be directed at testing in an actual engine rather than further additional rig testing.